

Oliver Zacharias

## **Gyrokinetic Simulations of Tearing Modes**

**IPP 12/13**  
**Juli,2015**

# Gyrokinetic simulations of tearing modes

Inauguraldissertation

zur  
Erlangung des akademischen Grades eines  
Doktors der Naturwissenschaften  
der  
Mathematisch-Naturwissenschaftlichen Fakultät  
der  
Ernst-Moritz-Arndt-Universität Greifswald

vorgelegt von: Oliver Zacharias  
geboren am 22. Januar 1982  
in Karl-Marx-Stadt

Greifswald, den 30. Mai 2015

Dekan: Prof. Dr. rer. nat. Klaus Fesser

1. Gutachter: Prof. Dr. Per Helander

2. Gutachter: Prof. Dr. Barrett N. Rogers

Tag der Promotion: 24. April 2015

# Abstract

The collisionless tearing mode is investigated by means of the  $\delta f$ -PIC code EUTERPE solving the gyrokinetic equation. In this thesis the first simulations of electromagnetic non-ideal MHD modes in a slab geometry with EUTERPE are presented.

Linear simulations are carried out in the cases of vanishing and finite temperature gradients. Both cases are benchmarked using a shooting method showing that EUTERPE simulates the linearly unstable tearing mode to a very high accuracy. In the case of finite diamagnetic effects and values of the linear stability parameter  $\Delta'$  of order unity analytic predictions of the linear dispersion relation are compared with simulation results. The comparison validates the analytic results in this parameter range.

Nonlinear single-mode simulations are performed in the small- to medium- $\Delta'$  range measuring the dependency of the saturated island half width on the equilibrium current width. The results are compared with an analytic prediction obtained with a kinetic electromagnetic model.

In this thesis the first simulation results in the regime of fast nonlinear reconnection (medium- to high- $\Delta'$  range) are presented using the standard gyrokinetic equation. In this regime a nonlinear critical threshold has been found dividing the saturated mode from the super-exponential phase for medium- $\Delta'$  values. This critical threshold has been proven to occur in two slab equilibria frequently used for reconnection scenarios. Either changing the width of the equilibrium current or the wave number of the most unstable mode makes the threshold apparent. Extensive parameter studies including the variation of the domain extensions as well as the equilibrium current width are dedicated to a comprehensive overview of the critical threshold in a wide range of parameters. Additionally, a second critical threshold for high- $\Delta'$  equilibria has been observed.

A detailed comparison between a compressible gyrofluid code and EUTERPE is carried out. The two models are compared with each other in the linear regime by measuring growth rates over wave numbers of the most unstable mode for two setups of parameters. Analytical scaling predictions of the dispersion relation relevant to the low- $\Delta'$  regime are discussed. Employing nonlinear simulations of both codes the saturated island half width and oscillation frequency of the magnetic islands are compared in the small- $\Delta'$  range. Both models agree very well in the limit of marginal instability and differ slightly with decreasing wave vector. Recently, the full polarisation response in the quasi-neutrality equation was implemented in EUTERPE using the Padé approximation of the full gyrokinetic polarisation term. Linear simulation results including finite ratios of ion to electron temperature are benchmarked with the dispersion relation obtained from a hybrid model. Finite

temperature effects influence the saturated island width slightly with increasing ion to electron temperature ratio which has been verified by both models.

# Contents

<b>List of Figures</b>	<b>vii</b>
<b>List of Tables</b>	<b>ix</b>
<b>Nomenclature</b>	<b>xi</b>
<b>1 Introduction</b>	<b>1</b>
1.1 Magnetic reconnection . . . . .	1
1.2 Preparation for reconnection: A hydrodynamic analogon . . . . .	5
1.3 Current research and motivation for this work . . . . .	8
1.4 Collisionless tearing mode instability . . . . .	10
1.4.1 The linear tearing mode . . . . .	10
1.4.2 Overview of analytical dispersion relations . . . . .	15
1.4.3 The nonlinear tearing mode . . . . .	17
<b>2 Gyrokinetics</b>	<b>19</b>
2.1 Gyrokinetic description . . . . .	19
2.2 Electromagnetic gyrokinetic equations in a slab . . . . .	22
<b>3 The PIC method</b>	<b>25</b>
3.1 Implementation of the PIC method . . . . .	25
3.1.1 Discretisation of the distribution function . . . . .	25
3.1.2 Discretisation of the field equations . . . . .	27
3.1.3 Requirements in electromagnetic simulations . . . . .	27
3.2 Diagnostic tools . . . . .	28
<b>4 Electromagnetic simulations in a slab</b>	<b>31</b>
4.1 Normalisation procedures . . . . .	31
4.2 MHD slab equilibria for reconnection simulations . . . . .	31
4.3 Implementation of the slab geometry . . . . .	34
4.4 Linear benchmark in slab geometry . . . . .	36
<b>5 Linear simulations of the tearing mode</b>	<b>39</b>
5.1 Linear dispersion relation . . . . .	39
5.2 Benchmark of the tearing mode without gradients . . . . .	43
5.3 Benchmark of the tearing mode with gradients . . . . .	48
5.4 Critical behaviour caused by diamagnetic effects . . . . .	50
<b>6 Nonlinear simulations of tearing modes</b>	<b>55</b>

6.1	Simulations of nonlinear saturated reconnection . . . . .	56
6.2	Simulations of nonlinear super-exponential reconnection . . . . .	60
6.2.1	Phenomenology and first numerical simulations . . . . .	61
6.2.2	The transition between both nonlinear phases . . . . .	65
6.2.3	Extended parameter studies . . . . .	69
<b>7</b>	<b>Comparison of a compressible gyrofluid and gyrokinetic model</b>	<b>73</b>
7.1	Introduction . . . . .	73
7.1.1	The compressible gyrofluid model . . . . .	73
7.1.2	Equilibrium configuration and numerical setup . . . . .	75
7.2	Linear comparison of the models . . . . .	76
7.2.1	Eigenvalue equations . . . . .	76
7.2.2	Linear benchmark with eigenvalue approach . . . . .	77
7.2.3	Model comparison in the drift kinetic limit . . . . .	79
7.2.4	Influence of gyro-effects . . . . .	80
7.3	Comparison of the nonlinear models . . . . .	81
7.3.1	Drift kinetic limit . . . . .	82
7.3.2	Finite ion temperature effects . . . . .	85
<b>8</b>	<b>Conclusions and outlook</b>	<b>89</b>
	<b>Bibliography</b>	<b>90</b>
	<b>Declaration of originality</b>	<b>97</b>
	<b>Acknowledgements</b>	<b>99</b>
	<b>Index</b>	<b>99</b>

# List of Figures

1.1	Temporal evolution of the detachment of a drop. . . . .	6
1.2	Visualisation of inhibited scalar reconnection. . . . .	7
1.3	Visualisation of possible scalar reconnection. . . . .	7
1.4	Different scales involved in the boundary layer analysis. . . . .	12
1.5	The stability parameter depending on the wave number. . . . .	13
1.6	Qualitative structure of a magnetic island. . . . .	18
2.1	Microscopic particle dynamics in kinetic and gyrokinetic theory. . . . .	20
2.2	Visualisation of gyrokinetics concepts. . . . .	21
3.1	Temporal evolution of the perturbed field energy. . . . .	28
4.1	Schematic representation of magnetic equilibrium I. . . . .	32
4.2	Comparison of stability parameters of different equilibria. . . . .	33
4.3	Slab geometry implemented in EUTERPE . . . . .	35
4.4	Benchmark of the shear Alfvén wave. . . . .	37
5.1	Linear benchmark of the tearing mode eigenfunctions. . . . .	45
5.2	Linear benchmark of tearing mode growth rates. . . . .	46
5.3	Analytic dispersion relation compared with the exact growth rate. . . . .	47
5.4	Linear benchmark of the drift tearing mode growth rate. . . . .	49
5.5	Linear benchmark of the drift tearing mode frequency. . . . .	50
5.6	Growth rates of the tearing mode depending on $\eta$ . . . . .	51
5.7	Critical $\eta$ depending on $\beta$ . . . . .	52
6.1	Diagnostic quantities describing the saturated mode ( $a = 0.6$ ). . . . .	56
6.2	Diagnostic quantities describing the saturated mode ( $a = 0.5$ ). . . . .	58
6.3	Saturated island half widths compared with the analytical prediction. . . . .	59
6.4	Linear growth rate supporting the discussion of Fig. 6.3. . . . .	60
6.5	Diagnostics for super-exponential nonlinear reconnection (1). . . . .	61
6.6	Diagnostics for super-exponential nonlinear reconnection (2). . . . .	63
6.7	Evolution of the current profile compared with initial profile (1). . . . .	64
6.8	Evolution of the current profile compared with initial profile (2). . . . .	65
6.9	Oscillation frequency $\omega_B$ depending on the wave vector. . . . .	67
6.10	Oscillation frequency $\omega_B$ and growth rate depending on $a$ . . . . .	68
6.11	Parameter scan ( <i>i</i> ) of non-saturating modes. . . . .	70
6.12	Parameter scan ( <i>ii</i> ) of non-saturating modes. . . . .	72
7.1	Linear benchmark of the gyrofluid eigenfunctions. . . . .	77

7.2	Linear benchmark of the gyrokinetic eigenfunctions. . . . .	78
7.3	Linear benchmark of the dispersion relation of both models. . . . .	78
7.4	Comparison of the linear dispersion relations (case I, II). . . . .	80
7.5	Comparison of the codes including FLR effects (case II, 1). . . . .	80
7.6	Comparison of the codes including FLR effects (case II, 2). . . . .	81
7.7	Evolution of the island half widths for both codes (case I). . . . .	83
7.8	Evolution of island half width obtained with the gyrofluid code . . . . .	84
7.9	Comparison of the saturated island half widths (case I, II). . . . .	85
7.10	Saturated island half widths compared with the analytical prediction. . . . .	86
7.11	Comparison of the oscillation frequencies (case I, II). . . . .	86
7.12	Comparison of the island half widths including FLR effects. . . . .	87

# List of Tables

1.1	Overview of analytic dispersion relations (1). . . . .	16
1.2	Overview of analytic dispersion relations (2). . . . .	17
1.3	Overview of analytic dispersion relations (3). . . . .	17
6.1	Overview of parameter values in both unit systems. . . . .	62
6.2	Overview of parameter values for equilibria I, II. . . . .	66
6.3	Overview of parameter values for scans (i), (ii). . . . .	69
6.4	Comparison of simulation results with available references. . . . .	71
7.1	Set of parameters defining setup I and II. . . . .	79



# Nomenclature

$k_B$	Boltzmann constant
$s$	species label, $s = (i, e)$
$m_s$	mass of species $s$
$q_s$	charge of species $s$ ( $q_e = -e$ , $q_i = e$ )
$T_{0,s}$	constant background temperature of species $s$ (equal to $T_0$ if $T_{0,i} = T_{0,e}$ )
$n_{0,s}$	constant background density of species $s$ (equal to $n_0$ if $n_{0,i} = n_{0,e}$ )
$\mu_s = m_i/m_s$	ratio of ion mass to species mass $m_s$ ( $\mu_e = \mu$ , $\mu_i = 1$ )
$\rho_i = \sqrt{m_i k_B T_{0,i}}/(eB)$	ion gyroradius
$\rho_{S,e} = \sqrt{m_i k_B T_{0,e}}/(eB)$	ion sound Larmor radius
$\Omega_s = q_s B/m_s$	Larmor frequency
$v_s = \sqrt{k_B T_{0,s}/m_s}$	thermal speed
$v_\perp$	perpendicular velocity
$\mu_B = v_\perp^2/(2B)$	magnetic moment per unit mass
$B$	absolute value of the equilibrium magnetic field
$\vec{b} = \vec{B}/B$	magnetic unit vector in direction of $\vec{B}$
$\bar{s}$	flux label
$A_0, \Psi_0$	background parallel magnetic vector potential
$p$	plasma pressure
$\beta_e = p/(B^2/2\mu_0)$	electron plasma beta as the ratio of electron pressure over magnetic pressure (short notation $\beta$ )
$\tau_s = T_{0,s}/T_{0,e}$	ratio of species temperature $T_{0,s}$ to electron temperature $T_{0,e}$ ( $\tau_i = \tau$ , $\tau_e = 1$ )

$v_A = B_{0,z}/\sqrt{\mu_0 n_0 m_i}$	Alfvén speed based on the guiding field strength $B_{0,z}$
$L_{\text{eq},x} = x/\nabla x$	scale length of the equilibrium gradients of quantity $x$ , being density $n_{0,s}$ , temperature $T_{0,s}$ or magnetic field $B$
$t_A = L_{\text{eq},B}/v_A$	Alfvén time
$\eta_s = L_{n,s}/L_{T,s}$	ratio of temperature to density gradient scale
$\omega_{p,s} = \sqrt{n_s e^2 / (\epsilon_0 m_s)}$	plasma frequency
$d_s = c/\omega_{p,s}$	collisionless skin depth of species $s$
$\phi$	perturbed of the electrostatic potential
$A, \Psi$	perturbed parallel magnetic vector potential
$\omega$	complex eigenvalue of the mode
$\gamma = \gamma_k = \Im(\omega)$	growth rate of the mode as the imaginary part of $\omega$
$\hat{\omega} = \Re(\omega)$	frequency of the mode as the real part of $\omega$
$\vec{k} = (k_x, k_y, k_z)$	wave vector
$k_{\parallel} = \vec{k} \cdot \vec{B}$	parallel wave vector

# 1 Introduction

## 1.1 Magnetic reconnection

Magnetic reconnection is a fundamental process in plasma physics which describes the topological restructuring of magnetic field lines. Following a more general term, it is a change in magnetic connectivity of plasma elements due to the violation of the frozen-in magnetic flux constraint of ideal MHD theory [1, 2].

During reconnection the magnetic energy as a source of free energy is converted into kinetic energy of the plasma, thermal energy and acceleration of particles. It is believed to play a crucial role in astrophysics as a way for explaining solar eruptions, coronal mass ejections, stellar flares, coronal heating and the generation of energetic particles. It also affects high velocity clouds in the galactic halo [3]. Reconnection events were proven to occur in the magnetotail of the earth and mercury and theoretically investigated in these domains [1, 4–6].

A very important additional research part of reconnection physics concern the aspects relevant for fusion by magnetic confinement. Neglecting the ideal MHD approximation of fusion plasmas, resistive tearing mode instabilities can evolve relatively fast and can lead to a strongly reduced plasma confinement. Moreover, nonlinear aspects of these reconnection events can lead to a high acceleration of the tearing instability which has to be controlled in experimental devices [7].

A very recommendable overview of the field of magnetic reconnection and detailed discussions are given in Ref. [1]. For advanced studies Ref. [2] contains a collection of rather specialised reports. It gives also a short and valuable introduction to reconnection and related topological concepts.

The concept of magnetic reconnection was founded by Giovanelli (1946) trying to explain the heating of the solar corona. Also Dungey (1953) recognised that the large amount of magnetic energy on the surface of the sun can be a source of a sudden acceleration of charged particles. Solar flares and coronal mass ejections exhibit the clearest visual examples of magnetic reconnection. Soft  $X$ -ray images gave more experimental insight into the magnetic structures and acceleration of charged particles [5]. Recently the *RHESSI* satellite was launched (2002) to provide high resolution  $\gamma$ -spectroscopy images of the sun used to explain impulsive reconnection events on the sun's surface.

A more detailed physical picture of reconnection can be given by inspecting Ohm's law of the fluid model under consideration. In Sec. 1.2 the relevance of Ohm's law is described comprehensively in terms of a hydrodynamic analogon of magnetic reconnection.

## 1 Introduction

Within the non-ideal MHD plasma description one can assume [8]

$$\vec{E} + \vec{v} \times \vec{B} = \eta \vec{j} - \nabla p + d_e^2 \frac{\partial \vec{j}}{\partial t} + \frac{\vec{j} \times \vec{B}}{n e}. \quad (1.1)$$

This equation can be traced back to the momentum balance of the electron fluid in the derivation of the MHD model. It describes the response of the current  $\vec{j}$  under the influence of an electric field  $\vec{E}$ . Here,  $n$ ,  $\vec{v}$  and  $p$  are the plasma density, velocity and scalar pressure, respectively. There are several strong restrictions when applying this law in the MHD context [1].

Neglecting the right hand side of Eq. (1.1) the plasma is ideal and the magnetic field lines are just guided with the plasma motion. The resistivity  $\eta$  and the inertia term proportional to  $d_e^2$  lead to a violation of the constraint of the frozen-in magnetic flux allowing the magnetic field to decouple from the plasma flow. The resistivity introduces dissipation in the system causing a conversion of magnetic energy into Joule heating. Without resistivity the system is dissipation-free and an effective impedance remains due to the finite electron inertia proportional to  $d_e^2$ . The pressure term does not support non-ideal effects since it is a gradient field. The pressure gradient here causes a process so-called slippage and has similar features of reconnection [2]. However, off-diagonal components of a pressure tensor can indeed break the frozen-in magnetic flux constraint [9]. The last part on the right hand site is known as Hall term. This term for itself does also not cause magnetic reconnection but makes Alfvénic waves dispersive (whistlers).

One of the earliest models, referred to as the Sweet-Parker (SP) model, describes a steady reconnection process within the resistive MHD context [1]. On the right hand side of Eq. (1.1) only the term proportional to  $\eta$  remains. A field line geometry which is antiparallel near the so-called singular layer underlies this model, motivated by modelling the complex magnetic dipole structures on the surface of the sun. It describes magnetic reconnection as a combination of a large scale ideal MHD-regime which accounts for the equilibrium length scales far away from the singular layer, and a thin non-ideal domain of width  $\delta_{\text{SP}}$  around the singular layer. Within this non-ideal diffusion domain the magnetic field lines are able to reconnect because the frozen-flux constraint is broken due to resistivity. The magnetic field diffuses into the layer, reconnects and accelerates the plasma along the singular layer in the elongated direction with an upstream-velocity  $v_{\text{A},up}$ . However, the elongated diffusion region of length  $\Delta$  limits the rate of reconnection due to the Alfvén limit on the ion outflow velocity. Assuming a steady-state reconnection in an incompressible plasma, the continuity equation yields for the inflow velocity [10, 11]

$$v_{in} \sim \frac{\delta_{\text{SP}}}{\Delta} v_{\text{A},up} \ll v_{\text{A},up}. \quad (1.2)$$

It relates the length  $\delta_{\text{SP}}$  of the diffusion region to the macroscopic elongated scale  $\Delta$  which causes the reconnection rate,  $v_{in}/v_{\text{A},up}$  to be relatively small. However, the comparison with experimental observations of the reconnection rate clearly failed since the approximations used in this theory are quite crude.

In the early 60ies this model has been improved by Petschek. He assumed that slow mode shocks in the Sweet-Parker outflow region greatly speed up the mass flow. As the external plasma crosses the shocks it is accelerated in the downstream direction. The structure of the shocks along the outflow direction is characterised by a new microscopic scale  $\Delta^*$ , and the macroscopic scale  $\Delta$  of the Sweet-Parker model. An analysis shows that the reconnection rate is increased by a factor of  $\sqrt{\Delta/\Delta^*}$ ,

$$v_{in} \sim \frac{\delta_{SP}}{\Delta} \sqrt{\frac{\Delta}{\Delta^*}} v_{A,up} \sim v_{A,up}. \quad (1.3)$$

Although the model of Petschek was impressive it is very controversial. Biskamp (1986) reported the results of numerical simulations which appeared to disprove the Petschek model. In particular, assuming constant resistivity over the whole simulation domain, the shocks emerged at distances much larger than predicted by Petschek [5].

The plasma in the solar corona can not always be considered as conductive. Collisionless mechanisms have been investigated leading to fast reconnection resulting in much higher reconnection rates compared to the resistive case which suites better the explanation of astrophysical observations. These mechanisms base, for instance, on inertia effects of the electrons breaking the frozen-in constraint [5]. This case corresponds to taking only the term proportional  $d_e^2$  of the right hand side of Eq. (1.1) into account. The influence of the Hall-term was investigated as well leading to an increase of the reconnection rate [2].

Experiments with fusion devices have also shown strong hints of reconnection phenomena, as was first observed by Goehler (1974) in tokamaks. So-called sawtooth crashes may occur, which have been observed by soft X-ray emissions. The electron temperature profile peaks and suddenly flattens. This has been explained by Kadomtsev (1975), assuming that the MHD helical mode with mode number  $m = 1$ ,  $n = 1$  displaces the equilibrium magnetic axis of the tokamak. After that the magnetic fields are allowed to reconnect at the  $q = 1$  surface with  $q$  the safety factor.

Since the 70ies the most intensively studied instability for the formation of X-points and reconnection is the tearing mode. It has attractive properties since there are collisionless and collisional variations. To describe reconnection in the magnetotail of the earth the collisionless tearing mode without a guiding field, often modelled by a so-called Harris configuration [12], has been established as a standard concept in magnetic reconnection physics. The tearing mode offers also the possibility to create spontaneous reconnection in contrast to forced reconnection driven by an external equilibrium flow.

In particular, it is important to extend the understanding of tearing modes in hot plasmas encountered in fusion devices which maintain a strong magnetic guiding field. Due to the high core temperature binary coulomb collisions can be neglected which makes the plasma highly conductive. Considering the confinement of fusion plasmas on large times scales the approximation of ideal MHD is not valid anymore. Waiting long enough, the magnetic field can diffuse perpendicular to the guiding

## 1 Introduction

field which makes the description of finite resistivity of the plasma necessary. One could suppose that the perpendicular magnetic diffusion causing destabilisation of the plasma is quite slow. Since the involved spatial scales are very small and a large amount of magnetic energy contained in the equilibrium can be released, the growth rate of the resistive tearing mode can be very high [13, 14]. The resistive tearing mode typically grows on a hybrid time scale  $\gamma_k^{-1} \sim t_A^{2/5} t_R^{3/5}$  between the short MHD time scale  $t_A$  and the very long resistive time scale  $t_R$ <sup>1</sup> [13].

Tearing modes are well known for the formation of magnetic islands which alter the magnetic topology and thus the confinement properties of fusion devices. The description of tearing modes can be extended by including electron temperature gradients. If additionally a sufficiently large resistivity is present so-called micro-tearing modes can be excited which form small scale islands [15, 16]. These modes trigger the stochastisation of magnetic islands causing a rapid deconfinement of the plasma.

From the 60ies until nowadays, the analytical work on tearing modes multiplied. The milestone work of Furth, Killeen and Rosenbluth (1963) within the resistive MHD context founded the linear boundary layer analysis of tearing modes [14]. They calculated the dispersion relation for the first time in terms of the stability parameter  $\Delta'$  describing the ideal solution on large scales outside the tearing layer. The famous analytical result of Rutherford (1973) stated the algebraic growth of the nonlinear resistive tearing mode [17]. During these decades the computational work concentrated mainly on fluid calculations. Sonnerup (1970) and Vasyliunas (1975) began to verify numerically that other solutions than Petschek's prediction exist in the regime of fast reconnection.

Drake and Lee (1977) used a drift kinetic model for both electrons and ions to predict collisionless and collisional linear dispersion relations in the low- $\Delta'$  limit [18]. Although quite early, this work is still a standard reference of present reports. Drake and Lee also proposed a nonlinear saturation mechanism of the tearing mode both without and with collisions [19]. The latter result confirmed the prediction of Rutherford.

During this period numerical work on simulations of kinetic models started which were discretised by particle-in-cell (PIC) methods. Katanuma (1980) investigated the nonlinear evolution of tearing modes in a slab [20]. However, this work focused on presenting a few single time series to enlight the physical saturation mechanism rather than a comprehensive numerical verification of available nonlinear predictions. Birdsall and Langdon (1985) seconded, but their approach included large spatial and temporal discrepancies of the scales involved (Debye length and system size, plasma frequency of the electrons and small growth rates) and thus made it intractable to obtain kinetic simulation results in a reasonable period of time. This numerical field gained much drive when the gyrokinetic equation derived by Hahm (1988) had been established. This kinetic description allows for tearing solutions circumventing the previously mentioned numerical disadvantages for simulations.

---

<sup>1</sup> The Alfvén time  $t_A = L_{\text{eq,B}}/v_A$  as well as the time of resistive diffusion,  $t_R = \mu_0 L_{\text{eq,B}}^2/\eta$  are related to the equilibrium magnetic field scale  $L_{\text{eq,B}}$ .

Porcelli (1991) succeeded in calculating a dispersion relation of the tearing mode with a fluid approach of the electrons and a gyrokinetic description of the ions. This dispersion relation includes diamagnetic effects, collisionality and finite ion temperature effects and still serves as a standard formula in benchmarking results of linear fluid simulations [21, 22]. Since the 90ies MHD modelling, minimal two-field and four-field models have seen explosive growth and usage due to the technological progress in computing power and numerical techniques [5, 23]. MHD codes could face demands of realistic 3D global domains like 3D simulations of earth's magnetosphere in the presence of the solar wind. The collaboration entitled Geospace Environmental Modeling (GEM) project enfolded several important results on numerical studies of two-fluid reconnection describing Earth's magnetosphere (Shay and Drake (1998), Daughton (2006)) [5].

Nonlinear studies by Aydemir (1992) discovered the so-called "explosive" reconnection when simulating the  $m = 1$  mode in a tokamak [7]. Using a four-field model in the high- $\Delta'$  regime and low collisionality he showed that in the early nonlinear phase the actual growth rate  $\gamma(t)$  of the tearing mode increases by one order of magnitude with respect to the linear growth rate  $\gamma_k$ . The strong increase of the reconnection rate in the early nonlinear phase was confirmed by Ottaviani (1993) and Kleva (1994) in the high- $\Delta'$  regime within a slab model [23]. A physical mechanism explaining this acceleration could not worked out but a heuristic differential equation describing the island evolution was derived. An comprehensive nonlinear theory explaining this subject is still under discussion [35].

Grasso (1999) extended the model of Ottaviani by taking finite Larmor radius (FLR) effects into account [21]. The numerical investigation included the dependency of the field structure of the tearing mode on finite ion temperature as well as the acceleration of the amplitude in the early nonlinear phase.

Progress has also been made investigating secondary island formation (plasmoids) using a resistive MHD model employing a turbulent background [45]. For sufficiently small resistivity the reconnection rate becomes independent from collisionality. Recently, a kinetic hybrid model was used to figure out numerically that Landau-damping can be mainly responsible for electron heating during two-dimensional reconnection [46, 47]. In particular, the width of the saturated island half width is found to be the same as predicted in MHD theory for sufficient large system sizes.

## 1.2 Preparation for reconnection: A hydrodynamic analogon

This chapter prepares for magnetic reconnection within a pure hydrodynamic context describing the detachment of a liquid drop. This chapter here follows mainly the work of [2, 48].

The term reconnection is not restricted to processes which involve electromagnetic fields. It can appear in a very general fashion, for instance, describing non-ideal processes within hydrodynamics. In the following example, the dynamical magnetic vector field  $\vec{B}$  is translated into a generic smooth scalar quantity  $P$  as shown in

## 1 Introduction

Figure 1.1 which can be thought of as a colour or density of a fluid. The Figure might show a fluid, where the white, lighter phase is associated to  $P = 0$  and the black, heavier phase to  $P = 1$ , whereas in between the quantity undergoes a smooth transition. The temporal evolution of this unstable configuration is depicted from left to right. The flow  $\vec{v}$  is a solution of the Navier-Stokes equations, while  $P$  is assumed to be just advected with the local flow, i.e. being described by a transport equation

$$\frac{\partial P(\vec{x}, t)}{\partial t} + \vec{v} \cdot \nabla P(\vec{x}, t) = 0. \quad (1.4)$$

However, the detachment can never be achieved using Eq. (1.4). To describe detachment, the boundary of the  $P = 1$  domain must be advected to the stagnation point in a finite time. This is not possible for any smooth velocity field. The flow at the

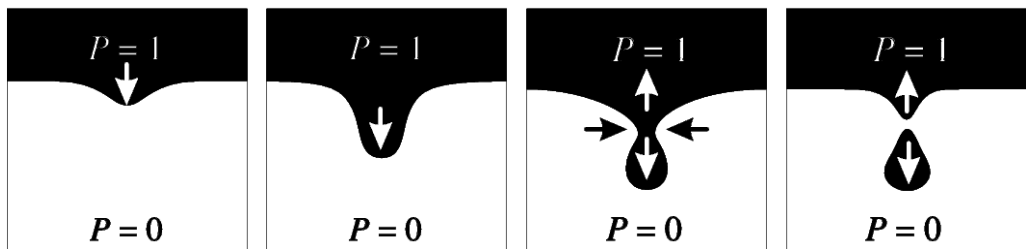


Figure 1.1: Temporal evolution of the detachment of a drop as an example of scalar reconnection. The Figure is taken from Ref. [48].

stagnation point  $x = 0, y = 0$  can be well approximated by  $\vec{v} = (-x, y, 0)$ . The time for transporting a fluid element over the last distance  $\epsilon$  to the stagnation point is

$$\Delta t = \int_{\epsilon}^0 \frac{1}{v_x} dx = \int_0^{\epsilon} \frac{1}{x} dx = \ln(x)|_0^{\epsilon} = \infty. \quad (1.5)$$

This situation is again shown in Figure 1.2, but in contrast to Figure 1.1 the coordinate system is rotated by  $\pi/2$ .

In reality the detachment is of course quite possible. The physical reason for the contradiction is that the description by Eq. (1.4) fails during the detachment. In nature the decreasing thickness of the  $P = 1$  domain reaches molecular distances in finite time and at least then it is not clear whether a fluid description can be maintained. To stay within the macroscopic fluid description and to account tentatively for the detachment, one can introduce a correction term in Eq. (1.4). It is not assured that this concept will be successful, since on those small scales involved the complex particle dynamics should be better described by a kinetic model. Adding a generic non-ideal term  $r$  to Eq. (1.4) one obtains

$$\frac{\partial P(\vec{x}, t)}{\partial t} + \vec{v} \cdot \nabla P(\vec{x}, t) = r(\vec{x}, t). \quad (1.6)$$

The only condition is that  $r$  must be small compared to the advection term, excluding the points, where the advection term vanishes. This equation will be the analogon of Ohm's law Eq. (1.1) and  $r$  can be translated to the term proportional

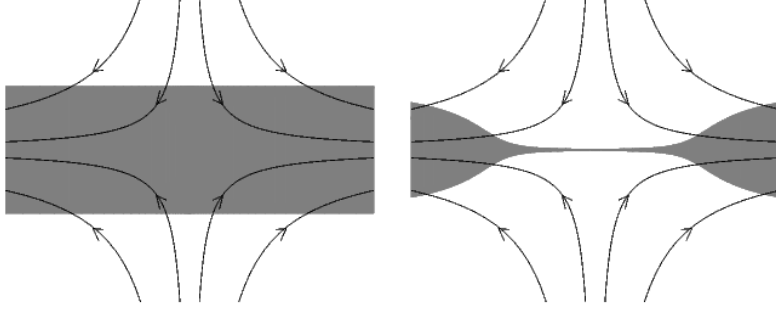


Figure 1.2: The reconnection process is not possible in finite time with an ideal transport equation for  $P$ . The Figure is taken from Ref. [48].

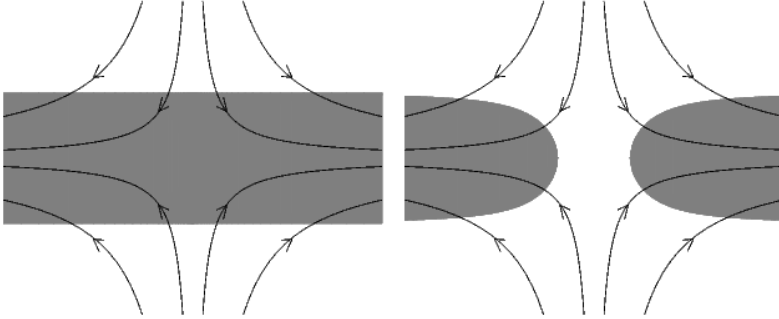


Figure 1.3: The reconnection process is now possible in finite time with non-ideal effects  $r$  in the transport equation of  $P$ . The Figure is taken from Ref. [48]

to the resistivity  $\eta \vec{j}$ . The exact form of  $r$  almost plays no role. Eq. (1.6) can be rewritten as

$$\frac{\partial P(\vec{x}, t)}{\partial t} + \vec{w} \cdot \nabla P(\vec{x}, t) = 0, \quad (1.7)$$

assuming  $r = -\delta \vec{v} \cdot \nabla P$  and defining  $\vec{w} = \vec{v} + \delta \vec{v}$ . The new velocity  $\vec{w}$  is not smooth since  $\nabla P$  vanishes at the point of detachment where  $r \neq 0$ . It requires a singularity in  $\delta \vec{v}$  and consequently in  $\vec{w}$  of the type  $|\delta \vec{v}| \sim 1/|\nabla P|$ .

Indeed, for a generic saddle point of the form  $P \sim a - bx^2 + cy^2$  detachment becomes possible as shown Figure 1.3. Since the singularity of the flow scales like  $w_x \sim -1/x$  with respect to the  $x$ -direction this leads to the estimation of the travel time

$$\Delta t = \int_{\epsilon}^0 \frac{1}{w_x} dx = \frac{\epsilon^2}{2}, \quad (1.8)$$

which is now finite.

### 1.3 Current research and motivation for this work

At the very first magnetic reconnection is a numerical and analytical challenge. Even global simulations in a slab geometry are still attractive and frequently used for investigations [25, 26]. The relative simple slab geometry admits the investigation of fundamental physical mechanisms of reconnection caused by the highly nontrivial aspects of boundary layer dynamics.

In this work the standard gyrokinetic equation are solved to model reconnection with a modern kinetic approach [27]. The gyrokinetic equation is solved by means of a  $\delta f$ -PIC method implemented in the EUTERPE code. This high performance and fully paralised code is an advanced tool for full gyrokinetic plasma simulations [28]. EUTERPE can provide a detailed view on the phase space dynamics which is a unique benefit in contrast to fluid models that are often forced to use a defined physics specified by the applied closures schemes. Since reconnection simulations are accompanied with a high computational effort the PIC scheme itself has to be compared by frequently used kinetic continuum codes, which tend to be rather slow due to high resolution of the multi-dimensional phase space [29, 31–33].

The numerical investigation of linear tearing modes is still a current topic of magnetic reconnection in the low- $\beta$  regime. However, numerically exact benchmarks of simulation results are a challenging task, rather it is common to compare with less exact analytic dispersion relations [29, 30]. This work shows that EUTERPE is able to simulate linear reconnection processes to very high accuracy by comparing with an adopted shooting method. Moreover, the performance of linear simulations verify that the computationally “cheap” PIC scheme is suitable for reconnection simulations.

There is a tremendous lack of simulation results of physically important parameter regimes concerning tearing modes. This can be traced back to the high number of relevant spatial scales which are able to modify the reconnection process sensitively. For instance, in the range of fast reconnection employing electron temperature gradients, the linear tearing mode has not been much investigated so far. In the presence of equilibrium gradients of length scales  $L_{T,e}$ ,  $L_{n,e}$  a critical threshold of  $\eta = L_{n,e}/L_{T,e}$  occurs and is not quite well understood. Closely connected to finite equilibrium gradients in the presence of reconnecting events is the investigation of micro-tearing modes, which are important for understanding electron transport during island formation. The numerical description of micro-tearing modes with PIC methods is not well developed.

An important point marks the nonlinear saturation of the tearing mode which is also a key feature of the present work. Since a coupling of the most unstable mode to modes with higher poloidal mode numbers is not expected, it is a very well arranged situation to observe the single-mode evolution. In contrast to, for instance, ITG-modes which can drive turbulent plasmas exciting a whole spectrum of interacting modes, analytical predictions of the saturated island half width of nonlinear single tearing modes are easier to validate, but not proved numerically so far for a broad range of parameters. Only rare systematic numerical investigations of the saturated island half width are available in the literature [26]. Either the weak col-

lisional regime has been investigated [47] or high- $\beta$  cases [30] which do not match the present purposes. The comparison of predictions of the saturated island half width [19] with numerical simulations is a further important contribution of this thesis.

Nonlinear tearing in terms of Hamiltonian fluid models has been discussed at length both in the high- and low- $\Delta'$  regime [42–44]. Despite of the wealth of numerical results obtained so far reasonable predictions like saturated island width depending on important plasma parameters are missing. The Hamiltonian fluid equations can be formulated in terms of topological invariants which might enhance analytical work. However, even this class of more intuitive models compared to pure kinetic approaches are still investigated rather numerically and show a lack of analytical work on nonlinear reconnection.

The need for simulation results and physical understanding becomes even more necessary in the high- $\Delta'$  regime. Early attempts of the theoretical description of nonlinear destabilisation in the high- $\Delta'$  regime started with fluid simulations and semi-analytical statements based on the evaluation of the vector potential and plasma flow pattern [23]. Important progress has been achieved in understanding nonlinear destabilisation mechanism by applying the energy principle on a two-fluid model in the high- $\Delta'$  [35]. However, in general this range of fast reconnection is harder to treat numerically the higher  $\Delta'$ . In this thesis the focus lies on the transition between the saturated phase and nonlinear destabilisation to get deeper insight into the difference of both regimes circumventing the range of large values of the stability parameter. Although a final answer to the physical mechanism of acceleration can not be given this transition will be one of the most interesting fields in nonlinear tearing physics. Attacking these simulations in real three-dimensional geometries would be a delicious task and is left for further work.

Since the last two decades reconnection was mainly investigated by fluid simulations [21, 23, 36]. Due to the influence of kinetic effects like finite Larmor radius effects or dominating phase space dynamics like superthermal particle acceleration on linear reconnection, a comparison between kinetic and fluid simulations is necessary. Beside kinetic effects, it is still not clear whether fluid models contain nonphysical effects like artificial saturation with respect to kinetic approaches when entering the nonlinear phase of reconnection [34]. During the last decade mainly two branches of gyro-flavoured models dominated magnetic reconnection physics: in the late 80ies the gyrokinetic approach came up as a standard tool in plasma physics [27]. In the early 90ies gyrofluid models were derived from the gyrokinetic equation and simplified versions of these models were used intensively in strongly magnetised plasmas [34, 37, 40]. These fluid models were also collated with arbitrary guide-field models in low- $\beta$  limits [41]. After proposing and deriving these models a comprehensive comparison of these different models is needed, especially with the original gyrokinetic equation. Linear comparisons of fluid and gyrokinetic approaches have been performed both in a low- and high- $\beta$  slab configuration [32, 38, 39]. However, an exact benchmark has not been presented as well as a systematic comparison of both models in the nonlinear regime. This thesis is also dedicated to a systematic comparison of the standard gyrokinetic model and a compressible gyrofluid model [51]

both in the linear and nonlinear regime. When focussing on linear simulations both approaches are accompanied with numerically exact benchmarks.

## 1.4 Collisionless tearing mode instability

The tearing mode is a non-steady spontaneous electromagnetic instability causing magnetic reconnection. Even if a plasma is stable with respect to ideal MHD, non-ideal effects can make the plasma unstable. The dynamics of this instability is mainly influenced by a very thin diffusion region of the order of the collisionless electron skin depth  $d_e$  where non-ideal effects become important. In the following a calculation of the linear growth rate  $\gamma$ , in a similar fashion as Ref. [13], but within the context of a simplified electron fluid model in a magnetised plasma is given to get in touch with boundary layer and tearing mode physics.

### 1.4.1 The linear tearing mode

The simplest configuration of a magnetic field  $\vec{B}_0 = (0, B_{0,y}, B_{0,z})$  in a slab which is tearing unstable, is provided by an equilibrium current of amplitude  $j_{0,z}$  and width  $a$ , flowing in the direction of the guiding field  $B_{0,z} \hat{e}_z$ . The only non-zero perpendicular component of the magnetic field is then given by

$$B_{0,y}(x) = \begin{cases} B'_{0,y} x & -a < x < a \\ -B'_{0,y} & x < -a \\ B'_{0,y} & x > a. \end{cases} \quad (1.9)$$

Usually the derivative of the magnetic field  $B'_{0,y}(0)$  is expressed in terms of the shear length defined by  $l_s = B_{0,z}/B'_{0,y}(0)$ .

This equilibrium is MHD stable, but introducing non-ideal effects like electron inertia makes it unstable. The resulting diffusion of the magnetic field lines leads to a new magnetic configuration and is expected to be of high influence at a resonant surface defined by the condition  $k_{\parallel}(x) = \vec{k} \cdot \vec{B}_0(x) = 0$ .

A simple model which supports magnetic reconnection is an electron fluid model given by the equations of motion [51]<sup>1</sup>

$$0 = \frac{\partial n_e}{\partial t} + [u_e, \Psi], \quad (1.10)$$

$$0 = \frac{\partial (\Psi - d_e^2 u_e)}{\partial t} - \rho_{S,e}^2 [n_e, \Psi], \quad (1.11)$$

$$u_e = \Delta \Psi, \quad (1.12)$$

---

<sup>1</sup>The equations are normalised to Alfvén units. This normalisation procedure is described in Sec. (4.1). The model originates from a more general gyrofluid model. Here only electrons are taken into account.

where  $n_e$  denotes the density,  $u_e$  the current density of the electrons and  $\Psi$  the magnetic flux. Eq. (1.12) is parallel Ampère's law. The electron skin depth  $d_e$  in Ohm's law, Eq. (1.11), is retained in order to provide a physical mechanism for breaking the frozen-in constraint. The electron continuity equation, Eq. (1.10), closes the system. The Poisson bracket for two arbitrary fields  $f, g$  is defined by  $[f, g] = \vec{b} \cdot \nabla f \times \nabla g$ .

To investigate the linear tearing mode, Eqs. (1.10–1.12) are linearised keeping only terms proportional to the fluctuating fields. The Fourier ansatz  $\Psi_1 \sim e^{i(k_y y - \omega t)}$  for the perturbed magnetic flux and analogously for  $u_e$  and  $n_e$  relates the eigenvalue  $\omega$  to the wave number  $k_y$ . The following calculation deals only with two-dimensional reconnection setting  $\partial_z = 0$  for the perturbations, so the resonant surface is located at  $x = 0$ . The linearised equations are

$$\begin{aligned} 0 &= \omega n_1 + k_y \left( -\frac{\partial_x^3 \Psi_0}{\partial_x \Psi_0} \Psi_1 + \partial_x^2 \Psi_1 - k_y^2 \Psi_1 \right) \partial_x \Psi_0, \\ 0 &= \omega (\Psi_1 - d_e^2 [\partial_x^2 \Psi_1 - k_y^2 \Psi_1]) + \rho_{S,e}^2 n_1 k_{\parallel}. \end{aligned} \quad (1.13)$$

A possible equilibrium vector potential  $\Psi_0$  representing setup Eq. (1.9) is given by

$$\Psi_0(x) = \begin{cases} -x^2/(2l_s) & -a < x < a \\ x/l_s + 1/(2l_s) & x < -a \\ -x/l_s + 1/(2l_s) & x > a. \end{cases} \quad (1.14)$$

After eliminating the density response  $n_1$ , the final differential equation becomes

$$\begin{aligned} 0 &= \omega^2 (\Psi_1 - d_e^2 [\partial_x^2 \Psi_1 - k_y^2 \Psi_1]) \\ &+ \rho_{S,e}^2 k_{\parallel}^2 \left( -\frac{\partial_x^2 B_{0,y}}{B_{0,y}} \Psi_1 + [\partial_x^2 \Psi_1 - k_y^2 \Psi_1] \right) \end{aligned} \quad (1.15)$$

It is quite possible to solve this eigenvalue equation straightforward numerically to get the complex eigenvalue  $\omega$  and the eigenfunction  $\Psi_1$ . However, this does not illuminate the physical picture behind reconnection.

The problem of calculating the growth rate can be solved approximately by accounting directly for the domains which differ strongly regarding the relevant physics. The approximative solution of the eigenvalue problem rests upon a distinction between the outer ideal (reduced) MHD region and the inner diffusion region. The motivation for this strategy can be explained by inspecting the typical eigenmode structure, shown in Figure 1.4. The equilibrium magnetic length  $a$ , obeying typically  $a \ll L_x$ , is the largest scale in the system and is related to the outer solution. Although Eq. (1.15) is always valid, the non-ideal term proportional to  $d_e$  can be neglected on the scale  $a$ . The differential equation simplifies and its solution describes the outer part. In contrast to the outer domain the spatial structure of the mode mostly varies close to the resonant surface due to the creation of a perturbed current sheet of width  $\delta_e$  deforming the eigenmode on the small scale  $d_e$ . At this distance the non-ideal effects can not be neglected anymore which motivates the derivation of an inner layer differential equation coming from Eq. (1.15). The resulting differential

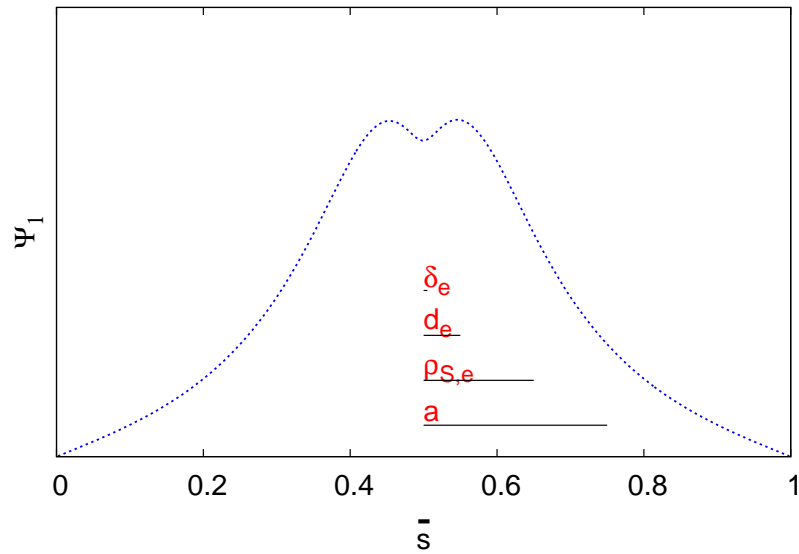


Figure 1.4: Different scales involved in boundary layer analysis of the tearing mode. The outer ideal MHD solution varies slowly on  $a$ . The strongly varying structure around  $\bar{s} = 0.5$  is caused by the perturbed electron current channel of width  $\delta_e$  and typically scales with  $d_e$ .  $\rho_{S,e}$  represents the distance at which the pressure profile changes.

equation accounts for magnetic field line diffusion.

Since the outer region is governed by the ideal MHD description and this solution varies on the length scale of the magnetic equilibrium  $x \sim a \sim k_y^{-1}$  it is assumed that it is much larger than all remaining scales, thus  $d_e, \rho_{S,e} \ll a$ . The ideal MHD equation follows then from Eqs. (1.15) by neglecting the term proportional to  $\omega$ <sup>1</sup> resulting in

$$\partial_x^2 \Psi_1 = \left( k_y^2 + \frac{\partial_x^2 B_{0,y}}{B_{0,y}} \right) \Psi_1. \quad (1.16)$$

This differential equation is qualitatively different from Eq. (1.15). The magnetic equilibrium is divided into three domains according to Eq. (1.9), for which one has to solve Eq. (1.16) together with the proper boundary conditions in between. Here the differential equation is trivial to solve and gives an exponentially decaying solution for  $x > a$  and  $x < -a$ . This reflects the spatially localised character of the eigenmode also on the equilibrium scale  $a$ . If  $a \ll L_x$ <sup>2</sup>, the boundary conditions of the eigenmode play a minor role. The solution  $\Psi_1$  is characterised by a jump in the

<sup>1</sup> In the ideal MHD domain the Alfvén time is much shorter than the time scale of the tearing mode, thus  $|\omega| \ll 1$ .

<sup>2</sup> This is the usual ordering of the magnetic equilibrium scale and extent of the system size.

slope at the resonant surface <sup>3</sup> [13],

$$\Delta' = \frac{1}{\Psi_1} \left( \left. \frac{\partial \Psi_1}{\partial x} \right|_{x=+0} - \left. \frac{\partial \Psi_1}{\partial x} \right|_{x=-0} \right). \quad (1.17)$$

The linear stability parameter  $\Delta'$  is an important quantity in the context of tearing mode analysis. It allows to compare roughly different equilibria using only one value.  $\Delta'$  is a function of  $k_y$ ,  $a$  and the extension of the domain  $L_x$ . It contains the whole equilibrium geometry and scale of the perturbations  $k_y$  under consideration, even for more complex global domains like a tokamak.

The value  $\Delta'$  can be calculated analytically for the specific slab equilibrium used here, Eq. (1.9), giving [13]

$$\Delta'(k_y a) = \frac{2k_y a (e^{-2k_y a} - 2k_y a + 1)}{e^{-2k_y a} + 2k_y a - 1}. \quad (1.18)$$

The system size  $L_x$  does not appear in this expression, since it is assumed that  $L_x \gg a$  and so  $\Psi_1$  decays fast enough to suppress the influence of the boundary conditions. The dependency  $\Delta'(k_y a)$  is shown in Figure 1.5 for  $a = 1$ . The mode becomes unstable, if this quantity is positive, otherwise it is stable. For wave vectors  $k_y > 0.64$  the reconnection process is inhibited.

It is important to note that many currently used equilibria in the literature follow the same qualitative structure as described in Eq. (1.9) and so  $\Delta'$  differs not much.

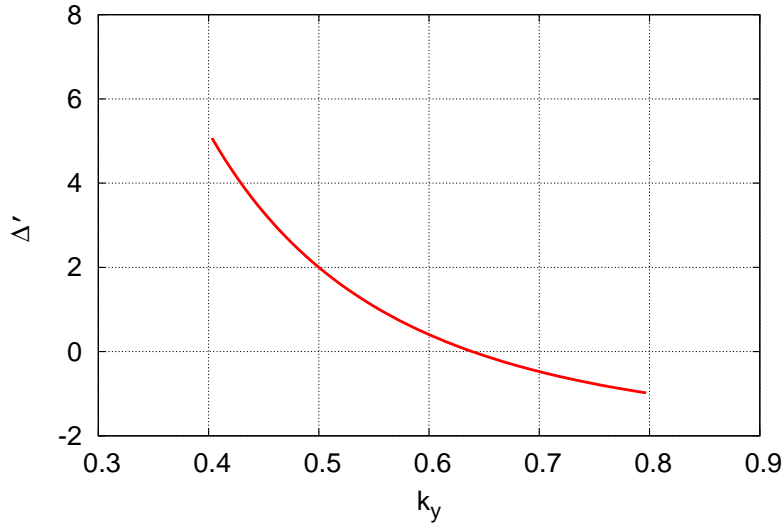


Figure 1.5: The tearing mode stability parameter depending on  $k_y$ . For  $k_y > 0.64$  the mode becomes stable.

The instability is mainly influenced by the thin current channel of width  $\delta_e$  at the

<sup>3</sup> One can show that also outer solutions of Eq. (1.16) exist which do not have a jump at  $x = 0$ . However, these modes are physically not relevant [13].

## 1 Introduction

resonant surface which is driven by a parallel electric field  $E_{\parallel}$ . Ideal MHD does not contain this quantity and so the ideal solution has to break down when approaching the layer  $|x| \rightarrow 0$ . The current layer serves as a kind of surface current  $j_{z,1}$  “seen” by the outer scale  $a$  which produces the jump in  $\partial_x \Psi_1$ .

Since  $\Psi_1$  must be differentiable, it cannot have a jump in the slope at all. The inner layer solution scales with  $\delta_{in}$  which will be defined later. This length resolves the current channel correctly. Far away from the current channel with respect to the small scale, i. e.  $|x| \gg \delta_{in}$  but nevertheless  $\delta_{in} \ll a$ , the inner solution will match asymptotically the outer solution to produce a smooth  $\Psi_1$  in the whole domain. Close to the resonant layer  $x \approx d_e$  the skin term in Eq. (1.15) and the strong variation of  $\Psi_1$  ( $\partial_x \gg k_y$ ) becomes dominant. This modifies the differential equation (1.15) qualitatively describing now the small scale dynamics with

$$-\partial_x^2 \Psi_1 (\gamma^2 d_e^2 + \rho_{S,e}^2 k_{\parallel}^2) + \gamma^2 \bar{\Psi}_1 = 0. \quad (1.19)$$

Usually it is assumed that the equilibrium magnetic field is a linear function close to the resonant surface,  $B_{0,y} \sim x/l_s$ . The second term on the left hand side of Eq. (1.19) contains the assumption of a constant value of the perturbed magnetic flux,  $\bar{\Psi}_1$ , reflecting the constant- $\Psi$  approximation across the layer. This assumption is only valid in the limit of marginal instability and clearly not applicable in the case  $\Delta' \gg 1$ . The characteristic length scale  $\delta_{in}$  can be estimated by balancing the first two terms of Eq. (1.19) giving  $\delta_{in} = (l_s \gamma d_e) / (\rho_{S,e} k_y)$ . Also one can show that the tearing mode is purely growing ( $\hat{\omega} = 0$ ), since there are no equilibrium gradients of temperature or density [13, 26].

Finally, both the solutions of the singular layer differential equation, Eq. (1.19) and the ideal solution from Eq. (1.16), will be combined to describe the mode structure over the whole domain  $L_x$  in order to get the final dispersion relation. In the following the method of asymptotic matching will be applied. First one rescales the inner solution according to  $X = x/\delta_{in}$ , assuming that  $\delta_{in}$  is arbitrary small with respect to  $a$ . In terms of the variable  $X$ , the stability parameter, Eq. (1.17) becomes

$$\Delta' = \frac{1}{\bar{\Psi}_{1,x}} \int_{-\infty}^{\infty} dX \frac{d^2 \Psi_{1,x}}{dX^2}. \quad (1.20)$$

This expression can also be formulated by integrating the differential equation of the layer, Eq. (1.19), respecting the redefined coordinate  $X$ ,

$$\begin{aligned} \frac{1}{\bar{\Psi}_{1,x}} \int_{-\infty}^{\infty} dX \frac{d^2 \Psi_{1,x}}{dX^2} &= \frac{\delta_{in}}{d_e^2} \int_{-\infty}^{\infty} dX \frac{1}{1+X^2} \\ &= \frac{\delta_{in}}{d_e^2} \pi. \end{aligned} \quad (1.21)$$

This expression makes contact with  $\Delta'$  of the ideal solution, Eq. (1.20), in the asymptotic limit. Knowing this value for a particular magnetic geometry, the growth

rate can be calculated as

$$\gamma = \Delta' \frac{\rho_{S,e} k_y d_e}{\pi l_s}, \quad (1.22)$$

which agrees with Porcelli [49] in the limit  $\Delta' \rightarrow 0$ . It makes also clear that the distance  $\delta_{in}$  scales as  $\delta_{in} \sim \Delta' d_e^2$  which is also known from kinetic theory of collisionless reconnection [18]. If  $d_e$ , and thus the non-ideal term of Eq. (1.11) vanishes, the mode becomes stable ( $\gamma = 0$ ). Also, if the strength of the sheared magnetic field becomes arbitrary small,  $l_s \rightarrow \infty$ , reconnection can not act, since only the homogeneous guiding field remains.

This analytical eigenvalue analysis shows that the tearing mode is a non-steady reconnection process which involves boundary layer dynamics. Many strongly differing, but physically important scales are involved. This insight would clearly not be possible when simply integrating Eq. (1.15) numerically.

The model equations (1.10–1.12), serve as a starting point for more complicated analyses. The inclusion of the electrostatic potential  $\phi$  into the dynamics leads to a coupled system of differential equations of fourth order [41, 50]. Additionally, the ions can be included as well, but due to the large natural mass ratio  $\mu$ , they play a minor role in the dynamics. The complete model from which Eq. (1.10–1.12) can be deduced [51], states that the plasma is advected with the flow  $\vec{v}_E = -\nabla \phi \times \vec{B}$ . Therefore, a second differential equation for the electrostatic potential has to be included, thus  $\phi$  is now also subject to a boundary layer problem that scales typically with  $\rho_{S,e}$  [43].

Consequently, the complete analytic calculation of the growth rate has to handle a double boundary layer analysis discriminating additionally the cases  $d_e > \rho_{S,e}$  and  $d_e < \rho_{S,e}$  assuming  $\rho_{S,e} \ll a$  as well. Usually the analytical work consists of applying a generalised Fourier transformation to the initial differential equations for  $A$  and  $\phi$  as well as a subsequent identification of the layer regions and several matching procedures of the fields [41, 49]. In this analysis it is customary to deal not only with the limit  $\Delta' d_e \rightarrow 0$  when matching both inner and outer solutions, but also with the opposite case  $\Delta' d_e \gg 1$ . This results in the application of a generalised asymptotic boundary condition for both fields  $\Psi_1$  and  $\phi$  when approaching the resonant layer [49, 52].

## 1.4.2 Overview of analytical dispersion relations

There is a large amount of analytical calculations of the dispersion relation of collisionless tearing modes because of subtle relations between parameters and the underlying type of models. This section gives an overview of available dispersion relations for collisionless tearing modes in low- $\beta$  configurations.

As a general remark the tearing mode stability parameter  $\Delta'$  plays a key role when classifying dispersion relations and comparing magnetic equilibria. In general the

## 1 Introduction

large- $\Delta'$  range is defined by the inequality [10]

$$\Delta' d_e > \left( \frac{d_e}{\rho_{S,e} \sqrt{1 + \tau}} \right)^{1/3}. \quad (1.23)$$

The opposite case is referred to as small- $\Delta'$  range. Parameter values frequently used in this work correspond to the estimate  $d_e \lesssim \rho_{S,e}$  and therefore the small- $\Delta'$  region is then characterised by  $\Delta' d_e \ll (d_e/\rho_{S,e})^{1/3} \approx 1$  for vanishing ratio of ion to electron temperature.

In Table (1.1) recent and for this work important references are shown that investi-

$L_{T,n} = 0, \tau = 0$	[21, 38, 41], Eq. (1.22)
$L_{T,n} = 0, \tau \approx 1$	[38]
$L_{T,n} \approx 1, \tau = 0$	[18, 56]
$L_{T,n} \approx 1, \tau \approx 1$	[49, 54, 57]

Table 1.1: References of analytic dispersion relations for the collisionless tearing mode.

gate collisionless reconnection with either a kinetic, fluid or hybrid approach. In this thesis the influence of finite ion temperature effects,  $\tau \approx 1$  on the tearing mode will be subject to simulations. For finite equilibrium scales of density and temperature in the simulation domain,  $L_{n,s} \approx 1$  and  $L_{T,s} \approx 1$ , the tearing mode gets a finite oscillation frequency  $\hat{\omega}$  [18, 44, 56].

The ratio  $d_e/\rho_{S,e} = 1/\sqrt{\beta\mu}$  and related cases  $d_e^2 \gg \rho_{S,e}^2$  ( $\beta \ll m_e/m_i$ , "inertia regime") and  $d_e^2 \ll \rho_{S,e}^2$  ( $\beta \gg m_e/m_i$ , "kinetic regime") define certain limits of validity of dispersion relations [51]. The analytic work of reference [50] using a two-fluid model includes linear dispersion relations valid for arbitrary guiding field strengths and may serve as a demonstrating explanation. The authors apply matched asymptotic expansion techniques which include the identification of different physical structures around the resonant layer depending on  $\beta$ . At very small plasma- $\beta$  values obeying  $\beta \ll m_e/m_i$ , ion and electron flow are coupled in the tearing layer width yielding a single MHD fluid description. For finite plasma- $\beta$  ( $\beta \lesssim (m_e/m_i)^{1/4}$ ), electrons and ions are decoupled on scales smaller than  $\rho_{S,e}$ . The mode is then referred to as kinetic Alfvén-driven tearing instability. Two sublayers are present: a narrow layer of width  $d_e$  where electron diffusivity is important and a two-fluid specific layer on scales  $\rho_{S,e}$ . If  $\beta \gg (m_e/m_i)^{1/4}$  reconnection is influenced by whistler waves and not of interest here. In Table (1.2) dispersion relations are shown valid for  $\tau = 0$  and  $L_{T,n} = 0$  in various limits <sup>1</sup>.

For the case  $\rho_{S,e} > d_e$  Table (1.3) lists the growth rates and real frequencies of the tearing mode in a slab configuration. In the case  $\Delta' d_e < 1$  an algebraic equation

<sup>1</sup> In Ref. [10] a short overview of linear dispersions is given in this regime. The original results were developed in Refs. [55, 56]

$L_{T,n} = 0, \tau = 0$	$\rho_{S,e} < d_e$ [10]	$\rho_{S,e} > d_e$ [38]
$\Delta' d_e < 1$	$\gamma = 0.22 \cdot k_y d_e^3 \Delta'^2 / l_s$	$\gamma = k_y d_e \rho_{S,e} \Delta' / (\pi l_s)$
$\Delta' d_e > 1$	$\gamma = k_y d_e / l_s$	$\gamma = k_y (2d_e / \pi)^{1/3} \rho_{S,e}^{2/3} / l_s$

Table 1.2: Analytical dispersion relations in the drift kinetic limit  $\tau = 0$  without equilibrium gradients.

is presented which must be solved for  $\omega$  [54]. The algebraic equation contains the poloidal plasma beta  $\beta_p$  at  $a$ , the diamagnetic frequency  $\omega^*$  and a complex function  $R(\omega_0)$  depending on  $\omega_0 \approx \omega^* (1 + \eta_e/2)$ <sup>1</sup>. The linear electron current layer width is given by  $\delta_e^* = \omega^* l_s / (k_y v_e)$ . In the case  $\Delta' d_e > 1$  and vanishing equilibrium gradients as well as  $\tau \rightarrow 0$ , the corresponding result of Table (1.2) can be restored<sup>2</sup>.

### 1.4.3 The nonlinear tearing mode

The island formation of resistive and collisionless tearing modes is well known, but differs clearly in both cases.

The magnetic islands in the resistive case do not saturate after the linear phase, rather the island width in the low- $\Delta'$  regime grows algebraically in time [17]. In the collisionless case the tearing mode stabilises nonlinearly in the small- $\Delta'$  range. The magnetic island width oscillates with a characteristic frequency for all times later than the initial nonlinear phase. If  $\Psi$  does not vary too much over the tearing

<sup>1</sup> The diamagnetic frequency of the electrons is given by  $\omega^* = k_y k_B T_e / (q_e B_{0,z}) (dn_{0,e}/dx) / n_{0,e}$  in SI units and  $\omega^* = k_y (dn_{0,e}/dx) / n_{0,e}$  in EUTERPE units.

<sup>2</sup> Reference [44] generalises the dispersion relation  $\gamma(k_y)$  to the case with diamagnetic effects. However, the term for  $\gamma_0(k_y)$  in this reference is not consistent with Refs. [10, 38]. In this thesis the term  $\gamma_0(k_y)$  of Ref. [38] is adopted.

$L_{T,n} \approx 1, \tau \approx 1$	$\gamma$	$\hat{\omega}$
$\Delta' d_e < 1$ , [54]	$\frac{1+\eta_e/2+1/\tau}{1+1/\tau} \frac{\gamma}{1+\eta_e/2} (\omega^*/\omega) = (\omega^*/\omega) \frac{\Delta' a \delta_e^*}{a \beta_p} + (1 + 1/\tau) R(\omega_0)$	
$\Delta' d_e > 1$ , [44]	$\gamma^2 = \gamma_0^2 - \left[ \frac{k_y \kappa_{T,e}}{2\eta} (1 + \tau) \right]^2$ $\gamma_0 = k_y / l_s (2d_e \rho_{S,e}^2 (1 + \tau) / \pi)^{1/3}$	$\hat{\omega} = \frac{k_y \kappa_{T,e}}{2\eta} (1 - \tau)$

Table 1.3: Analytical dispersion relations, valid only for  $\rho_{S,e} > d_e$ , including finite ion temperature and diamagnetic effects.

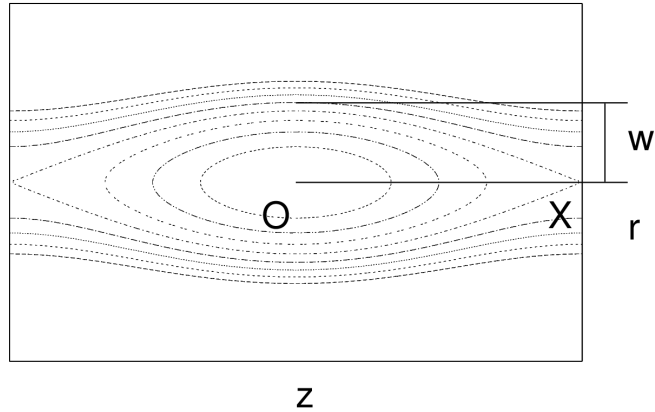


Figure 1.6: Qualitative structure of a magnetic island. The  $X$ -point is located at  $z = 2\pi/k_y$ ,  $r = 0$  and the  $O$ -point at  $z = \pi/k_y$ ,  $r = 0$ . The half width  $w$  is the half of the maximum extension of the separatrix regarding  $r$ .

layer, the constant- $\Psi$  (constant- $A$ ) approximation can be applied. Let  $\bar{A}(t)$  be the value of the perturbed vector potential across the layer at the  $O$ -point and assuming  $B_{0,y}(x) \sim x$ , the field lines close to the resonant surface can be represented by

$$F(r, z) = \frac{r^2}{2l_s} + \bar{A}(t) \cdot \cos(k_y z) = \text{const.} \quad (1.24)$$

The contour lines of  $F(r, z)$  are sketched in Figure 1.6. During island formation the open field lines move to the  $X$ -point, tear and reconnect. The newly reconnected field lines are accelerated towards the  $O$ -point. As shown in this Figure, the set of open and closed magnetic field lines is divided by the magnetic separatrix. The half of the maximum elongation with respect to  $r$  defines the island half width  $w(t)$ . In the constant- $\Psi$  approximation the island width is given by [13]

$$w(t) = 2\sqrt{\bar{A}(t)l_s}. \quad (1.25)$$

In this approximation the island half width is obtained by measuring the vector potential over time at the  $O$ -point.

The magnetic island grows and alters the magnetic confinement properties of the plasma. If the amplitude of the mode is sufficient large the charged species become trapped in this newly formed island structure. When the width of the magnetic islands reaches the width of the perturbed linear current channel  $\delta_e$ , the plasma inflow towards the layer is strongly reduced and the mode saturates [18].

The nonlinear evolution of tearing modes in the high- $\Delta'$  limit differs completely from their evolution in the opposite limit. The mode shows “explosive” reconnection indicated by an accelerated growth when entering the nonlinear phase [23] and the island width can reach macroscopic level of order  $w(t) = \mathcal{O}(a, L_x)$ .

## 2 Gyrokinetics

### 2.1 Gyrokinetic description

In this chapter a comprehensive description of gyrokinetics will be given to get in touch with this formalism, followed by the formal description of the theory in the next chapter.

The collisionless kinetic approach studying plasma physics consists of using the Vlasov equation for each species  $s$  [58]

$$\frac{dF_s}{dt} = \frac{\partial F_s}{\partial t} + \vec{v} \cdot \frac{\partial F_s}{\partial \vec{r}} + \frac{q_s}{m_s} \left( \vec{E} + \vec{v} \times \vec{B} \right) \cdot \frac{\partial F_s}{\partial \vec{v}} = 0. \quad (2.1)$$

The one-particle phase space distribution functions  $F_s(\vec{r}, \vec{v})$  are defined on the six-dimensional phase space.

Maxwell's equations describing the electromagnetic fields  $\vec{E}$  and  $\vec{B}$ , together with the sources  $\rho$  and  $\vec{j}$  obtained from  $F_s$ , close this system of equations.

The applicability of Eq. (2.1) is limited because it rests on the assumption that pair correlations between the particles can be neglected. Therefore, the Vlasov equation is valid as long as a typical correlation or collisional time scale  $t_C$ , is much larger than the characteristic time scale of the correlation-free system,  $t \ll t_C$ . This situation can be found in the hot core region of fusion plasmas since the collisional time scale increases with the temperature  $T$  roughly as  $t_C \sim T^{3/2}$ . The collisionless approach is also valid in astrophysics when the mean free path of the species is much larger than the characteristic spatial scales of the mode of interest. If the correlation-free description fails, the collisional kinetic approach known as Boltzmann equation would apply.

It is a computationally expensive task to solve Eq. (2.1). Conventional fusion devices are characterised by a strong magnetic guiding field along a specific direction and relatively weak magnetic fields perpendicular to it. Therefore, the physics becomes strongly anisotropic and the theoretical models are designed to account for this property, accompanied by a simplification of the resulting equations.

In a strongly magnetised plasma each charged particle performs a gyromotion around the guiding field shown in Figure 2.1 (left). The gyration can be described by

$$\begin{aligned} \vec{r} &= \vec{R} + \vec{\rho}_s \\ \vec{\rho}_s &= \frac{v_\perp}{\Omega_s} (\cos \alpha \hat{e}_1 + \sin \alpha \hat{e}_2). \end{aligned}$$

## 2 Gyrokinetics



Figure 2.1: Left: Microscopic dynamics of gyrating species (red) around a magnetic field line (blue). Right: Averaging over the fast gyromotion to pass to gyrokinetics. The gyrocenter is described by its position  $\vec{R}$ , the parallel canonical momentum  $p_{\parallel}$  along the magnetic field line and  $\mu_B$  (giving  $\rho$ ).

$\vec{R}$  is the gyrocenter position,  $\rho_s$  the gyroradius,  $\alpha$  the gyrophase and  $v_{\perp}$  the perpendicular velocity.

The applicability of the gyrokinetic model assumes that the gyrofrequency  $\Omega_s$  is the smallest timescale in the system. All other processes with a typical frequency  $\omega$  evolve on a much longer timescale.

Thus the first step in introducing gyrokinetics consists of removing the fast frequencies  $\Omega_s$  from the system with an appropriate formalism without losing essential information about larger timescales. In a sense, one averages over the fast gyromotion of the kinetic equation (2.1) to get the gyrokinetic equation [59, 60]

$$\frac{df_s}{dt} = \frac{\partial f_s}{\partial t} + \dot{\vec{R}} \cdot \nabla f_s + \dot{p}_{\parallel} \cdot \frac{\partial f_s}{\partial p_{\parallel}} = 0. \quad (2.2)$$

It describes the evolution of a five-dimensional phase space distribution function  $f_s(\vec{R}, p_{\parallel}, \mu_B)$  of the gyrocenters. The physical particle is replaced by a quasi-particle that consists of a charged ring and carries a conserved magnetic moment  $\mu_B$  by definition, i. e.  $d\mu_B/dt \doteq 0$ . The new microscopic description of the particles is shown in Figure 2.1. In contrast to the description of the full gyration of the particles (left), the quasi-particle is just guided along the magnetic field (right). In general the gyrating particles experience also  $\nabla B$ -, curvature- and  $\vec{E} \times \vec{B}$ -drifts caused by the electromagnetic equilibrium background fields. For the sake of simplification they are not discussed here, but are of course included in the gyrokinetic theory as well.

Additionally, in the gyrokinetic approach one assumes that the variations of the equilibrium quantities varies on scales  $L$ , which are much larger than the gyroradius. However, it is still possible that the spatial scales of the perturbation  $k_{\perp}^{-1}$  can be of the order of the Larmor radius. This situation is displayed in Figure 2.2, left. In case of two species  $s = (i, e)$ , typically only for the ions an explicit gyrokinetic description is necessary due to the large natural mass ratio  $\mu$  the electron Larmor radius  $\rho_e$  can be neglected.

If the essential spatial scales related to magnetic reconnection, i. e.  $L$ ,  $k_{\perp}$ ,  $d_e$  and  $\rho_i$ , are much larger than the Debye length, the plasma appears quasi-neutral. Charge separation can be neglected and thus the condition of quasi-neutrality holds, i. e.

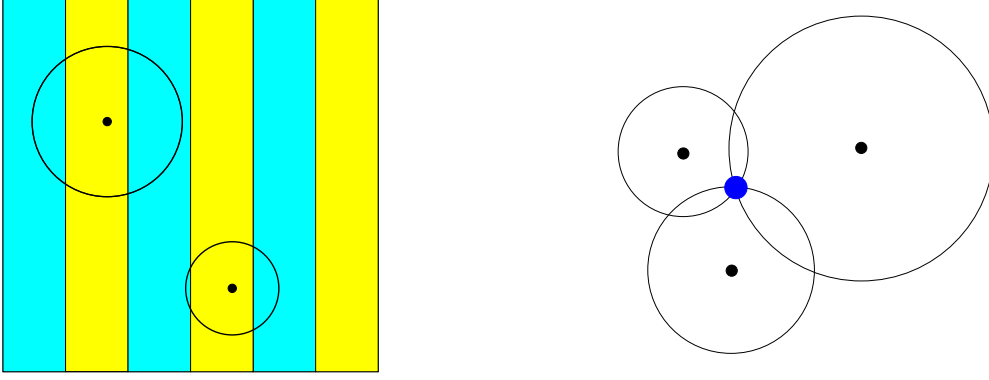


Figure 2.2: Left: The gyrokinetic model allows for small scale perturbations that are of the order of the gyroradius. Right: schematic explanation of the gyroaveraged density  $\langle n_s \rangle$ . At location  $\vec{x}$  (blue point) one wishes to compute the density  $n_s(\vec{x})$  to which all gyro-particles (black rings) contribute, whose gyrorings pass through  $\vec{x}$ .

equating the number densities of the physical particles,  $n_e(\vec{x}) = n_i(\vec{x})$ . This expression serves as an additional field equation, since the densities are obtained by integrals of the distribution functions over the phase space which depend on the fluctuating electromagnetic fields.

In the gyrokinetic framework one has to express the number densities  $n_s(\vec{x})$  of the physical particles in terms of the density of gyrocenters  $n_s(\vec{R})$ . To get the physical density one first defines the gyroaveraged density  $\langle n_s \rangle(\vec{x})$  according to <sup>1</sup>

$$\langle n_s \rangle(\vec{x}) = \int B^* d\vec{R} dp_{\parallel} d\mu_B d\alpha \delta(\vec{R} + \vec{\rho}_s(\vec{R}) - \vec{x}) \delta f_s(\vec{R}, p_{\parallel}, \mu_B). \quad (2.3)$$

This expression relates the gyrocenter position  $\vec{R}$  with the variable  $\vec{x}$ , where to evaluate the gyroaveraged density. In Figure 2.2 (right) the schematic evaluation of the gyroaveraged density  $\langle n_s \rangle$  at  $\vec{x}$  (blue point) is sketched for three quasi-particles. The expression (2.3) forces only those quasi-particles (black circles) to contribute to  $\langle n_s \rangle(\vec{x})$  that have any point on their gyroring in common with  $\vec{x}$ . In the derivation of the gyrokinetic quasi-neutrality condition an additional polarisation density  $n_{pol,s}(\vec{x})$  which depends on the electrostatic field corrects the gyroaveraged density to give finally the physical number density  $n_s(\vec{x}) = \langle n_s \rangle(\vec{x}) + n_{pol,s}(\vec{x})$ .

The second field equation is provided by parallel Ampère's law which describes the perpendicular magnetic fluctuations  $\delta B_{\perp}$ . Eq. (2.2) and both quasi-neutrality and parallel Ampère's law form the *standard* electromagnetic gyrokinetic model [59].

It is customary to treat only the perpendicular magnetic fluctuations in a low- $\beta$  plasma, defined by the condition  $\beta \ll 1$  [61]. If  $\beta$  is allowed to reach values of order unity,  $\beta = \mathcal{O}(1)$ , the parallel magnetic field fluctuations  $\delta B_{\parallel}$  become as important as the perpendicular magnetic perturbations. Consequently, the perpendicular Ampère's law must be introduced.

<sup>1</sup>The quantity  $B^*$  will be defined in Sec. (2.2).

## 2.2 Electromagnetic gyrokinetic equations in a slab

The standard gyrokinetic equations result from an ordering procedure [60] with respect to the ratios  $\rho_i/L$ ,  $k_{\parallel}/k_{\perp}$  and  $\omega/\Omega_s$  much smaller than unity. Nevertheless, this ordering allows the perturbation to be comparable to the Larmor radius,  $k_{\perp} \rho_i = \mathcal{O}(1)$ . The gyrokinetic equation

$$\frac{df_s}{dt} = \frac{\partial f_s}{\partial t} + \dot{\vec{R}} \cdot \nabla f_s + \dot{p}_{\parallel} \cdot \frac{\partial f_s}{\partial p_{\parallel}} = 0, \quad (2.4)$$

describes the evolution of the distribution functions of the gyrocenters in phase space. This equation will be solved by EUTERPE using the method of characteristics. The characteristics of Eq. (2.4) in a slab read in terms of the variable  $p_{\parallel}/m_s = v_{\parallel} + q_s A/m_s$ <sup>1 2</sup> [59]

$$\begin{aligned} \dot{\vec{R}}_s &= \frac{p_{\parallel}}{m_s} \vec{b} - \frac{q_s}{m_s} \vec{b} \langle A \rangle + \frac{1}{B^*} \vec{b} \times \nabla \langle \phi - \frac{p_{\parallel}}{m_s} A \rangle \\ &= \frac{p_{\parallel}}{m_s} \vec{b} + \dot{\vec{R}}^1, \\ \frac{\dot{p}_{\parallel}}{m_s} &= -\frac{q_s}{m_s} \vec{b} \cdot \nabla \langle \phi - \frac{p_{\parallel}}{m_s} A \rangle, \\ \dot{\mu}_B &= 0. \end{aligned} \quad (2.5)$$

The averaging procedure of the field fluctuations,

$$\langle A, \phi \rangle(\vec{R}) = \frac{1}{2\pi} \int_0^{2\pi} d\alpha (A, \phi)(\vec{x}, t)|_{\vec{x}=\vec{R}+\vec{\rho}_s(\alpha)} \quad (2.6)$$

introduces a mean field at  $\vec{R}$ , where the quasi-particle is affected by the forces. When performing PIC simulations it is advantageous to split the full phase space distribution function  $f_s$  using the  $\delta f$ -ansatz [26, 62]

$$f_s = f_{0,s} \left( \vec{R}, \frac{p_{\parallel}}{m_s}, \mu_B \right) + \delta f_s \left( \vec{R}, \frac{p_{\parallel}}{m_s}, \mu_B, t \right). \quad (2.7)$$

The time-independent background Maxwellian is assumed to be given analytically,

$$f_{0,s} = \frac{n_{0,s}(\vec{x})}{\sqrt{2\pi} v_s(x)^2} e^{-\frac{\left(\frac{p_{\parallel}}{m_s} - u_{0,s}(x)\right)^2 + v_{\perp}^2}{2v_s(x)^2}}. \quad (2.8)$$

The  $\delta f$ -ansatz reduces the particle-induced noise. The bulk velocity  $u_{0,s}$  allows for a parallel equilibrium current which depends only on the spatial slab coordinate  $x$ .

<sup>1</sup>If not stated otherwise the equations are always normalised to the unit system used in EUTERPE. The normalisation procedure is explained in Sec. (4.1).

<sup>2</sup>The Eqs. contain the quantity  $B^* = B + m_s/q_s (p_{\parallel}/m_s) \vec{b} \cdot (\vec{\nabla} \times \vec{b})$ . For the outlines discussed here it is customary to use the approximation  $B^* \approx B$  [26].

Inserting Eq. (2.7) into Eq. (2.2) gives

$$\begin{aligned} \frac{d\delta f_s}{dt} &= -\frac{df_{0,s}}{dt} = -f_{0,s}S_s, \\ S_s &= \kappa_s \dot{\vec{R}}^1 \cdot \nabla x + \frac{q_s}{m_s v_s(x)^2} \left[ -\left(\frac{p_{\parallel}}{m_s} - u_{0,s}\right) \vec{b} \cdot \nabla \left\langle \phi - \frac{p_{\parallel}}{m_s} A \right\rangle \right]. \end{aligned} \quad (2.9)$$

Furthermore, one defines

$$\begin{aligned} \kappa_s &= \kappa_{n,s} - \kappa_{T,s} \left( \frac{3}{2} - \frac{\left(\frac{p_{\parallel}}{m_s} - u_{0,s}(x)\right)^2 + v_{\perp}^2}{2v_s(x)^2} \right) - \kappa_{u_{0,s}}, \\ \kappa_{u_{0,s}} &= \frac{\left(\frac{p_{\parallel}}{m_s} - u_{0,s}(x)\right)}{v_s(x)^2} \frac{du_{0,s}}{dx}, \\ \kappa_{T,s} &= -\frac{1}{T_{0,s}} \frac{dT_{0,s}}{dx}, \\ \kappa_{n,s} &= -\frac{1}{n_{0,s}} \frac{dn_{0,s}}{dx}. \end{aligned} \quad (2.10)$$

The quasi-neutrality condition demands for the physical charge densities

$$\sum_s q_s n_s(\vec{x}) = 0, \quad (2.11)$$

for drift kinetic electrons, and gyrokinetic ions [59, 62]

$$n_i(\vec{x}) = \langle n_i \rangle(\vec{x}) + \frac{\Gamma_0 - 1}{\rho_i^2} \phi(\vec{x}). \quad (2.12)$$

The first term on the right hand side of Eq. (2.12) has been defined in Eq. (2.3), while the second term represents the polarisation density  $n_{pol,s}(\vec{x})$ .

The exact expression for  $\Gamma_0$  in Eq. (2.12) is a complicated nonlocal operator in real space and difficult to treat numerically. It is usually formulated in Fourier space where it reads  $\Gamma_0(k_{\perp}^2 \rho_i^2)$ , defined in terms of the modified Bessel function  $I_0(x)$  of the first kind according to  $\Gamma_0(x) = e^{-x} I_0(x)$  [62].

The simplest approximation of the polarisation density in the ion response consists of using the long wavelength approximation,  $k_{\perp} \rho_i \ll 1$ . Expanding  $\Gamma_0$  in a Taylor series in this limit the ion density response becomes  $\Gamma_0 \approx 1 + k_{\perp}^2 \rho_i^2$  which in real space reads

$$n_i(\vec{x}) = \langle n_i \rangle(\vec{x}) + \nabla_{\perp}^2 \phi(\vec{x}). \quad (2.13)$$

Only in the range of small gyroradii,  $k_{\perp} \rho_i < 0.5$ , the long wavelength approximation is useful to describe finite Larmor radius effects correctly [63].

A further common approximation of the polarisation density is provided by the

## 2 Gyrokinetics

Padé approximation [62]. The advantage of the Padé approximation is that it gives reasonable results for arbitrary values of  $k_{\perp}^2 \rho_i^2$  compared with the exact gyroaveraged result and can be calculated easily. The Padé approximation replaces  $\Gamma_0$  in Fourier space by  $\Gamma_0(k_{\perp}^2 \rho_i^2) \mapsto 1/(1 - k_{\perp}^2 \rho_i^2)$ . One can show that the resulting density of the ions in real space is given by

$$n_i(\vec{x}) = \langle n_i \rangle(\vec{x}) + \nabla_{\perp}^2 \phi(\vec{x}) + \nabla \rho_i^2 \nabla_{\perp} [\langle n_i \rangle(\vec{x}) - n_e(\vec{x})]. \quad (2.14)$$

Therefore, the field equation for  $\phi$  is given by  $n_e(\vec{x}) = n_i(\vec{x})$  with either the ion response according to Eq. (2.13) or Eq. (2.14).

The Vlasov-Maxwell system is closed by Ampère's law. The physical parallel currents  $j_{ph,\parallel,s}$  are the sources for the parallel vector potential  $A$  according to

$$-\frac{1}{\beta} \nabla_{\perp}^2 A(\vec{x}) = \sum_s \langle j_{ph,\parallel,s} \rangle(\vec{x}). \quad (2.15)$$

However, the current response in the  $p_{\parallel}$ -description as it is used here, is derived from the first moment of the perturbed distribution function with respect to the momentum canonical  $p_{\parallel}/m_s$ . In this formalism Ampère's law reads

$$-\frac{1}{\beta} \nabla_{\perp}^2 A(\vec{x}) + \sum_s n_{0,s}(\vec{x}) \frac{q_s^2}{m_s} A(\vec{x}) = \sum_s \langle j_{\parallel,s} \rangle(\vec{x}). \quad (2.16)$$

The so-called skin terms proportional to the field amplitude appear on the left hand side. Formally, the skin term cancels completely the adiabatic response of the right hand side of Eq. (2.16) which would result again in Eq. (2.15) [62].

The gyrooperation for the current in Eq. (2.16) is defined equivalently to Eq. (2.3),

$$\langle j_{\parallel,s} \rangle(\vec{x}) = \int B^* d\vec{R} d\vec{v} d\alpha \delta(\vec{R} + \vec{\rho}_s(\vec{R}) - \vec{x}) \delta f_s \frac{p_{\parallel}}{m_s}. \quad (2.17)$$

In the *standard* gyrokinetic equations shear Alfvén waves are admissible solutions while compressional Alfvén waves do not appear, since the perpendicular Ampère's law is not taken into account.

In the description of tearing modes an usual ordering of the reconnection relevant scales is imposed originating from experimental observations. The electron skin depth  $d_e$  and the perpendicular scale of the perturbation  $k_{\perp}^{-1}$  is assumed to be much smaller than the gyroradius,  $k_{\perp}^{-1} \approx d_e \ll \rho_i$ . The gyroradius, which is approximately the Larmor sound radius  $\rho_{S,e}$  for  $\tau = \mathcal{O}(1)$ , is smaller than the variation of all equilibrium gradients, either magnetic field or density and temperature variation,  $\rho_i \approx \rho_{S,e} \ll L_{\text{eq},x}$ .

The observed growth rate of the tearing mode in experimental devices is typically much smaller than the gyrofrequency of the ions and electrons,  $\gamma \ll \Omega_s$ . Therefore, the assumptions of the standard gyrokinetic equations are fulfilled.

# 3 The PIC method

## 3.1 Implementation of the PIC method

The kinetic simulations were performed with the PIC code EUTEPRE. It solves the Vlasov-Maxwell system in global and toroidal three-dimensional geometry using the method of characteristics. The PIC code shows a good parallel scaling with a large number of processors. The magnetic background equilibrium is provided by a VMEC file, from which all relevant magnetic equilibrium quantities are derived.

This numerical method contains principally the same computational cycle as every particle-in-cell method [64]. EUTEPRE uses the  $\delta f$ -approach to reduce particle noise in contrast to a full- $f$  method. The perturbed part of the distribution function is discretised by using numerical particles, called markers. The statistics induced by the marker representation improves with increasing number of markers  $N_p$  as  $1/\sqrt{N_p}$  [63].

The temporal integration of the characteristics of the gyrokinetic equation and weight evolution is performed by a Runge-Kutta scheme of fourth order. A recently implemented Fehlberg integrator allows also the use of an adaptive time step method [70]. The particle trajectories are pushed in a cylindrical coordinate system,  $\vec{x} = (r, z, \bar{\phi})$ .

The charge and the current densities as the sources of the field equations are provided by a corresponding Monte-Carlo integration over the phase space using markers. The field equations are discretised in real space by a  $B$ -spline finite element method [68] and solved by sparse matrix tools [65]. The solver works in a straight field line coordinate system,  $\vec{\xi} = (\bar{s}, \chi, \bar{\phi})$  [66]. Both coordinate systems can be converted into each other using the VMEC file <sup>1</sup>.

To further reduce the statistical noise induced by the markers, it is possible to use a Fourier filter to extract a specific poloidal mode number  $m$  and a toroidal mode number  $n$  of the fields. Furthermore, it is possible to filter the field in a limited rectangular domain in Fourier space  $(-m_{\max}, \dots, m_{\max}) \times (-n_{\max}, \dots, n_{\max})$ , if  $m_{\max}$  and  $n_{\max}$  are the maximum poloidal and toroidal mode numbers.

### 3.1.1 Discretisation of the distribution function

In EUTEPRE the perturbed distribution function  $\delta f_s$  is sampled by  $N_p$  markers with the coordinates  $\vec{R}_n$ ,  $p_{\parallel,n}/m_s$  and  $\mu_{B,n}$  in the reduced phase space. Each marker carries a weight  $w_n(t)$  that is traced along the characteristics of the gyrokinetic

---

<sup>1</sup>The coordinate transformation between both systems is explained in Sec. (4.3)

### 3 The PIC method

equation. The perturbed distribution function is assumed to have the form [68]

$$\delta f_s = \sum_{n=1}^{N_p} \frac{w_n(t)}{B^*} \cdot \delta(\vec{R} - \vec{R}_n) \delta\left(\frac{p_{\parallel}}{m_s} - \frac{p_{\parallel,n}}{m_s}\right) \delta(\mu_B - \mu_{B,n}). \quad (3.1)$$

Around each marker position  $\vec{z}_n = (\vec{R}_n, p_{\parallel,n}/m_s, \mu_{B,n})$  a small phase space volume  $\Omega_{n,s}$  is located representing the phase space volume carried by the marker at this position. The values of  $\Omega_{n,s}$  are predefined with the only constraint that the sum of all small phase space volumes has to fill out the phase space completely without overlap or holes.

The markers are distributed in phase space using a numerical probability function  $g(\vec{z})$  that is constant along the marker trajectory ( $dg/dt = 0$ ). It is assumed here that  $g$  can be split into a pure spatial part  $g_R$  and a part  $g_v$  that describes the distribution in momentum space, thus  $g = g_R \cdot g_v$ . The pure spatial part  $g_R$  can be set constant over the real volume  $V$ ,  $g_R = 1/V$ . A uniform marker loading in momentum space as it is employed here is defined by setting  $g_v dv_{\parallel} d\mu_B d\alpha = \text{const.}$  One can show from the condition  $\int d\vec{z} g = 1$  that in this case  $g = 1/(V \cdot (\pi \kappa_{v,s} v_s)^2 v_{\perp})$ , being  $\kappa_{v,s}$  the radius of the momentum sphere in terms of  $v_s$ .

The source terms of the field equations are provided by phase space integrals of the perturbed distribution function. From the numerical point of view the high-dimensional phase space integrals can be carried out efficiently using a Monte-Carlo integration. This approach replaces the integration by an evaluation of an expectation value  $E$ , using the numerical distribution function  $g(\vec{z})$ . The expectation value is then approximated by the usual estimator for an arbitrary function  $h(\vec{z})$

$$\begin{aligned} E[h] &= \int d^6 Z h(\vec{z}, t) \cdot \delta f(\vec{z}, t) \\ &= \int d^6 Z h(\vec{z}, t) \cdot \frac{\delta f(\vec{z}, t)}{g(\vec{z})} \cdot g(\vec{z}) \\ &= \frac{1}{N_p} \sum_{n=1}^{N_p} h(\vec{z}_n, t) w_n(t) + \epsilon_{\text{stat}}. \end{aligned} \quad (3.2)$$

The weights are defined by  $w(\vec{z}_n, t) = \delta f(\vec{z}_n, t) / g(\vec{z}_n) \doteq \Omega_n \delta f(\vec{z}_n, t)$ . The statistical error  $\epsilon_{\text{stat}}$  reduces with increasing marker number,  $\epsilon_{\text{stat}} \sim 1/\sqrt{N_p}$ .

The temporal evolution of the weight follows from inserting Eq. (3.1) into Eq. (2.2) and integrating over  $\Omega_{n,s}$ ,

$$\frac{dw_{n,s}}{dt} = -\Omega_{n,s} f_{0,s} S_s. \quad (3.3)$$

The term  $S_s$  is given by Eq. (2.9) (Sec. 2.2). According to Eq. (3.2) the source terms of the field equations can be computed by selecting  $h = 1$  or  $h = p_{\parallel}/m_s$  for density or current, respectively.

### 3.1.2 Discretisation of the field equations

The field equations for the electrostatic potential  $\phi$  and the parallel vector potential  $A$ , Eqs. (2.12, 2.16) are discretised with a finite element method using the representation

$$\phi(\vec{\xi}) = \sum_l \phi_l \Lambda_l(\vec{\xi}), \quad A(\vec{\xi}) = \sum_l A_l \Lambda_l(\vec{\xi}). \quad (3.4)$$

$\Lambda_l(\vec{\xi})$  represents a  $B$ -spline finite element with multi-index  $l = (i_1, i_2, i_3)$ . It is assumed to factorise according to  $\Lambda(\vec{\xi})_l = \Lambda_{i_1}(\bar{s}) \Lambda_{i_2}(\chi) \Lambda_{i_3}(\bar{\phi})$ . In this thesis each  $B$ -spline was chosen to be of order two. This corresponds to quadratic splines, whose spatial derivatives and so the forces on the particles still depend continuously differentiable on the coordinates  $\vec{\xi}$ .

The quasi-neutrality equation in the long wavelength approximation and Amperère's law can be projected into the  $B$ -spline basis, Eq. (3.4) [62]

$$- \int d\vec{\xi} \Lambda_k(\vec{\xi}) \nabla_{\perp}^2 \phi = \int d\vec{\xi} \Lambda_k(\vec{\xi}) (\langle n_i \rangle(\vec{\xi}) - n_e) \quad (3.5)$$

$$\int d\vec{\xi} \Lambda_k(\vec{\xi}) \left( \sum_s \frac{\beta_s}{\rho_s^2} A - \nabla_{\perp}^2 A \right) = \int d\vec{\xi} \Lambda_k(\vec{\xi}) \langle j_{\parallel, s} \rangle(\vec{\xi}). \quad (3.6)$$

Using Eq. (3.4) and performing an integration by parts one obtains the set of linear equations

$$\sum_l M_{kl}^{(Q)} \phi_l = N_k^{(Q)}, \quad \sum_l M_{kl}^{(A)} A_l = N_k^{(A)}. \quad (3.7)$$

The elements of the matrices  $M_{kl}^{(Q)}$  and  $M_{kl}^{(A)}$  are calculated and stored at the beginning of every simulation. Eqs. (3.7) are solved during every computational cycle by parallel preconditioned iterative methods using of the tools the PETSc library [65].

### 3.1.3 Requirements in electromagnetic simulations

In EUTERPE the gyrokinetic equation is discretised within the  $p_{\parallel}$ -formalism originating from the historical development of PIC methods. Early attempts failed in discretising the electromagnetic slab equations using the  $v_{\parallel}$ -formalism due to the partial time derivative of the vector potential [67].

Although the  $p_{\parallel}$ -approach is successful for the description of many electromagnetic instabilities, simulations of e. g. damped modes are more sophisticated due to the so-called cancellation problem, magnified for high- $\beta$  scenarios ("high- $\beta$  problem") or, for instance, MHD modes with medium  $\beta$ -values ( $\beta = \mathcal{O}(1\%)$ ) in the limit  $k_{\perp} \rightarrow 0$ . It is caused by the different discretisation of the left hand side of Ampère's law, Eq. (3.6) and the "current" density on the right hand side. The left hand side is discretised by  $B$ -splines, whereas the current density is represented by particles. From the mathematical point of view the skin term perfectly cancels the adiabatic part of the current. These two different kinds of discretisations do not necessarily lead

### 3 The PIC method

to a numerical cancellation.

In this thesis an enhanced control variates method has been used for simulations with EUTERPE to safely perform electromagnetic calculations. This algorithm rests upon an iterative method which gradually removes the adiabatic part of the current response within each computational cycle [62, 68]. The scheme has been proven to achieve simulations of Alfvén modes in a slab to very high accuracy [62, 69].

During this work it has been observed that the tearing mode is rather robust with respect to the cancellation of the adiabatic current response. Simulations of the tearing mode in a slab can be performed with a sufficient high number of particles without using the iterative procedure. For the benchmark of the Alfvén wave the iteration scheme was applied, but it was not used in general.

## 3.2 Diagnostic tools

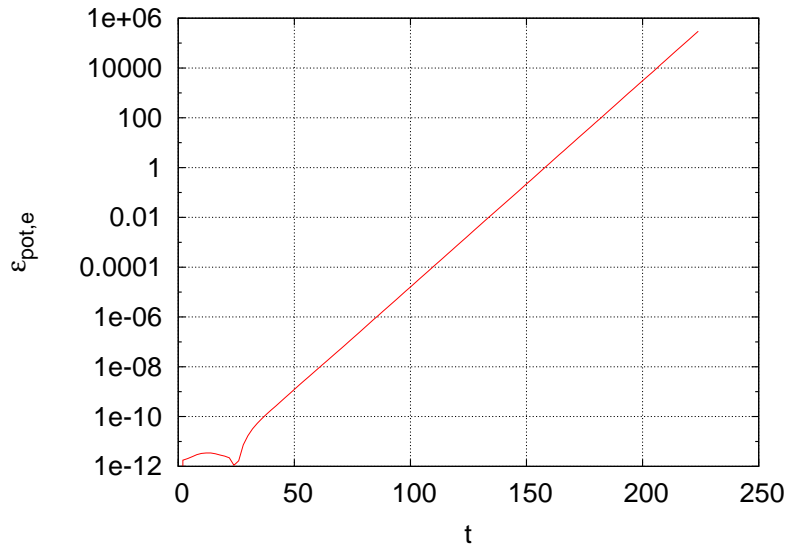


Figure 3.1: Temporal evolution of the perturbed field energy. The slope is proportional to the growth rate  $\gamma$ .

EUTERPE provides a lot of tools to extract information about the simulations both in time and space. The energy of the system over the volume  $V$  of the simulation domain is given by the sum of kinetic energy  $E_{\text{kin},s}$  and field energy  $E_{\text{field},s}$  over  $V$  according to  $E(t)/V = 1/V \sum_s [E_{\text{kin},s}(t) + E_{\text{pot},s}(t)] = \text{const}$ . The corresponding contributions are defined by

$$\begin{aligned}
 E_{\text{pot},s}/V &= \frac{1}{2V} \int_V d\vec{\xi} (q_s \langle n_s \rangle \phi - \langle j_s \rangle A_{\parallel}), \\
 E_{\text{kin},s}/V &= \frac{1}{V} \int_{\Omega_{\text{PS}}} d^6 Z \frac{m_s}{2} (v_{\perp}^2 + v_{\parallel}^2) (f_{0,s} + \delta f_s(t)).
 \end{aligned}
 \tag{3.8}$$

In the last term the part related to  $f_{0,s}$  describes the initial kinetic energy  $E_{\text{kin},0,s}$  while the contribution of  $\delta f_s$  describes the perturbed part of the kinetic energy,  $\epsilon_{\text{kin},e}$ . For the simulations presented in this work the electrons mainly influence the dynamics of reconnection, thus the field energy of the electrons  $\epsilon_{\text{pot},e}(t)$  is used to obtain first quantitative statements for instance measuring the growth rate of the excited modes.

Figure 3.1 shows the evolution of the electron field energy  $\epsilon_{\text{pot},e}(t)$  of a tearing mode. After the initial transient phase,  $t \lesssim 50$ , the exponential behaviour dominates. In this phase the growth rate can be computed by the rescaled temporal derivative of the field energy according to  $(d\epsilon_{\text{pot},e}/dt)/\epsilon_{\text{pot},e} = 2\gamma$ .

When investigating nonlinear tearing modes the quality of the simulations is indicated by the conservation of energy. The quantity  $\Delta\epsilon$  is introduced for electrons and defined by  $\Delta\epsilon = |(E_{\text{kin},0,e} + \epsilon_{\text{kin},e} + \epsilon_{\text{pot},e})/E_{\text{kin},0,e} - 1|$ . An order of  $\Delta\epsilon = \mathcal{O}(1\%)$  reflects a reasonable conservation of energy during the simulations.

A further important diagnostics is the spatio-temporal field structure that can be extracted directly from EUTERPE. From these data important values like, for instance, the island half width can be obtained by evaluating the mode structure.



# 4 Electromagnetic simulations in a slab

## 4.1 Normalisation procedures

The equations and relations used in EUTERPE are normalised to a proper unit system according to

$$t = \Omega_i \hat{t}, \quad x = \frac{\hat{x}}{\rho_{S,e}}, \quad A = \frac{\hat{A}}{B_{0,z} \rho_{S,e}}, \quad \phi = \frac{\hat{\phi}}{B_{0,z} \rho_{S,e}^2 \Omega_i}, \quad (4.1)$$

where carets denote dimensional quantities. The density  $\hat{n}_s$  and temperature  $\hat{T}_s$  is normalised to the constant background density  $n_0$  and the flat temperature profile of the electrons  $T_e$ , respectively. If not stated otherwise this will be the standard normalisation for all relations presented in this work.

In chapter 7.1 a fluid model is compared with the gyrokinetic model implemented in EUTERPE. This fluid model adopts Alfvén units

$$t = \frac{\hat{t}}{t_A}, \quad x = \frac{\hat{x}}{L_{\text{eq,B}}}, \quad A = \frac{\hat{A}}{B_{0,z} L_{\text{eq,B}}}, \quad \phi = \frac{\hat{\phi}}{B_{0,z} L_{\text{eq,B}} v_A}. \quad (4.2)$$

The gyrofluid model describes the evolution of the gyrocenter densities  $\hat{n}_s$  and current fields  $\hat{u}_s$ <sup>1</sup> that are normalised according to

$$n_s = \frac{L_{\text{eq,B}} \hat{n}_s}{\hat{d}_i n_0}, \quad u_s = \frac{L_{\text{eq,B}} \hat{u}_s}{\hat{d}_i v_A}. \quad (4.3)$$

## 4.2 MHD slab equilibria for reconnection simulations

In this thesis two kinds of ideal MHD equilibria are used for simulations which is motivated by different equilibria presently used in literature.

For both equilibria a strong guiding field in the toroidal direction  $\hat{z}$  of strength  $B_{0,z}$

---

<sup>1</sup> Although this notation is misleading, it is customary in literature to write  $u_s$  for the current field [10].

is present. The first equilibrium (magnetic configuration I) is given by

$$B_{0,y}(x) = -\frac{\beta}{2} C \sqrt{\mu \pi} a \operatorname{erf}\left(\frac{x - \frac{L_x}{2}}{a}\right). \quad (4.4)$$

The error function  $\operatorname{erf}(x)$  varies significantly over a distance  $a = L_{\text{eq,B}}$ . The strength of the perpendicular magnetic field is controlled by the dimensionless parameter  $C > 0$ . The direction of guiding and perpendicular magnetic field is shown in Figure 4.1. This equilibrium forces the resonant surface to be at  $x = L_x/2$  in two-dimensional simulations.

The equilibrium configuration II is frequently used in fluid simulations [44, 51] and

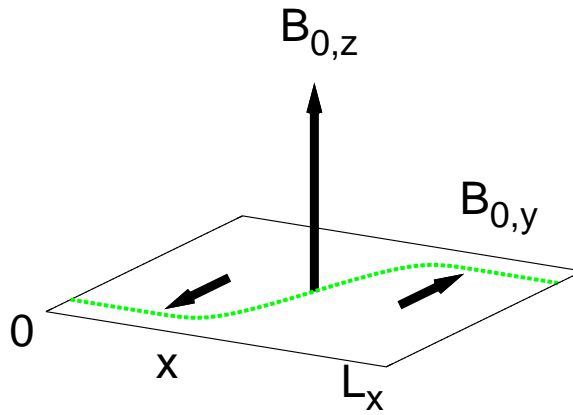


Figure 4.1: Schematic representation of magnetic equilibrium I.

given by

$$B_{0,y}(x) = -\frac{2C}{a} \cdot \frac{\sinh\left(\frac{x - \frac{L_x}{2}}{a}\right)}{\cosh^3\left(\frac{x - \frac{L_x}{2}}{a}\right)}. \quad (4.5)$$

The stability parameter can be obtained analytically for  $L_x \gg a$  [71],

$$\Delta' a = 2 \frac{[3 + (k_y a)^2] \cdot [5 - (k_y a)^2]}{(k_y a)^2 \sqrt{4 + (k_y a)^2}}. \quad (4.6)$$

Thus, the mode becomes stable if  $k_y a > \sqrt{5}$ .

The stability parameters  $\Delta'(k_y a)$  of the equilibria are summarised in Figure 4.2. The function  $\Delta'$  related to setup Eq. (1.9) (Sec. (1.4))<sup>1</sup> is plotted for  $a = 1$  and

<sup>1</sup> This equilibrium refers to Ref. [13] and is denoted as ‘‘GR’’ (Goldston Rutherford)

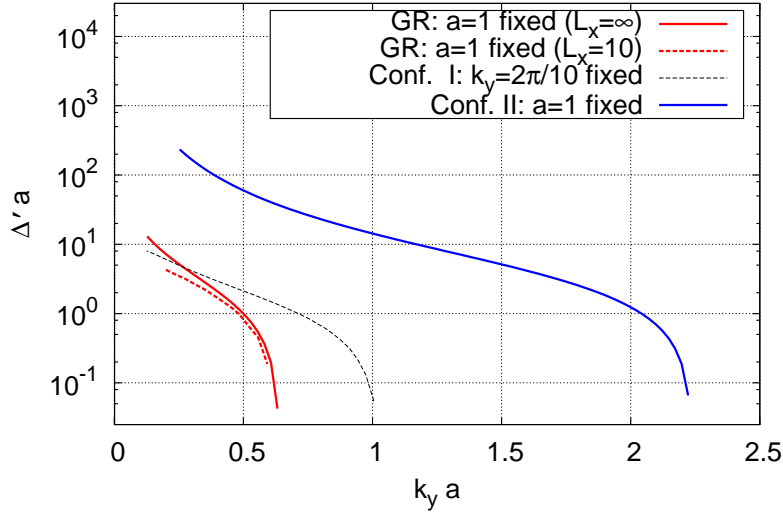


Figure 4.2: Comparison of stability parameters  $\Delta'$  of magnetic configuration I (black), magnetic equilibrium II (blue), the analytic expression Eq. (1.18) for an infinite extend of the domain in the  $x$ -direction (GR, red solid) and a finite extend (GR, red dashed). The stability threshold of the linear mode is given by the condition  $\Delta' = 0$ . In this Figure the EUTERPE normalisation is used.

various  $k_y$ . If the domain extension  $L_x$  becomes arbitrary large, Eq. (1.18) can be applied (red solid line) as was shown in Figure 1.5. For a finite  $x$ -domain  $L_x = 10$  the function slightly differs from this formula if  $k_y$  is small enough (red dotted line). The mode becomes stable if  $k_y > 0.64$ , while for very small wave vectors  $k_y < 0.2$  the large- $\Delta'$  regime is covered. The stability parameter for configuration I was obtained numerically by solving Eq. (1.17) (black dashed line). Here, the domain  $L_x = 10$  is fixed and additionally  $k_y = 2\pi m/10 = 2\pi/10$  representing the  $m = 1$  mode. Making the magnetic equilibrium scale  $a$  small enough, the stability parameter reaches arbitrary large values as well (high- $\Delta'$  regime). The stability parameter of configuration II is also depicted in Figure 4.2 (blue solid line) using Eq. (4.6) and setting  $a = 1$ . Although the shape of  $\Delta'(k_y a)$  is similar to the previous cases an offset is present.

In general the perpendicular equilibrium magnetic field  $B_{0,y}$  is connected with a parallel equilibrium current of both species,  $j_{0,s}(x) = q_s n_{0,s} u_{0,s}(x)$ . Since electrons are much faster than ions it is assumed here that only the electrons with bulk profile  $u_{0,e}(x)$  cause the perpendicular magnetic field while for ions  $u_{0,i}(x) = 0$ . For a given magnetic field the current  $\vec{j}_{0,e}$  and the corresponding bulk velocity  $u_{0,e}(x)$  can be calculated via Ampère's law as implemented in EUTERPE. Thus, the Maxwellian for the electrons is of the form

$$f_{0,e}(x, p_{\parallel}, v_{\perp}) = \frac{n_{0,e}(x)}{\sqrt{2\pi\mu}^3} e^{-\frac{\left(\frac{p_{\parallel}}{m_e} - u_{0,e}(x)\right)^2 + v_{\perp}^2}{2\mu}}. \quad (4.7)$$

This is an admissible solution of the Vlasov equation to zero-th order ( $df_{0,e}/dt = 0$ ). A natural mass ratio  $\mu = 1836$  is chosen in this thesis if not stated otherwise. Due to the ideal MHD pressure balance a consistent Maxwellian must lead to a spatially varying density  $n_{0,s}(x)$  [20]. In a low- $\beta$  equilibrium the density profile can be approximated very well by constants  $n_{0,s}$  [13].

### 4.3 Implementation of the slab geometry

The code EUTERPE is designed to solve for the gyrokinetic equation in three-dimensional toroidal geometries. To account for a one-dimensional slab it has to be modified. As the code is three-dimensional in its structure the slab implementation must fit into this framework and is thus somewhat counterintuitive.

EUTERPE uses two intrinsic coordinate systems for computations. The trajectories of the particles are pushed in cylinder coordinates  $\vec{x} = (r, z, \bar{\phi})$ . The second coordinate system is a straight field line system and used for solving the field equations,  $\vec{\xi} = (\bar{s}, \chi, \bar{\phi}) = \{\xi_i\}$  ( $i = 1, 2, 3$ ). It can be deduced directly from the three-dimensional magnetic equilibrium. These both coordinate systems are characterised by the toroidal coordinate  $\bar{\phi}$ , while the in-plane coordinates are  $(r, z)$  respectively  $(\bar{s}, \chi)$ .

In analytic calculations, however, usually the coordinate system  $(x, y, \hat{z})$  is used as depicted in Figure 4.1. Here, the toroidal coordinate is  $\hat{z}$  and the in-plane coordinates are  $x, y$ . Thus, the three coordinate systems are linked qualitatively by the mappings  $(r, z, \bar{\phi}) \leftrightarrow (\bar{s}, \chi, \bar{\phi}) \leftrightarrow (x, y, \hat{z})$ . In this chapter the mapping of  $\vec{x}$  to  $\vec{\xi}$  is discussed.

In general three-dimensional geometry the equilibrium is assumed to have nested flux surfaces. These two-dimensional surfaces themselves are curved manifolds and their interior geometry is directly connected to the three-dimensional magnetic equilibrium. However, a slab geometry is a one-dimensional equilibrium, whose flux surfaces are planes.

The task of implementing a slab geometry in EUTERPE is twofold: on the one hand it is necessary to choose proper geometric quantities, i.e. a suitable metric for a slab which describes the coefficients of the field equations. On the other hand the slab domain is subject to boundary conditions of the fluctuating fields which have to be specified at  $\bar{s} = 0$  and  $\bar{s} = 1$ , in contrast to the toroidal case where the fields have only to be specified at  $\bar{s} = 1$ .

In the following the geometric construction of the slab is outlined. To illustrate the action of the geometric quantities on the mathematical structure of the field equations, the quasi-neutrality equation is used. Without loss of generality the quasi-neutrality is written in the long wavelength approximation

$$n_e = \langle n_i \rangle + \Delta\phi = \langle n_i \rangle + \sum_{i,j=1}^3 \frac{1}{\sqrt{g}} \frac{\partial}{\partial \xi_i} \left( \sqrt{g} g^{ij} \frac{\partial}{\partial \xi_j} \phi \right). \quad (4.8)$$

An analogue to Eq. (4.8) can be formulated for Ampère’s law in curvilinear coordinates. In this form the magnetic topology is fixed by choosing values for the metric coefficients  $g^{ij}$ , defined in terms of the local gradients  $g^{ij} = \nabla \xi^i \cdot \nabla \xi^j$ , and its determinant  $g$ . On this stage the only constraint with respect to the magnetic coordinates used in EUTERPE is that  $\bar{s} \in [0, 1]$ ,  $\chi \in [0, 2\pi]$  and  $\bar{\phi} \in [0, 2\pi]$ . The inhomogeneous coordinate is by definition  $\bar{s}$ .

The concrete extensions of the slab and the relations between particle- and solver-coordinates will be described by the following specifications of the simulation domain which is shown in Figure 4.3. The specification of the geometry as explained above must be only managed in the  $(\bar{s}, \chi)$  plane, since EUTERPE has already a so-called cylinder mode. It represents a straight, non-toroidal, geometry periodic in the  $\bar{\phi}$ -direction.

As sketched in Figure 4.3 the magnetic axis is located at  $(r, z) = (r_0, 0)$  (blue

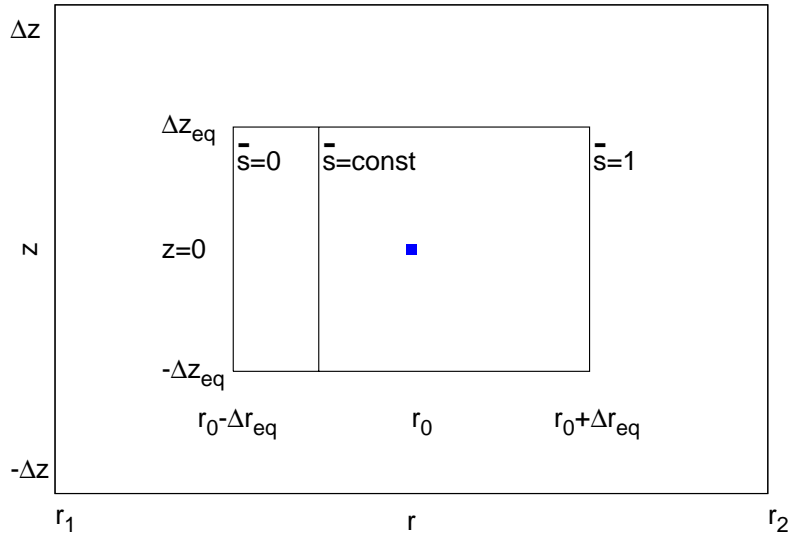


Figure 4.3: The Figure shows the dimensions of the slab used for all simulations with EUTERPE. The blue point represents the location of the magnetic axis. The connection between the particle coordinate system  $r, z$ , ( $\bar{\phi} = \text{const.}$ ) and the solver coordinates  $\bar{s}, \chi$  is explained in the text.

point). The larger of both boxes represents the coordinate background which ranges in the interval  $r_1, \dots, r_2$  horizontally and  $-\Delta z, \dots, \Delta z$  vertically.

The smaller box is the equilibrium box and encloses the whole plasma. Its extension is specified by  $[r_0 - \Delta r_{eq}, \dots, r_0 + \Delta r_{eq}] \times [-\Delta z_{eq}, \dots, \Delta z_{eq}]$ . The parameters are chosen to be  $\Delta r_{eq} = L_x/2$  and  $\Delta z_{eq} = L_y/2$  here.

The radial coordinate  $\bar{s}$  is proportional to  $r$ , including additionally the condition  $\bar{s} \in [0, 1]$ . As depicted in Figure 4.3 the  $\bar{s} = 0$  surface coincides with  $r = r_0 - L_x/2$ , while  $\bar{s} = 1$  is set at  $r = r_0 + L_x/2$ .

The  $\chi$ -values range from  $0, \dots, 2\pi$ , when  $z$  ranges in the interval  $-L_y/2, \dots, L_y/2$ .

Finally, the transformation of the coordinate systems can be summarised as

$$r(\bar{s}) = \bar{s} L_x + r_0 - \frac{L_x}{2}, \quad z(\chi) = \frac{\chi}{2\pi} L_y - \frac{L_y}{2}. \quad (4.9)$$

The corresponding gradients are  $\nabla\bar{s} = \hat{e}_r/L_x$ ,  $\nabla\chi = \hat{e}_z 2\pi/L_y$  and  $\nabla\bar{\phi} = \hat{e}_{\bar{\phi}}/r_1$ . The parameter  $r_1$  can be chosen freely, but was fixed here as  $r_1 = r_0 - L_x$ . The only non-zero components of the metric are

$$g^{\bar{s}\bar{s}} = \frac{1}{L_x^2}, \quad g^{\chi\chi} = \frac{(2\pi)^2}{L_y^2}, \quad g^{\bar{\phi}\bar{\phi}} = \frac{1}{r_1^2}. \quad (4.10)$$

Due to the choice of the metric  $g^{ij}$  the slab gets a physical length  $2\pi \cdot r_1$  in the  $\bar{\phi}$ -direction and  $L_y$  in the  $\chi$ -direction.

The second step of implementing the slab in EUTERPE is to specify the boundary conditions of the fields with respect to the solver coordinates. The perturbed fields respect Dirichlet boundary conditions at  $\bar{s} = 0, 1$  and are treated periodically in the  $\bar{\phi}$ - and  $\chi$ -direction.

The particle trajectories are also subject to boundary conditions with respect to  $\bar{s}$ ,  $\chi$ . At the boundaries of the simulation domain the particles are reflected at  $\bar{s} = 0, 1$  and periodically injected at  $\chi = 0, 2\pi$ . The points on the gyroring obey periodic boundary conditions in both directions. It turns out that this specific choice of the particle boundary conditions in the  $\bar{s}$ -direction has no essential impact on the simulations results since the dynamics of the tearing mode is mainly concentrated around the resonant layer.

## 4.4 Linear benchmark in slab geometry

At the very beginning of the simulations it has to be proven that the slab modification works correctly. One possibility is to measure the frequency  $\hat{\omega}$  of shear Alfvén waves. In this benchmark the magnetic equilibrium has only a toroidal guiding field component,  $\vec{B} = (0, 0, 1)$  which is subject to perpendicular magnetic perturbations characterised by the wave vector  $\vec{k}_\perp = (k_x, k_y)$ . The mode number  $(m, n) = (10, 1)$  was extracted during the simulations. The equilibrium domain has an extension of  $L_x = L_y = 150$ . In this benchmark  $N_p = 10^7$  electron markers were used, accompanied by one iteration cycle of the enhanced control variate method per time step.

In this test the electrons are the only kinetic species and ions are fixed serving as a neutralising background. Thus, the weights of the ions are set to zero.

Only Ampère's law is taken into account to simplify the physical setup. The quasi-neutrality condition is switched off by setting the  $B$ -spline coefficients of the electrostatic potential  $\phi$  to zero.

From a generalised dispersion relation of a sheared slab the dispersion of Alfvén

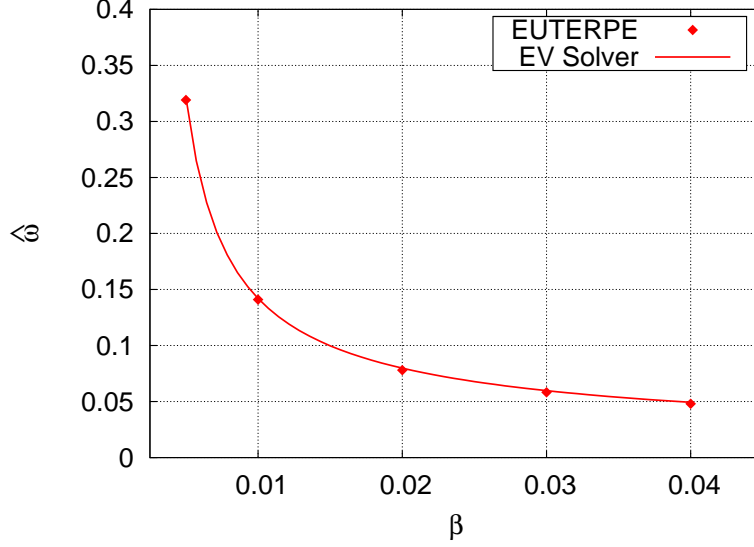


Figure 4.4: The frequency of the shear Alfvén wave over  $\beta$ . The benchmark is successful, thus the slab geometry has been implemented correctly.

modes can be derived as <sup>1</sup>

$$k_{\perp}^2 d_e^2 + 1 = 2Z_3(\zeta_e). \quad (4.11)$$

Here,  $\zeta_e = \omega / (\sqrt{2\mu} k_{\parallel})$  is the complex argument of the plasma dispersion function of third order,  $Z_3$ . The  $n$ -th order plasma dispersion function  $Z_n(\zeta_e)$  is defined by [62]

$$Z_n(\zeta) = \frac{1}{\sqrt{\pi}} \int_{-\infty}^{\infty} dt \frac{t^n e^{-t^2}}{t - \zeta}. \quad (4.12)$$

The complex algebraic equation (4.11) was solved for  $\omega(\beta)$  numerically with a root finder.

In Figure 4.4 the frequency depending on  $\beta$  is shown. The length scale of the perturbation in  $x$ -direction is  $L_x/25$ . The frequency obtained with EUTERPE and the results of the eigenvalue (EV) solver agree to high accuracy. Therefore, the benchmark is successful and the slab geometry has been implemented correctly.

<sup>1</sup>The most general dispersion relation of a sheared slab with constant equilibrium gradients will be derived in Sec. 5.1.



# 5 Linear simulations of the tearing mode

## 5.1 Linear dispersion relation

In this chapter the dispersion relation of linear tearing modes is discussed. The most general linear eigenvalue problem of the gyrokinetic equation in a slab is derived by means of Eqs. (2.5–2.10) without any restriction of the scales involved.

Both kinetic ions and electrons contribute to the source terms of the field equations. The plasma is assumed to be inhomogeneous in general by employing a local approach of temperature and density gradients in contrast to the global current profile, i. e. the gradients have constant values  $n'_{0,s}$  and  $T'_{0,s}$  respecting the  $x$ -direction. The linear mode is assumed to be two-dimensional, thus setting  $\partial_z = 0$ . This restriction does not narrow the essential physics, since otherwise only the resonant surface is shifted in space. However, three-dimensional nonlinear tearing can indeed differ substantially from two-dimensional tearing [2, 72].

Using the  $\delta f$ -ansatz, the linearised Eq. (2.10) for the perturbed part of the distribution function reads

$$\dot{R}_s^1 \frac{\partial f_{0,s}}{\partial \vec{R}} + \dot{p}_s^1 \frac{\partial f_{0,s}}{\partial p_{\parallel}} = -\frac{\partial \delta f_s}{\partial t} - \dot{R}_s^0 \frac{\partial \delta f_s}{\partial \vec{R}} - \dot{p}_s^0 \frac{\partial \delta f_s}{\partial p_{\parallel}}.$$

The unperturbed and perturbed contributions of the particles trajectories are given by Eqs. (2.5) (Sec. 2.2).

Applying the usual Fourier ansatz for the spatio-temporal structure,  $\partial_t \mapsto -i\omega$ ,  $\partial_y \mapsto ik_y$ , one obtains

$$\delta f_s = f_{0,s} \frac{\left(\phi - \frac{p_{\parallel}}{m_s} A\right)}{k_{\parallel}(x) \left(\frac{\omega}{k_{\parallel}(x)} - \frac{p_{\parallel}}{m_s}\right)} \left[ k_y \kappa_s + \frac{q_s}{\tau_s} k_{\parallel}(x) \left(\frac{p_{\parallel}}{m_s} - u_{0,s}(x)\right) \right]. \quad (5.1)$$

Two-dimensional reconnection leads to a parallel wave vector  $k_{\parallel}(x) = k_y B_{0,y}(x)$ . The generalised gradient term  $\kappa_s$  has been defined in Eq. (2.10) (Sec. 2.2). The  $x$ -dependency of the problem is kept, since it is necessary to resolve the spatial structure of the layer.

The field equations close the Vlasov-Maxwell system. For vanishing ion to electron temperature ratio  $\tau \ll 1$ , the approximation  $\langle n_i \rangle \approx n_i$  is employed and analogously

for the current  $\langle j_{\parallel,i} \rangle$ <sup>1</sup>. This is an important modification for all subsequent benchmarks carried out, since otherwise the exact gyroaveraging operator leads to an eigenvalue problem for a relatively complicated set of integro-differential equations. The effort to solve this problem is quite beyond the scope of this work.

In the subsequent benchmarks the long wavelength approximation is used. With these assumptions the quasi-neutrality equation reads

$$\begin{aligned} \delta n_i + \Delta \phi &= \delta n_e \\ \int 2\pi v_{\perp} dv_{\perp} d(p_{\parallel}/m_i) \delta f_i + \Delta \phi &= \int 2\pi v_{\perp} dv_{\perp} d(p_{\parallel}/m_e) \delta f_e. \end{aligned} \quad (5.2)$$

The density responses  $\delta n_s$  contain terms  $\delta n_{s,\phi}$  related to the electrostatic potential, and terms  $\delta n_{s,A}$  related to the vector potential resulting from the corresponding terms related to  $\phi$ ,  $A$  in Eq. (5.1).

The ‘‘current’’ in Ampère’s law is given by the first moment of  $\delta f_s$  with respect to the momentum coordinate  $p_{\parallel}/m_s$ <sup>2</sup>

$$\begin{aligned} -\frac{1}{\beta} \Delta A + \sum_s \mu_s q_s^2 A &= \sum_s \langle j_{\parallel,s} \rangle \\ &= \sum_s q_s \int 2\pi v_{\perp} dv_{\perp} d(p_{\parallel}/m_s) (p_{\parallel}/m_s) \delta f_s \\ &= \sum_s \delta j_s. \end{aligned} \quad (5.3)$$

The contribution of each species to the current contains parts  $\delta j_{s,A}$  related to  $A$ , and terms  $\delta j_{s,\phi}$  related to  $\phi$ . The complete set of differential equations, Eqs. (5.2, 5.3), can be cast into the final eigenvalue problem

$$\begin{aligned} \frac{d^2 \phi}{dx^2} &= k_y^2 \phi - \sum_s q_s (\delta n_{s,\phi} \phi + \delta n_{s,A} A), \\ \frac{d^2 A}{dx^2} &= \left( \beta \sum_s \mu_s q_s^2 + k_y^2 \right) A - \sum_s \beta (\delta j_{s,\phi} \phi + \delta j_{s,A} A). \end{aligned} \quad (5.4)$$

---

<sup>1</sup> By experience with EUTERPE the approximation  $\langle n_i \rangle \approx n_i$  is valid to a high degree for the benchmarks of the tearing mode considered here. The simulation results practically do not change when varying  $\tau = \mathcal{O}(10^{-3}), \dots, \mathcal{O}(1)$ .

<sup>2</sup> Note that normalised quantities are used so  $q_e = -1$ ,  $q_i = 1$  and  $v_i = \sqrt{\tau}$ ,  $v_e = \sqrt{\mu}$ .

The coefficients are obtained by inserting Eq. (5.1) into Eqs. (5.2, 5.3)

$$\delta n_{s,\phi} = -\frac{1}{k_{\parallel}} \left( k_y K_s^0 + \frac{q_s}{\tau_s} k_{\parallel} \langle V_s^1 \rangle \right), \quad (5.5)$$

$$\delta n_{s,A} = \frac{u_{0,s}}{k_{\parallel}} \left( k_y K_s^0 + \frac{q_s}{\tau_s} k_{\parallel} \langle V_s^1 \rangle \right) + \frac{1}{k_{\parallel}} \left( k_y K_s^1 + \frac{q_s}{\tau_s} k_{\parallel} \langle V_s^2 \rangle \right), \quad (5.6)$$

$$\delta j_{s,\phi} = -\frac{q_s}{k_{\parallel}} \left( k_y K_s^1 + \frac{q_s}{\tau_s} k_{\parallel} \langle V_s^2 \rangle \right) - \frac{q_s u_{0,s}}{k_{\parallel}} \left( k_y K_s^0 + \frac{q_s}{\tau_s} k_{\parallel} \langle V_s^1 \rangle \right), \quad (5.7)$$

$$\begin{aligned} \delta j_{s,A} &= \frac{q_s u_{0,s}^2}{k_{\parallel}} \left( k_y K_s^0 + \frac{q_s}{\tau_s} k_{\parallel} \langle V_s^1 \rangle \right) + \frac{2q_s u_{0,s}}{k_{\parallel}} \left( k_y K_s^1 + \frac{q_s}{\tau_s} k_{\parallel} \langle V_s^2 \rangle \right) \\ &+ \frac{q_s}{k_{\parallel}} \left( k_y K_s^2 + \frac{q_s}{\tau_s} k_{\parallel} \langle V_s^3 \rangle \right). \end{aligned} \quad (5.8)$$

The functions  $K_s^m(x, \omega)$  with  $m$  integer contain all gradient terms according to

$$K_s^m(x, \omega) = \kappa_{n,s} \langle V_s^m \rangle - \frac{1}{2} \kappa_{T,s} \langle V_s^m \rangle + \kappa_{T,s} \langle V_s^{m+2} \rangle - \frac{du_{0,s}}{dx} \frac{\langle V_s^{m+1} \rangle}{v_s^2}. \quad (5.9)$$

The moments  $\langle V_s^n \rangle$  are defined in terms of  $Z_n(\zeta_s)$  with  $\zeta_s = \left( \frac{\omega}{k_{\parallel}} - u_{0,s} \right) / (\sqrt{2}v_s)$ ,

$$\begin{aligned} \langle V_s^n \rangle(x, \omega) &= \left( \sqrt{2}v_s \right)^{n-1} \frac{1}{\sqrt{\pi}} \int_{-\infty}^{\infty} dt \frac{t^n e^{-t^2}}{t - \left[ \frac{1}{\sqrt{2}v_s} \left( \frac{\omega}{k_{\parallel}(x)} - u_{0,s}(x) \right) \right]} \\ &= \left( \sqrt{2}v_s \right)^{n-1} Z_n(\zeta_s). \end{aligned} \quad (5.10)$$

It is important to note that  $k_{\parallel}(x)$  and  $u_{0,s}(x)$  depend on  $x$ . These functions also appear within the plasma dispersion function, so the solution of this kinetic eigenvalue problem is quite ambitious.

It is important to take care of the correct use of  $Z_n(\zeta_s)$  in the complex plane when crossing the layer from  $x > 0$  to  $x < 0$ , where  $k_{\parallel}$  crosses zero. Since the solution of the dispersion relation Eq. (5.4) should always give an instability, it must hold  $\gamma > 0$  everywhere. Let  $k_{\parallel}(x) > 0$  if  $x > 0$ , and vice versa. If  $k_{\parallel} > 0$ , then  $\Im(\zeta_s) > 0$  and one can use the plasma dispersion function  $Z_n(\zeta_s)$  defined in Eq. (5.10). If one crosses the layer, the sign of  $k_{\parallel}$  switches because the direction of the equilibrium magnetic field lines switches as well. Then  $\Im(\zeta_s) < 0$ , although  $\gamma > 0$  is still demanded. The application of Eq. (5.10) describes now a stable mode. However, the domain  $x > 0$  has no special features compared with  $x < 0$ . This can be understood by inspecting the mode structure of  $A$ , which is known to be symmetric with respect to  $x$  and so the physics is the same in both domains. Therefore, one has to maintain the condition of an unstable mode and one must replace  $Z_n$  with the complementary plasma dispersion function  $\bar{Z}_n$ , defined by  $\bar{Z}_n(\zeta_s) = -Z_n(-\zeta_s)$ . This function is analytic with respect to  $\omega$  as well, but it incorporates the property to describe instabilities when  $\Im(\zeta_s) < 0$ . This gives the correct description of the tearing mode

when  $k_{\parallel} < 0$ .

The complete linear dispersion relation, Eqs. (5.4), has to be solved for  $\omega(k_y)$ , using the coefficients defined by Eqs. (5.5–5.8). The eigenvalue problem defined by Eqs. (5.4) is the most general expression for an eigenvalue problem in a slab with constant density and temperature profiles, since neither a special current profile is fixed nor a scale ordering is implied. For instance, it is common in analytical work on slab tearing modes to employ  $a > d_e$  which matches experimental reconnection setups. From the mathematical point of view this is a restriction to the applicability of the resulting dispersion relation. The dispersion relation derived here can be applied to every physical situation.

The solution of the eigenvalue problem Eqs. (5.4) is referred to as full tearing mode or just tearing mode in this thesis. Note that this case includes both fields  $A$ ,  $\phi$  and both kinetic species.

The full tearing mode model can be simplified by neglecting the ion response as well as the fluctuations of the electrostatic field. The resulting solution of the dispersion relation is referred to as electron tearing mode. This model is motivated by the observation that electrons play always the dominant role in the dynamics due to the large natural mass ratio  $\mu$ . The eigenvalue problem of the electron tearing mode thus reduces to

$$\begin{aligned} \frac{d^2 A}{dx^2} &= (\beta\mu + k_y^2) A + \delta j_{e,A} A \\ &= (\beta\mu + k_y^2) A - \beta A \frac{q_e}{k_{\parallel}} [u_{0,e}^2 (k_y K_e^0 + q_e k_{\parallel} \langle V_e^1 \rangle) \\ &\quad + 2u_{0,e} (k_y K_e^1 + q_e k_{\parallel} \langle V_e^2 \rangle) + k_y K_e^2 + q_e k_{\parallel} \langle V_e^3 \rangle]. \end{aligned} \quad (5.11)$$

This model also permits reconnection and serves as a minimal electromagnetic model<sup>1</sup>. The eigenvalue problem Eq. (5.11) is still difficult to solve. Moreover, no reconnection-typical scale ordering nor a specific current profile is imposed. Thus, a simple analytical derivation of the growth rate of the electron tearing mode will be given following Ref. [20].

The ideal MHD domain was described by Eq. (1.16). For the sake of simplicity it is assumed that gradients of temperature and density vanish. Close to the resonant layer  $x \approx L_x/2$ , the variation of the current can be neglected setting  $du_{0,e}/dx = 0$  and so  $K_e^m = 0$ , too. It is a common approximation to treat the limit  $u_{0,e} \ll v_e$  and

---

<sup>1</sup>The dispersion relation Eq. (5.11) simplifies further when the shifted Maxwellian is being removed using  $u_{0,e} = 0$  and the gradients are set to zero. The singular layer vanishes and it follows  $K_e^m = 0$ . Since the equations do not depend on  $x$  anymore, a harmonic spatial exponential  $e^{ik_x x}$  is an eigenfunction. Including the substitution  $k_{\parallel} \mapsto k_z$  one gets

$$\begin{aligned} -k_x^2 &= (\beta\mu + k_y^2) - \beta \langle V_e^3 \rangle, \\ -k_{\perp}^2 &= \beta\mu (1 - 2Z_{3,e}), \end{aligned}$$

which is the electron Alfvén wave, Eq. (4.11) (Sec. 4.1).

so all terms in Eq. (5.11) proportional to  $u_{0,e}$  are small, resulting in

$$\frac{d^2 A}{dx^2} = (\beta\mu + k_y^2) A - \beta A \langle V_e^3 \rangle. \quad (5.12)$$

At  $x \approx L_x/2$  the spatial structure in the  $x$ -direction varies much stronger than in the  $y$ -direction ( $\partial_x \gg k_y$ ), therefore,

$$\frac{d^2 A}{dx^2} \approx (\beta\mu - 2\beta\mu Z_{3,e}) A = \zeta_e^2 Z_{0,e} A. \quad (5.13)$$

The moment  $\langle V_e^3 \rangle$  has been expressed in terms of  $Z_3(\zeta_e)$  with the argument  $\zeta_e = \omega / (\sqrt{2}v_e k_{\parallel})$ . The relation  $Z_{3,e} = 1/2 + \zeta_e^2 Z_{0,e}$  reduces the order of the plasma dispersion function [62].

The inner layer scale  $\delta_{in}$  related to the perturbed current is defined by the condition  $|\zeta_e| \approx 1$ , or equivalently  $k_{\parallel}(\delta_{in})v_e \approx \gamma$ . This estimation of the width of the electron current channel is often used in kinetic calculations [18], since the plasma dispersion function has a peaked profile which is extended up to a scale  $\delta_{in}$ .

Eq. (5.13) can be manipulated similar to the procedure described in Sec. 1.4 giving the growth rate [18, 20]

$$\gamma = \Delta' \frac{k_y v_e d_e^2}{2\sqrt{\pi} l_s}. \quad (5.14)$$

This is the simplest kinetic analytical dispersion relation for slab tearing modes valid in the limit  $\Delta' d_e \ll 1$ . It reproduces the same scaling with  $k_y$  and  $d_e$  as the result of the fluid model in Sec. 1.4.2.

An extended calculation of the growth rate within a hybrid approach including  $\phi$  can be found in Ref. [46] which also uses a detailed matched asymptotic expansion for both fields. The linear equations in this reference can be mapped to the eigenvalue problem derived here.

## 5.2 Benchmark of the tearing mode without gradients

The full tearing mode as well as the electron tearing mode are simulated with EUTERPE. The results are benchmarked solving the associated eigenvalue problems Eq. (5.4, 5.11) by means of a shooting method. The shooting method relies on a reformulation of the eigenvalue problem into a Riccati differential equation. The algorithm originates from Ref. [73].

The algorithm will be explained shortly by inspecting a general set of complex coupled first order differential equations defined on the domain  $[0, L_x]$  [74]. The

vectors  $d\vec{u}/dx$  and similarly  $d\vec{v}/dx$  may fulfil the equations

$$\begin{aligned}\frac{d\vec{u}}{dx} &= A(x, \omega) \vec{u} + B(x, \omega) \vec{v}, \\ \frac{d\vec{v}}{dx} &= C(x, \omega) \vec{u} + D(x, \omega) \vec{v}.\end{aligned}\tag{5.15}$$

The matrices  $A, \dots, D$  may specify the problem with the unknown eigenvalue  $\omega$  whereas boundary conditions for  $\vec{u}, \vec{v}$  at  $x = 0$  and  $x = L_x$  are set. One introduces the unknown Riccati matrix  $R(x, \omega)$  by the definition  $\vec{u} = R\vec{v}$ . Inserting this ansatz into Eq. (5.15) the nonlinear Riccati equation becomes

$$\frac{dR}{dx} = -RCR - RD + AR + B.\tag{5.16}$$

For the solution of Eq. (5.16) the boundary conditions  $R(0, \omega) = R(L_x, \omega) = 0$  are employed. The shooting code integrates  $R(x, \omega)$  according to Eq. (5.16) from the left starting at point  $x = 0$  and from the right starting at point  $x = L_x$  to a certain inner point  $x_f \in (0, L_x)$ . The corresponding solutions are denoted  $R_l(x_f, \omega)$  and  $R_r(x_f, \omega)$ . It can be shown that the continuity of the solutions  $\vec{u}, \vec{v}$  and  $d\vec{u}/dx, d\vec{v}/dx$  at  $x = x_f$  is guaranteed if the necessary and sufficient condition  $\det [R_l(x_f, \omega) - R_r(x_f, \omega)] = 0$  is fulfilled. Thus, for a fixed matching point  $x_f$  the search for the eigenvalue  $\omega$  is reformulated into finding the complex root  $\omega$  of the complex determinant depending on the matrices  $R_r(x_f, \omega), R_l(x_f, \omega)$ . The eigenfunctions are obtained in a separate step by integrating  $d\vec{v}/dx = (CR + D)\vec{v}$  and  $\vec{u} = R\vec{v}$  backwards from  $x_f$  with the already obtained  $R(x, \omega)$ .

The algorithm also includes an adaptive step size method for the spatial integration and gives high precision results even when strong spatial variations are present.

Eqs. (5.4, 5.11) were implemented into the shooting code. For the eigenvalue problem of the full tearing mode, Eq. 5.15 reduces to a set of four first-order differential equations with  $u_1 = \phi, u_2 = A, v_1 = d\phi/dx,$  and  $v_2 = dA/dx$ . It is an unique advantage to solve the exact eigenvalue problem containing all the physics within. Numerically exact benchmarks of the full tearing mode are very rarely found in literature [25] in contrast to the electron tearing mode [20, 26]. Principally, it is quite possible to extend this low- $\beta$  description including the parallel magnetic perturbations  $\delta B_{\parallel}$ , solving a set of three complex differential equations<sup>1</sup>.

The plasma is assumed here to be homogeneous employing a constant temperature and density. Magnetic field configuration I was chosen which is motivated by a direct comparison of the dispersion relation of Ref. [26]. The shear length of the magnetic equilibrium is given by  $l_s = 1/(C\beta\sqrt{\mu}) \approx 23.3$  using  $\beta = 10^{-3}$ . The constant  $C$  is always set to unity if not stated otherwise. The size of the simulation box is

---

<sup>1</sup>This task has never been solved with a shooting code. Although simulations results are available in this case [38], it is common to use much less exact dispersion relations obtained by analytic approaches, often in asymptotic limits.

Despite the fact that exact asymptotic limits required by analytic derivations can not be achieved by numerical simulations, simulations results often still deviate from the analytic dispersion relation up to 50% [29]. This might enlight the power of the Riccati method presented here.

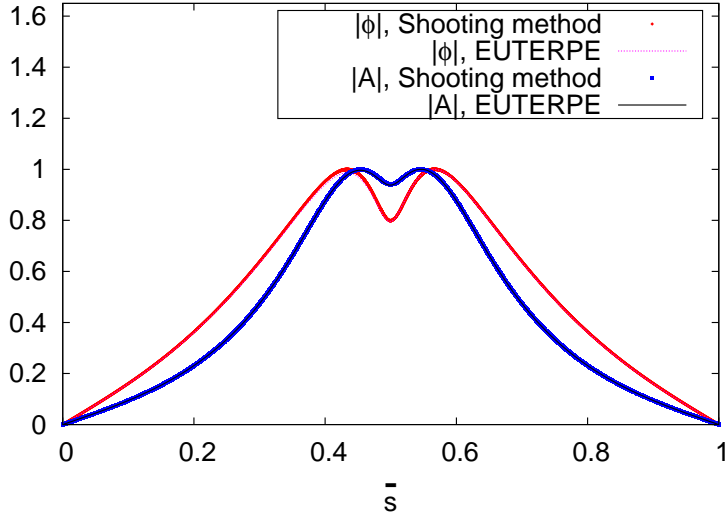


Figure 5.1: Spatial eigenmode structure of  $A$  and  $\phi$  both for EUTERPE and the shooting method ( $a = 0.9$ ). The maximum amplitude of both fields is normalised to unity. EUTERPE is able to perform linear reconnection simulations to high accuracy.

$L_x \times L_y = 10 \times 10$ . In EUTERPE the long wave length approximation of the quasi-neutrality condition was used to match the required assumptions of the eigenvalue problem. The cold ion limit was enforced by setting  $\tau = 10^{-3}$ . For the simulations here the resolution of the domain accounts for  $n_{\bar{s}} = 256$  and  $n_{\chi} = 16$  points. An amount of  $N_p = 10^7$  markers for each species was used with a time step  $\Delta t = 0.05$ . The clear numerical verification of the mode needs about 64 CPUh which is relatively cheap. The filter in EUTERPE was adjusted to pass only the  $m = 1$  mode. In case of the electron tearing mode, the weights of the ions have been set to zero suppressing the ion response. When simulating the electron tearing mode the electrostatic potential was switched off as sketched in Sec. 4.4.

For numerical reasons it is necessary to use a sufficiently high resolution of all relevant scales. The electron current layer of width  $\delta_e \approx \gamma l_s k_y / v_e \approx 0.17$ , with  $k_y = 2\pi/10 \approx 0.62$ , has been resolved with at least four points. The reconnection process is mainly induced by inertia effects with the relevant collisionless electron skin depth  $d_e = 1/\sqrt{\beta\mu} \approx 0.7$  which is somewhat smaller than the ion sound radius  $\rho_{S,e} = 1$ . This corresponds to a spatial resolution of the skin depth with 17 points. The collisionless ion skin depth  $d_i = 1/\sqrt{\beta} \approx 31.6$  is much larger than the simulation box size and plays no role. The ion current channel of width  $\delta_i \approx \gamma l_s / k_y \approx 7.3$  is also not of importance due to the large mass ratio. In the cold ion limit the Larmor radius becomes much smaller than any other scale in the system,  $\rho_i \approx 0.03 \ll \delta_e$ .

At first a fixed equilibrium scale  $a = 0.9$  is chosen to benchmark a single eigenvalue and the corresponding eigenfunctions in the full tearing mode case. From EUTERPE simulations a growth rate  $\gamma = 0.37$  is obtained, while the result of the shooting method is  $\gamma = 0.3694$ . A comparison between the mode structures calcu-

lated with EUTERPE and the shooting code is shown in Figure 5.1. The vector potential  $A$  and the electrostatic potential  $\phi$  calculated with EUTERPE fit very well with the eigenmodes obtained with the shooting code. The mode structure of  $\phi$  in the vicinity of the resonant layer is somewhat wider than for  $A$  and typically varies on scales  $\rho_{S,e}$  [46], reflected by the estimate  $d_e < \rho_{S,e}$ .

The benchmark was extended to a broad range of values of  $a$  measuring the growth

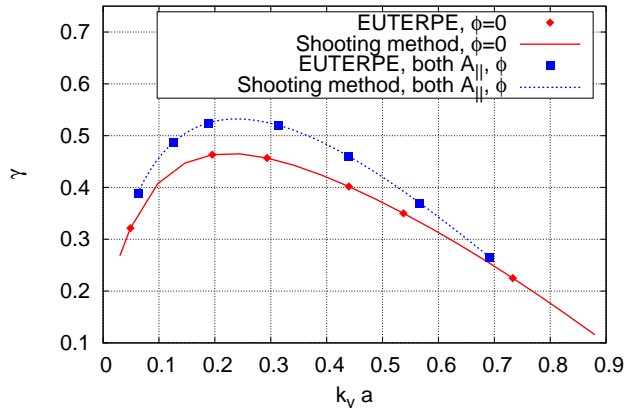


Figure 5.2: Benchmark of the growth rate over  $k_y a$  for fixed  $k_y = 2\pi/10$  and both tearing mode cases. EUTERPE is able to simulate reconnection to very high precision.

rate. Starting in the range of marginal stability with  $a \approx 1.4$  ( $k_y a \approx 0.9$ ), the equilibrium current width was decreased approaching  $a \approx 0.08$  ( $k_y a \approx 0.05$ ). Although the variation of  $a$ , especially if  $a \ll d_e$ , allows formally tearing mode solutions, this kind of scale variation is rather unusual, as will be discussed below. For small values  $a \approx 0.08$ , tearing modes with poloidal mode number  $m = 2, 3, \dots$  exist being more unstable than the  $m = 1$  mode, but are filtered out. The dispersion relation  $\gamma(k_y a)$  obtained with EUTERPE compared with the results of the shooting method are shown in Figure 5.2. The red curve and points refer to the growth rate of the reduced (electron) tearing mode model, whereas the blue values represent the dispersion relation of the full tearing mode. The mode becomes stable at  $a \approx 1.4$  ( $k_y a \approx 1.1$ ). Reducing the equilibrium current width a maximum growth rate  $\gamma = 0.52$  was found at  $a = 0.42$  ( $k_y a \approx 0.25$ ) for the tearing mode case which is somewhat larger than for the electron tearing mode ( $\gamma \approx 0.47$ ). In the case of small values of  $a \approx 0.08$  the modes require a very high spatial resolution, but are benchmarked to high precision. Thus, the adaptive step size integration of the shooting code is able to face this ambitious task and covers the simulation results perfectly. The depicted growth rates of both models (with and without  $\phi$ ) differ only slightly over the whole range of  $a$ . The comparison makes evident that the electrostatic potential gives a small correction compared to the electron tearing case. The approximation becomes better for  $a > 1.1$  ( $k_y a > 0.7$ ). For the parameter chosen here ( $d_e < \rho_{S,e}$ ) it has been shown analytically that the electrostatic response can

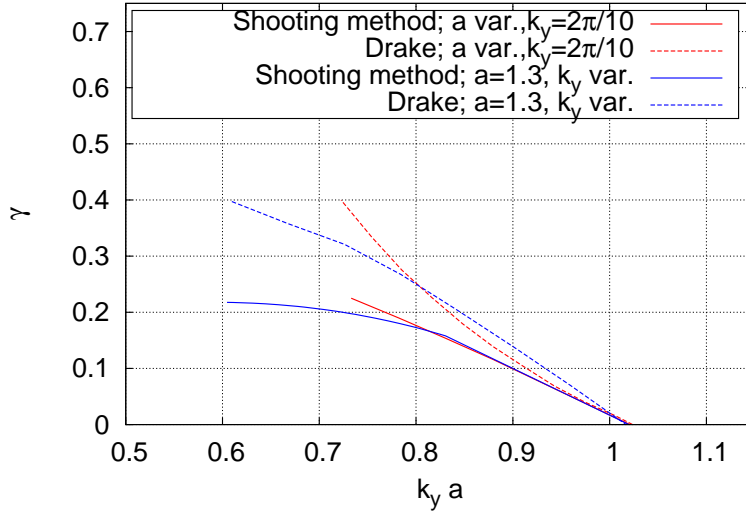


Figure 5.3: Comparison between the analytical result of Drake with the result of the shooting method (electron tearing mode case). The blue curves match the physical ordering  $d_e \ll a$  much better than the red curves ( $d_e > a$ ).

be neglected in the regime  $\Delta' d_e \ll 1$  [18]. In the medium range  $0.1 < a < 1.3$  the electrostatic potential destabilises the electron tearing mode more dominantly.

To make a closer contact to literature the analytic dispersion relation of the electron tearing mode Eq. (5.14), the result of Drake [18] and the numerically exact dispersion relation are compared.

In contrast to the strict derivation of Eq. (5.14), Drake obtained a similar dispersion relation by using heuristic scaling arguments allowing the estimate of the perturbed current width and structure of the vector potential. These both results differ by a prefactor  $1/\sqrt{\pi}$  which can be summarised to

$$\gamma = \Delta' \frac{k_y v_e d_e^2}{2l_s} \left( \frac{1}{\sqrt{\pi}} \right)^l, \quad (5.17)$$

setting  $l = 0$  (Drake) and  $l = 1$  (Eq. 5.14, [20]). The constant prefactors are less interesting, rather the correct dependence of  $\gamma$  on the essential values  $k_y$ ,  $\Delta'$  and  $l_s$  matters. The case  $l = 0$  is compared with the dispersion relation of the electron tearing mode obtained with the shooting code.

Mainly two setups of parameters are of interest, either a variation of  $a$  with a constant wave vector or vice versa. The resulting dispersion relations are depicted in Figure 5.3. The growth rate depending on  $a$  with fixed  $k_y = 2\pi/10$  was discussed in the previous benchmark. Drake's result is only valid in the small- $\Delta'$  range which is achieved when  $k_y a \gtrsim 0.7$  and the constant- $\Psi$  approximation becomes valid. The red curves show the contrast of Eq. (5.17) to the shooting method. When  $a$  is varied as in the previous benchmark one reaches values  $k_y a \approx 0.4$ , consequently  $a \lesssim d_e \sim 0.7$ . Due to this unusual reversion of reconnection relevant scales, Drake's result can not

cover this parameter range. The analytical dispersion relation Eq. (5.17) even does not match the qualitative behaviour of the curve obtained by the shooting method if  $k_y a \lesssim 0.7$ .

The condition  $d_e \ll a$  fulfils better the assumptions of the derivation of Eq. (5.17). This result is shown in Figure 5.3 indicated by the blue curves. Here  $d_e \approx 0.7 \lesssim a = 1.3$  is commonly used and  $k_y$  is varied. The typical  $x$ -variation of  $A$  is in the order of  $d_e$  ( $\nabla_{\perp}^2 A \approx A/d_e^2$ ) at the resonant layer and is much larger than the variation in  $y$ -direction. As in the derivation of Eq. (5.14) adopted,  $k_y \ll \partial_x$  is well satisfied for  $k_y a \approx 1$ . Thus, the qualitative shape of the both the dispersion relation obtained with the shooting method and Drake's result is the same.

### 5.3 Benchmark of the tearing mode with gradients

The exact MHD equilibrium condition in a slab requires the magnetic pressure  $p_B$  to be balanced by kinetic pressure according to  $p(x) + p_B(x) = \text{const}$ . Inspecting a simple equation of state of the plasma,  $p(x) = n(x)T(x)$ , the density and temperature profiles  $n(x)$  and  $T(x)$  must satisfy the ideal MHD pressure balance self-consistently. The derived pressure gradient  $\nabla_{\perp} p$  arises due to variations of temperature and density according to  $\nabla_{\perp} p = \nabla_{\perp} n \cdot T + n \cdot \nabla_{\perp} T$ . Instead of calculating the pressure gradient derived from the exact functions  $n$ ,  $T$ , the variations of the background are set to constants according to  $\nabla_{\perp} n \approx n_0/L_n$  and  $\nabla_{\perp} T \approx T_0/L_T$  independent from each other [18]. This approach simplifies analytic work, because the globally varying pressure profile is essentially replaced by the scales of pressure variation.

The tearing mode is strongly localised at the resonant surface and therefore it is expected that in this region equilibrium gradients will play the major role. This non-consistent, local approach in the global slab domain is adopted for all subsequent simulations including diamagnetic effects.

The aim of the investigations here is to observe and benchmark the electron tearing mode in the presence of diamagnetic effects. Similar to the parameter variation in Sec. 5.2, the length scale  $a$  was changed and the linear growth rate and real frequency was measured. The extensions of the simulation box are  $L_x = L_y = 10$  while employing magnetic configuration I and  $\beta = 10^{-3}$ . A Fourier filter selects the  $m = 1$  mode, therefore, the wave vector  $k_y = 2\pi/10$  of the perturbation is fixed. The temperature ratio  $\tau = 1$  has been used while including the exact gyroaveraged ion response  $\langle n_i \rangle$  and long wavelength approximation is enforced during the simulations. A spatial resolution of  $n_{\bar{s}} = 256$  points in radial direction, a time step  $\Delta t = 0.1$  and up to  $N_p = 4 \cdot 10^7$  electron markers suffice for the numerical convergence of the growth rates and give relatively short simulation times. A temperature gradient of  $\kappa_{T,e} = 1$  for the electrons has been chosen without a density variation ( $\kappa_{n,e} = 0$ ). The temperature gradient is rather large compared with a realistic physical setup, since it changes significantly over one ion sound radius  $\rho_{S,e}$ .

The dispersion relation  $\gamma(k_y a)$  obtained with EUTERPE is depicted in Figure 5.4 (red points). The magnetic equilibrium scale ranges from  $a = 0.5, \dots, 1.3$  ( $k_y a =$

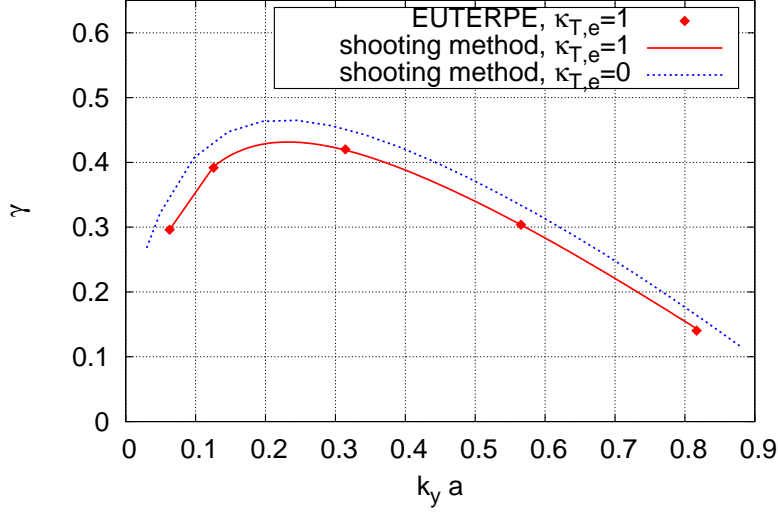


Figure 5.4: Growth rate of the drift tearing mode depending on  $a$  ( $\kappa_{T,e} = 1$ ,  $k_y = 2\pi/10$ ) obtained with EUTERPE (points) and the shooting method (solid lines). The dispersion relation for the case  $\kappa_{T,e} = 0$  is solved with the shooting method (blue line). The benchmark of the growth rates succeeded.

0.3, ..., 0.81). These results were compared with the results of the shooting code (red solid line). The blue curve shows the case when no electron temperature gradient is present indicating the stabilising influence of diamagnetic effects on the mode. Although a rather high temperature gradient is apparent the mode gets stabilised only slightly.

The real frequency  $\hat{\omega}$  depending on  $a$  obtained with both EUTERPE and the shooting method are shown in Figure 5.5. The simulation results are measured via time series of a field value at a fixed point in the simulation domain. Using several periods the mean value of the periods was used to calculate the frequency. The simulations in this range of parameter require a high computational effort, since the frequencies do not differ very much when changing  $a = 0.3, \dots, 1.3$  ( $k_y a = 0.18, \dots, 0.81$ ). The comparison visualises small differences between the results of EUTERPE and the shooting method. The error of measurement results from the standard deviation of the repeated simulations for fixed  $a$  and is depicted, too. It turned out that the size of the momentum sphere matters. Even though  $\kappa_{v,e} = 8, \dots, 9.5$  exceeds the thermal speed widely, it seems that the high thermal speed affects the frequencies much more than the growth rates due to the relatively large value  $C = 1$ . The accuracy of the simulation results could be improved by increasing the number of markers, but the results shown in Figure 5.5 might suffice to prove that EUTERPE can describe even drift tearing modes to high accuracy.

The kinetic theory of Drake [18] predicts that the frequency of the drift tearing mode is characterised roughly by the diamagnetic frequency  $\omega_T^*$  only,  $\hat{\omega} \approx \omega_T^*/2 =$

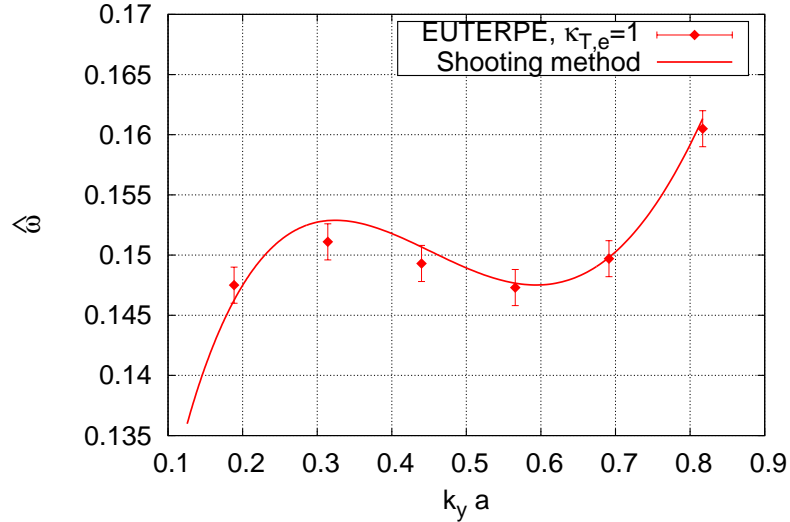


Figure 5.5: Frequency of the drift tearing mode depending on  $a$  ( $\kappa_{\text{T},e} = 1$ ,  $k_y = 2\pi/10$ ) obtained with EUTERPE (red points) and the shooting method (red line). At first this high precision benchmark visualises small differences between the results of both methods.

$k_y \kappa_{\text{T},e}/2 \approx 0.3$ . This estimation is valid in the range  $\Delta' d_e \ll 1$  which corresponds here to  $0.8 \lesssim k_y a$ . The theory shows that the drift frequency is a constant in this range, consistent with the drift frequencies obtained with EUTERPE. For  $k_y a < 0.8$  ( $\Delta' d_e \approx 1$ ) it has been proven with EUTERPE that  $\hat{\omega}$  is also nearly constant for various  $a$ . Although the prediction is roughly twice the frequency with  $k_y a = 0.81$ ,  $\omega_{\text{T}}^*/2 \approx 2 \cdot 0.16$  and thus does not match the values of the simulation, it gives the correct order of magnitude. The confirmation of this analytical result requires further extended parameter studies in the corresponding low- $\Delta'$  regime.

## 5.4 Critical behaviour caused by diamagnetic effects

As indicated in the previous section, the electron tearing mode gets stabilised in the presence of a temperature gradient across the layer. In the first part of this chapter the full tearing mode is studied by applying finite temperature and density gradients. It has been shown analytically that the stabilisation of the full tearing mode must occur for a certain value  $L_n$  [49]. This analytical result has never been verified in an broad parameter space. Recent simulations obtained with gyrofluid models [44] were restricted to a few results in the high- $\Delta'$  regime missing an extended numerical proof of the analytical prediction [49].

For the present scope the medium- to high- $\Delta'$  regime is of interest employing mag-

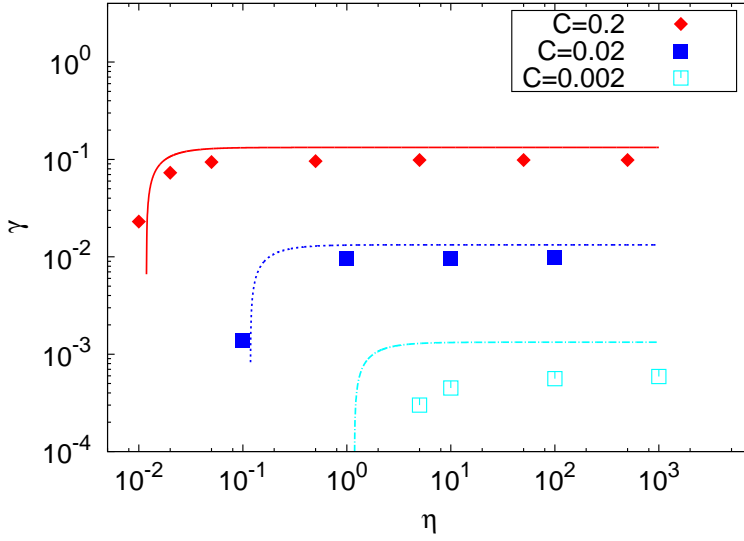


Figure 5.6: Growth rates depending on  $\eta$ . The critical behaviour of the growth rate has been measured for different  $C$  (full tearing mode case,  $a = 0.5$ ,  $k_y = 2\pi/10$ ). Results obtained with EUTERPE (points) are covered well by the analytic estimate Eq. (5.18) (lines).

netic configuration I setting  $\beta = 10^{-3}$  and  $a = 0.5$ . Each species is exposed to the same temperature and density gradients,  $\kappa_{T,e} = \kappa_{T,i} = \kappa_T$  and  $\kappa_{n,e} = \kappa_{n,i} = \kappa_n$ . Furthermore, it is defined  $\eta_s = \eta = L_n/L_T$ . For a good performance of the simulations  $N_p = 4 \cdot 10^6, \dots, 12 \cdot 10^6$  markers are sufficient, while resolving the simulation domain needs  $n_{\bar{s}} = 128$  radial points. The quasi-neutrality equation in the long wavelength approximation is employed with a fixed temperature ratio  $\tau = 1$ , whereas the exact density response of the gyrocenters was taken into account. The first simulations are carried out measuring the growth rates by varying the density gradient  $\kappa_n$  with a fixed temperature gradient  $\kappa_T = -0.005$ . Additionally, the simulations cover various strengths of the perpendicular magnetic field,  $C = 0.2, 0.02, 0.002$ . In Figure 5.6 (points) the growth rates obtained with EUTERPE are depicted.

Fixing any value of the shear strength  $C$ , and large values of  $\eta$  ( $\eta \gg 1$ ), a decrease of  $\eta$  does not influence the growth rate very much. Inspecting  $\gamma(\eta)$  related to  $C = 0.2$  (red points), the growth rate remains almost constant with respect to  $\eta$  when reducing  $\eta \approx 10^3$  by five orders of magnitude to  $\eta \approx 10^{-1}$ . In the vicinity of  $\eta \approx 10^{-2}$ , referred here to as the critical threshold  $\eta_{cr}$ , the growth rate drops suddenly. Below this threshold the tearing mode gets stabilised completely.

A complete stabilisation in cases of much smaller shear strengths  $C = 0.02, 0.002$  has been verified as well, shown in Figure 5.6 (blue and green points). In a low shear equilibrium,  $C \ll 1$ , or equivalently  $u_{0,e}/v_e \ll 1$ , the critical  $\eta$  reaches values close to unity. In this case the gradient scales vary on scales much larger than  $\rho_{s,e}$  getting more relevant for fusion applications.

For the set of parameters considered here analytical dispersion relations have been

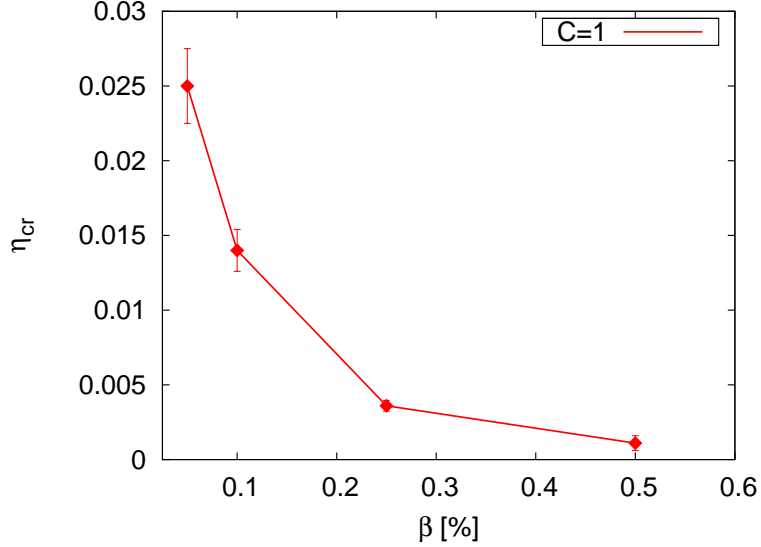


Figure 5.7: Critical  $\eta$  for various  $\beta$  for the electron tearing mode case ( $a = 0.5$ ,  $\kappa_T = -0.05$ ). For realistic  $\beta$ -values  $\mathcal{O}(1\%)$  the threshold  $\eta_{\text{cr}} = \mathcal{O}(10^{-4})$  is very small, thus the tearing mode is practically always unstable for realistic equilibrium gradients.

obtained in the presence of diamagnetic effects [44, 49]. They rely on a fluid description of the electrons combined with a gyrokinetic ion response including full FLR effects. In contrast to the quasi-neutrality equation used in EUTERPE the analytic prediction uses a Padé-response of the ions. By experience and due to the results of Sec. 7.2 this difference matters because the growth rates obtained with both field equations can deviate from each other in the range  $\mathcal{O}(10\%)$ . To apply the prediction properly respecting the dependency on  $\tau$  its limit of vanishing temperature ratio of the ions is employed. Thus, the analytical prediction fitting for the parameters here reads (see Table 1.3, Sec. 1.4.2)<sup>1</sup>

$$\gamma^2 = \gamma_0^2 - \left( \frac{k_y \kappa_{T,e}}{2\eta} \right)^2, \quad \gamma_0 = \frac{k_y}{l_s \sqrt{\beta}} \left( \frac{2}{\pi \sqrt{\mu \beta}} \right)^{1/3}. \quad (5.18)$$

The case  $\eta \rightarrow \infty$  corresponds to a vanishing density gradient ( $\gamma = \gamma_0$ ). The comparison of the simulated growth rates with Eq. (5.18) is shown in Figure 5.6 (solid lines). Both results agree well over the whole range of  $\eta$  and for the values  $C = 0.2, 0.02$ . In the case  $C = 2 \cdot 10^{-3}$  the prediction deviates up to 50% from the simulation results in the range  $\eta = \mathcal{O}(10^2)$ . Note that the validity of Eq. (5.18) reaches its limit for the parameters chosen here. Though this equation is valid for  $d_e < \rho_{S,e}$  it requires  $\rho_{S,e} < a$ , which matches here not completely ( $a = \mathcal{O}(\rho_{S,e})$ ). Small deviations of the growth rates occur when comparing the analytical result and the results obtained with EUTERPE, especially close to the critical  $\eta$ . This can be traced back to the high computational efforts which are necessary to resolve

<sup>1</sup>Note that the prediction here is subject to EUTERPE units.

small  $\gamma$ . If the growth rate becomes very small, the inaccuracy becomes larger in contrast to the values  $\gamma \approx \gamma_0$ . The computations become challenging for very low shear strengths  $C = 2 \cdot 10^{-3}$  and require relatively long simulation times even in a slab. For the runs with a shear strength of  $C = 2 \cdot 10^{-3}$ , the computations needed approximately  $3 \cdot 10^4$  CPUh for each point.

The threshold  $\eta_{\text{cr}}$  is of special interest, because it marks the value at which reconnection is prevented. Subsequently, this threshold is exposed to investigations using the electron tearing mode model. Maintaining the previous simulation conditions, but for  $\kappa_{\text{T}} = -0.05$ , the dependency of  $\eta_{\text{cr}}$  on the plasma- $\beta$  is examined within the electron tearing mode case. In Figure 5.7 the relation  $\eta_{\text{cr}}(\beta)$  is depicted for a single value  $C = 1$ . The critical threshold  $\eta_{\text{cr}}$  decreases strongly with higher  $\beta$ . For realistic  $\beta$ -values of the order  $\mathcal{O}(1\%)$  the tearing mode is always unstable for the parameters under consideration here. Indeed, if a small temperature gradient  $\kappa_{\text{T},e} = \mathcal{O}(10^{-2})$  is present, only a relatively large density gradient  $\kappa_{\text{n},e} = \mathcal{O}(10^1)$  or higher prevents the reconnection process. The absolute error bars of  $\eta_{\text{cr}}$  increase with higher values. However, the ratio of error to measured value remains the same for all points. A scaling of the critical  $\eta_{\text{cr}}(\beta)$  can be derived from Ref. [44, 49], evaluating Eq. (5.18) at the critical threshold  $\gamma = 0$ ,

$$\begin{aligned} 0 &= \gamma_0^2 - \left( \frac{k_y \kappa_{\text{T}}}{2\eta_{\text{cr}}} \right)^2 \\ &= \frac{k_y}{l_s \sqrt{\beta}} \left( \frac{2}{\pi \sqrt{\beta \mu}} \right)^{1/3} - \left( \frac{k_y \kappa_{\text{T}}}{2\eta_{\text{cr}}} \right)^2 \end{aligned} \quad (5.19)$$

From Eq. (5.19) the proportionality  $\eta_{\text{cr}} \sim 1/\beta^{1/3}$  ( $l_s \sim 1/\beta$ ) follows and supports qualitatively the decreasing of  $\eta_{\text{cr}}$  with higher  $\beta$ -values obtained with EUTERPE (Figure 5.7). Note that the increase of  $\beta$  according to Figure 5.7 changes the ratio  $d_e/\rho_{\text{S},e} = 1/\sqrt{\mu\beta}$  in the range  $1.0, \dots, 0.3$ . Therefore, the scaling derived from the dispersion relation Eq. (5.18) applies correctly only in the higher  $\beta$ -regime ( $\beta = \mathcal{O}(1\%)$ ) when  $d_e < \rho_{\text{S},e}$  and requires more simulation results for this case. The scaling  $\eta_{\text{cr}}(C)$ , indirectly shown in Figure 5.6, can be estimated using Eq. (5.19). Recalling that  $l_s \sim 1/C$ , the scaling  $\eta_{\text{cr}} \sim 1/C$  can be deduced which covers well the decrease of  $\eta_{\text{cr}}$  with larger shear strength.

The kinetic approach of Ref. [54] predicts the stabilisation of the tearing mode in the presence of diamagnetic effects as well. The gyrokinetic equation used in this work can be mapped to the gyrokinetic model here as well as the similar magnetic equilibrium. The prediction states  $\eta_{\text{cr}} \sim 1/\beta^{1/2}$ , if  $\Delta'a$  is of order unity covering qualitatively the findings of the simulations (Figure 5.7).

The kinetic approach proposed by Drake [18] in the presence of equilibrium gradients primarily does not predict a critical threshold. A reason might be the medium- $\Delta'$  value that allows the mode to get stabilised for sufficient large gradients.



# 6 Nonlinear simulations of tearing modes

Nonlinear simulations of tearing modes are a challenging numerical task in every geometry, thus even in a slab. From the numerical point of view nonlinear simulations are important for at least two reasons: the numerical simulation of the nonlinear saturation over large periods will finally demonstrate that EUTERPE can handle the subject of reconnection. Secondly, a good numerical performance of the single-mode simulations serves as a good starting point for investigations regarding mode-coupling, three-dimensional reconnection and further nonlinear electromagnetic modes in toroidal geometries.

The saturation of the collisionless tearing mode in the range  $\Delta'd_e < 1$  is known as Rutherford-like or “sub-exponential” behaviour. This type of nonlinear stabilisation is accompanied by the observation that the actual growth rate  $\gamma(t)$  does not exceed the linear growth rate  $\gamma_k$  for all times ( $\gamma(t) \leq \gamma_k$ ) [34].

The nonlinear acceleration of the field amplitude is known as “super-exponential” reconnection <sup>1</sup>, mainly investigated in high- $\Delta'$  scenarios <sup>2</sup>. This type of nonlinear destabilisation is characterised by an instantaneous growth rate  $\gamma(t) > \gamma_k$  when entering the nonlinear phase. The simulations presented here are the first results obtained with PIC methods at all. The numerical effort describing this non-saturation is dramatically higher compared to the Rutherford-like type, since an extremely small current channel evolves and collapses during a very short time interval. Both types of nonlinear behaviour are still far apart from a comprehensive physical understanding which motivates further simulations.

---

<sup>1</sup> The terms super-exponential, quasi-explosive, impulsive and faster-than-exponential arise often in this context describing the same strong increase of the reconnected flux in time. Further similar notations occur in similarity solutions of extended MHD models [13]. Although not comparable directly to the reconnection process here, the amplitudes  $A$  also grow “explosive” when approaching a certain time  $t_1$ : an algebraic term becomes significant in the early nonlinear regime,  $A \sim \exp(\gamma_k t)/(t_1 - t)$ .

<sup>2</sup> The roughly given threshold  $\Delta'd_e \approx 1$  which divides both nonlinear phases is obtained by experience with numerical simulations. It has never been proven strictly that it is a general sufficient condition for observing the super-exponential phase.

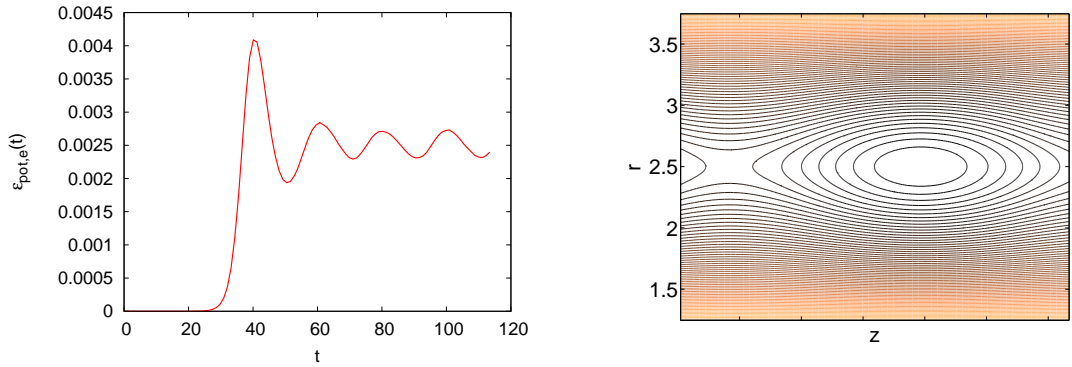


Figure 6.1: Left: The nonlinear evolution of the field energy while saturation ( $a = 0.6$ ). A clear saturation phase is reproduced. Right: Isocontours of the full vector potential  $A_0(r) + A(r, z, t = 113)$  showing the structure of the magnetic island close to the singular layer  $x = L_x/2 = 2.5$ .

## 6.1 Simulations of nonlinear saturated reconnection

For the subsequent outline magnetic configuration I has been chosen and a domain size  $L_x \times L_y = 2.5 \times 2\pi$ . The domain extension is resolved with up to  $n_{\bar{s}} \times n_{\chi} = 768 \times 16$  in the  $x, y$ -direction. To compare with the simulation results of Ref. [26], the plasma- $\beta$  is chosen to be  $\beta = 10^{-3}$ , not at least because the width of the perturbed current channel increases when reducing  $\beta$  and can be easier resolved numerically. The electron tearing mode model is used, but additionally the ions contribute to the dynamics, although they are not expected to play a dominant role. About  $5, \dots, 20 \cdot 10^6$  markers for each species have been used to obtain a good computational performance. The nonlinear mode-coupling between the  $m = 1$  mode, higher harmonics ( $m = 2, \dots, m_{\max}$ ) and the  $(m, n) = (0, 0)$  mode might essentially influence the simulations. For the parameters under investigation, various filter sizes  $m_{\max} = 2, \dots, 7$  with  $n = 0$  have been employed to check effects of mode-coupling including possibly damped tearing modes with  $\Delta' < 0$ . In all cases it has been verified that the  $m = 1$  mode dominates completely. This is important, because later on the results will be compared with analytical estimations relying on a single-mode model.

A typical nonlinear saturation of the tearing mode is depicted in Figure 6.1 (left) showing  $\epsilon_{\text{pot},e}(t)$  for  $a = 0.6$ . After the initial linear phase  $t \lesssim 20$ , the amplitude of the mode is large enough to alter the particle orbits and allowing the electrons to follow the island structure. In the clearly saturated period ( $t > 40$ ) a typical oscillation frequency of the electron field energy is observed accompanied by a periodic oscillation of the field amplitude at each spatial location. It has been proven clearly with EUTERPE that the saturation persists for all times  $t = \mathcal{O}(10^2 \cdot \gamma_k^{-1})$ . The numerical proof of the saturation and standing oscillations is important to validate the code. Moreover, EUTERPE provides a credible energy conservation of  $\Delta\epsilon(t) \lesssim 5\%$  for all nonlinear simulations discussed in this chapter.

The spatial structure of the magnetic island at a fixed time  $t = 113$  is shown in Figure 6.1 (right). The full parallel vector potential consisting of the equilibrium background  $A_0$  and the perturbation  $A$  has been plotted in the vicinity of the layer  $x \approx L_x/2$ . The structure of the magnetic island can be clearly resolved.

The estimation of the island half width  $w(t)$  in the constant- $\Psi$  regime was discussed in Eq. (1.25) (Sec. 1.4.3). If the constant- $\Psi$  approximation can not be applied, the shape and width of the separatrix can be obtained only numerically. Setting the  $X$ -point at  $(z = 2\pi/k_y, r = 0)$  without constraints of generality, the separatrix is the set of points  $(r, z)$  at each time  $t$  which obeys the condition

$$A\left(z = \frac{2\pi}{k_y}, r = 0, t\right) = A_0(r = w(t)) + A\left(z = \frac{\pi}{k_y}, r = w(t), t\right). \quad (6.1)$$

The island half width can be obtained by starting at the  $X$ -point and following the isocontour of the full vector potential. The maximum elongation with respect to  $r$  is reached at  $(z = \pi/k_y, r = w(t))$ .

Eq. (6.1) presumes that the  $X$ -point is fixed at each time step which is not necessarily the case in the simulations. In the beginning of the simulations the mode can drift in the poloidal direction because of computational reasons, although no equilibrium gradients are applied. After the mode has prospered well in the linear phase the mode structure remains fixed during simulations. To solve Eq. (6.1) for  $w(t)$  a MATLAB routine has been written using the field structure  $A(r, t)$  extracted from EUTERPE. Since the vector potential is given on a discrete spatial grid and no additional interpolation routine is used, the solution of Eq. (6.1) will result in a step-like function  $w(t)$ . Additionally, the island half width obtained with the constant- $\Psi$  approximation is also computed measuring the vector potential at the  $O$ -point.

To compare the simulated island half width with analytical predictions the time dependency of  $w(t)$  is removed by defining the temporal mean value  $w = \langle w(t) \rangle_T$  over a large time period  $T \gtrsim \gamma_k^{-1}$ .

The temporal evolution of  $w(t)$  with the simulation parameter  $a = 0.5$  is depicted in Figure 6.2. The solution of Eq. (6.1) in this case,  $w \approx 0.6$ , the scaled field energy  $\epsilon_{\text{pot,e}}(t)$  and a simulation result of Wan ( $w = 0.59$ ) [26] is compared. Wan estimated  $w \approx 0.6$  using the model of Drake [19] which will be discussed later. All values of  $w$  agree very well with each other, but are not very meaningful to proof Drake's prediction. Only an extended parameter study could reveal the reliability of this model.

Filling this gap of nonlinear gyrokinetic simulation studies in low- $\beta$  scenarios, the island half width  $w$  depending on  $a$  has been investigated. The equilibrium current width was varied  $a = 0.1, \dots, 0.75$ . This variation of  $a$  is rather unusual in the sense of the discussion in Sec. 5.2, because it leads to a possible configuration with  $0.1 \approx a < d_e \approx 0.7$ .

In Figure 6.3 the island half width  $w$  depending on the linear growth rate  $\gamma$  (red points) is depicted. Here  $w$  was obtained by solving Eq. (6.1). The constant- $\Psi$  approximation was checked as well by solving Eq. (1.25) for  $w(\gamma)$ . The results from both methods agree with each other better than 5%. The analytical finding by

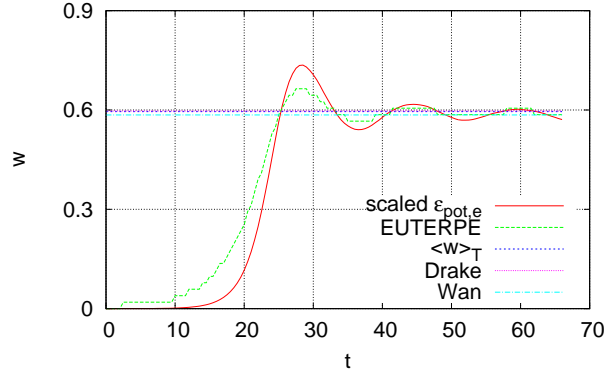


Figure 6.2: The temporal evolution  $w(t)$  and  $\epsilon_{\text{pot},e}(t)$  for  $a = 0.5$ ,  $L_x = 2.5$ . The island half width  $w = \langle w(t) \rangle_T$  obtained with EUTERPE is compared with the prediction of Drake [19] and the one simulation result of Wan [26].

Drake gives a relation  $w \sim \Delta'$ . When  $\Delta' d_e < 1$ , the dispersion relation Eq. (5.17) can be applied stating essentially  $\Delta' \sim \gamma$ . Therefore, it has been chosen to represent the saturated island half width  $w$  depending on the growth rate which emphasises the dependence of  $w$  on the most important linear quantity  $\gamma$ . The linear dispersion relation obtained with the shooting method  $\gamma(k_y a)$  is shown in Figure 6.4 to relate  $w$  with the exact solution of the linear eigenvalue problem. In the small- $\Delta'$  range, which corresponds to  $k_y a \gtrsim 0.75$  in Figure 6.4, the island half widths  $w \lesssim 0.1$  are small compared to the collisionless skin depth. The term small (or skin-size) islands refers to the relation  $w \ll d_e$  [75] and is covered well, since  $w \ll d_e \approx 0.7 \approx a = 0.75$ . Decreasing the equilibrium width to approximately  $a \approx 0.5$  ( $k_y a \approx 0.5$ ), the growth rate becomes larger ( $\gamma \approx 0.4$ ). In this range the island half width increases linearly with the growth rate up to values of  $w \approx 0.5$ .

The single simulation result of Wan ( $w = 0.59$ ) is shown as well (blue point) and fits well with the result of EUTERPE. At this point the magnetic island becomes as large as the equilibrium current width  $a$ . The islands are called large-sized if they extend as far as the “macroscopic” region  $a$ . This term does not fit very well here, since additionally it is  $a \ll d_e$ . In most of reconnection simulations  $d_e \ll a$  holds, and if  $w \approx a$  the term could be applied adequately. When  $a \approx 0.3$  ( $k_y a \approx 0.3$ ) the growth rate reaches the maximum value  $\gamma = 0.57$  and the island width as well,  $w \approx 0.7$  (Figure 6.3). The island widths becomes smaller when decreasing  $a$  further and a “curl” appears. This range is not supposed to be a reasonable reconnection scenario compared with the assumptions of Drake’s theory and the prediction must fail. If  $a$  reaches the lowest value  $a < 0.1$  ( $k_y a < 0.1$ ), the island half width exceeds clearly this equilibrium scale,  $0.1 \approx a < w \approx 0.4$ . Here also finite size effects play a role, since  $w \approx 0.7 \approx L_x/2 = 1.25$ .

The simulation results of  $w$  are discussed in terms of Drake’s prediction: in this

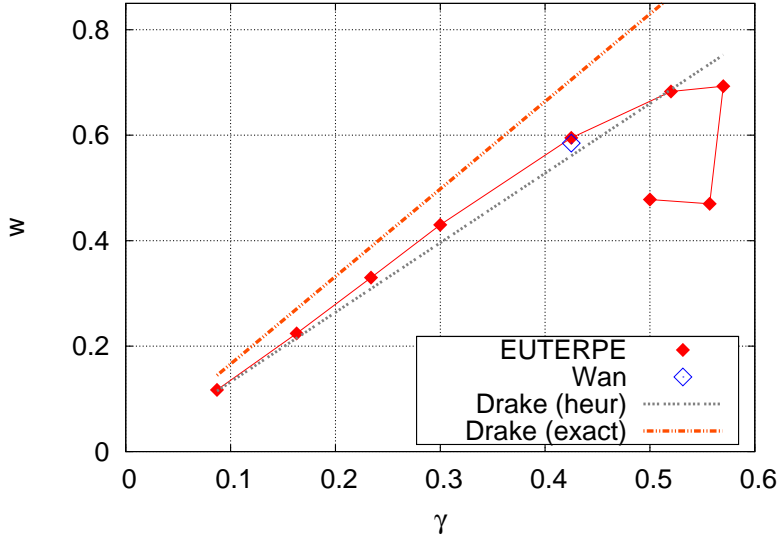


Figure 6.3: Comparison between the saturated island  $w(\gamma)$  obtained with EUTERPE, analytical theory (Drake) and Wan [26] (The red solid line connects simulations results). In the low- $\Delta'$  regime ( $\gamma \lesssim 0.4$ ) Drake's prediction is proved.

model electrons dominate the reconnection process while the electrostatic potential has been neglected. Under these conditions the saturated island half width is given by

$$w = \Delta' \frac{d_e^2}{2G}, \quad (6.2)$$

with an estimated constant  $G = 0.41$ .

As pointed out in Sec. 5.2, there are two similar kinetic dispersion relations derived in the small- $\Delta'$  regime, Eqs. (5.17). Using simple scaling arguments one can estimate a heuristic dispersion relation, which deviates from the exact derived dispersion relation by prefactors. The Eqs. (5.17) can be combined with Eq. (6.2) obtaining

$$w = \gamma \frac{\sqrt{\pi}^l l_s}{k_y v_e G}. \quad (6.3)$$

Inspecting Figure 6.3 (dashed lines), the case  $l = 0$  corresponds to the heuristic derivation (heur) and  $l = 1$  to the analytic results (exact).

Drake's theory is strictly valid only in the small- $\Delta'$  regime which refers here to values  $k_y a \gtrsim 0.75$  ( $w \lesssim 0.1$ , Figure 6.3). Decreasing the equilibrium current width to values  $a \approx 0.5$ , the island width increases linearly, as predicted by Drake. This marks the threshold validity of the theory. A further decrease of the equilibrium scale  $a$  gives the estimation  $0.1 \approx a < w \approx 0.4$ , in which the island width is comparable to the simulation size  $L_x$ . The island width saturates with respect to  $\gamma$  and drops

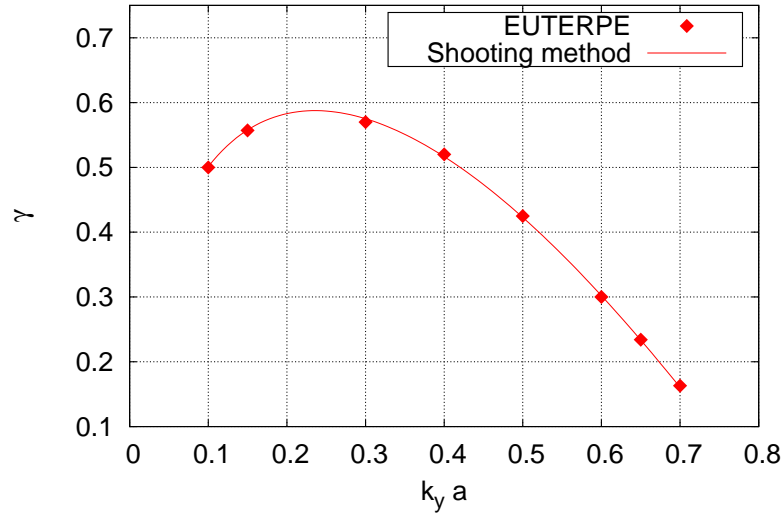


Figure 6.4: Linear dispersion relation  $\gamma(k_y a)$  depending on  $a$  ( $k_y = 1$ ) obtained with EUTERPE (points) and the shooting method (solid line). The relation  $\gamma(a)$  is used to support the discussion of Figure 6.3.

when reducing  $a$ .

Wan compared his result  $w = 0.59$  (Figure 6.2) with the analytic prediction, Eq. (6.3) ( $l = 0$ ), but properly speaking, Drake's model is not suited for this parameter configuration. Despite that, Eq. (6.3) confines the simulation results for both values  $l = 0, 1$  and gives a reasonable prediction if the growth rates are sufficiently small. The physical mechanism of the saturation in the nonlinear regime is still under discussion. Drake suggests that electrons interact with the mode via resonance effects in phase space. This can not be the final answer, because it will be shown later that fluid simulations reproduce similar island half widths compared with the gyrokinetic model in the low- $\Delta'$  regime.

## 6.2 Simulations of nonlinear super-exponential reconnection

In the following the essential difference of both nonlinear phases as well as the phenomenology will be discussed. A parameter study is performed which connects both phases. Additionally, there are a couple of results in literature which are badly compared to each other. Therefore, in the last section an extended parameter study is presented relating several simulation results presented in literature.

The full tearing model is used throughout this chapter excluding FLR effects by using the drift kinetic limit ( $\tau \ll 1$ ). In the quasi-neutrality equation the gyroaveraging operator acting on the ions is included while the polarisation density is sub-

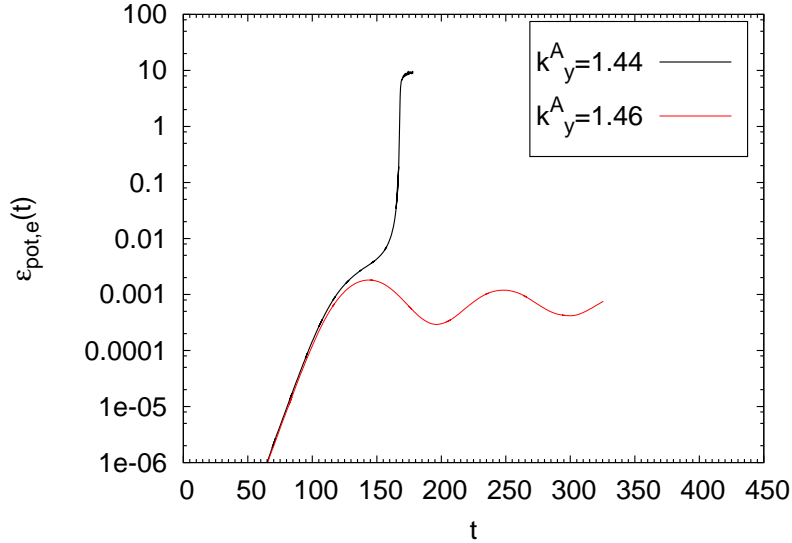


Figure 6.5: Electron field energy over time. Phenomenological difference between a mode with super-exponential growth ( $k_y^A = 1.44$ ) and a saturated mode ( $k_y^A = 1.46$ ). In the case  $k_y^A = 1.44$  the short saturation period at  $t \approx 175$  is not physical, but plotted for completeness.

ject to the long wavelength approximation. The results obtained with EUTERPE are compared with simulation results from (reduced) gyrofluid models subject to magnetic equilibrium II [21, 22]. For simplifying a direct comparison to those investigations and parameter values the quantities are expressed in Alfvén units if necessary. The superscript 'A' refers to Alfvén normalisation while quantities in the EUTERPE normalisation stay unmarked.

### 6.2.1 Phenomenology and first numerical simulations

The phenomenology of nonlinear destabilisation is outlined employing magnetic configuration II. A Fourier filter extracted the  $m = 1$  mode after proving numerically that this does not lead to an essential restriction regarding mode-coupling. In most of the simulations discussed in this chapter the particles are pushed using a newly implemented Fehlberg time integrator. It will be outlined later that this method is a helpful numerical tool for the simulations presented here.

A summary of the selected parameters are listed in Table 6.1 for both unit systems. The resolution of the spatial scales is very important and numerically demanding. In the first simulations presented here, a resolution of  $n_{\bar{s}} \times n_{\chi} = 18470 \times 40$  points has been used with one bin in the  $\bar{\phi}$ -direction to simulate a real two-dimensional mode. Otherwise at least eight points in the toroidal direction must be taken into account increasing the extension of the solver matrix unnecessarily. The subsequent super-exponential reconnection studies needed 512,  $\dots$ , 4096 cores per run.

In Figure 6.5 simulation results are depicted showing the electron field energy over

	EUTERPE units	Alfvén units
domain size in $x$	$L_x = 20.94$	$L_x^A = 2\pi$
magnetic equilibrium scale	$a = 3.33$	$a^A = 1$
ion sound Larmor radius	$\rho_{S,e} = 1$	$\rho_{S,e}^A = 0.3$
electron skin depth	$d_e = 0.33$	$d_e^A = 0.1$
wave vector varied	$k_y$	$k_y^A = k_y/\rho_{S,e}^A$

Table 6.1: Selected parameter values for the simulations represented in both unit systems. The values are equivalent to a constant plasma- $\beta$  of  $4.91 \cdot 10^{-3}$ .

time for two values of the wave vector  $k_y^A = 1.44, 1.46$ . In the case  $k_y^A = 1.46$  the nonlinear phase starts at  $t \gtrsim 100$ . The field energy (red curve) as well as the mode amplitude saturated showing the oscillating behaviour. The energy conservation proved clearly, since  $\Delta\epsilon \lesssim 1\%$  during simulation.

For the wave number  $k_y^A = 1.44$  the mode also tries to enter the saturated state shortly until  $t \approx 125$  (black curve). However, a subsequent saturation phase can not be observed by inspecting the field energy which increases rapidly as well as the mode amplitude. At  $t \approx 175$  the field energy seems to saturate but this can not be clearly proven numerically as will be discussed below. It is this super-exponential behaviour  $\gamma(t) \gg \gamma_k$  which characterises the phenomenon and the non-saturation. The calculations break down indicated by, for instance, the violation of energy conservation for  $t \gtrsim 170$  ( $\Delta\epsilon = \mathcal{O}(1)$ ).

The high spatial resolution in  $x$ -direction is necessary, since for example in the case of a spatial grid with fewer points ( $n_{\bar{s}} \times n_{\chi} = 6 \cdot 10^3 \times 40$ ) the electron field energy would not reach the “numerically saturated” curve shown in Figure 6.5 (black). The explosive phase would appear earlier motivating an increase of the grid resolution and number of markers. Also, if the conservation of energy can no longer be improved, the “final” set of numerical parameters is reached.

It is important to note that these simulations are always linked with a loss of particles in the momentum space. After the initial accelerate phase the electrons exceed the  $\kappa_v$ -sphere independent of its size. The simulation breaks down for  $t \gtrsim 170$  because  $\Delta\epsilon$  gets large and the electrons get lost. The loss of particles through the momentum sphere per time step, the actual growth rate and energy diagnostic are depicted in Figure 6.6. The particle loss was always observed in super-exponential simulations and was investigated for several runs. The radius of the momentum space  $\kappa_{v,s}$  was tuned using values  $\kappa_v = 4, \dots, 17$  with a corresponding increase of the numbers of markers,  $N_p = 20 \cdot 10^6, \dots, 120 \cdot 10^6$ . These manipulations do not affect the simulations at all hinting a physical drive which accelerates the particles to super thermal energies. For  $k_y^A \ll 1.44$  ( $\Delta'd_e \gg 1$ ) the summarised loss of electrons becomes of the order  $\mathcal{O}(N_p)$  which is a serious problem for the simulations as well as the comparison with analytic models.

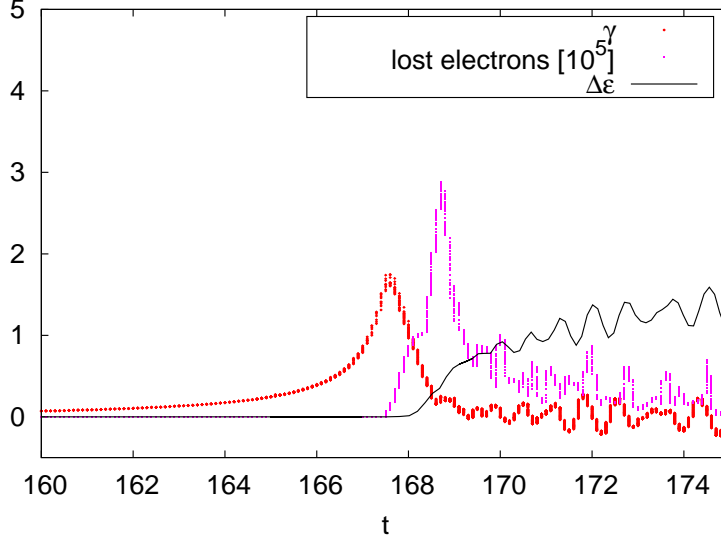


Figure 6.6: Diagnostics to characterise the nonlinear stage for  $k_y^A = 1.44$ . Actual growth rate  $\gamma(t)$ , numbers of electrons exceeding the momentum sphere and violation of the energy conservation  $\Delta\epsilon(t)$ .

It has been observed in previous related works that a thin current channel of width  $\mathcal{O}(d_e)$  evolves. During the evolution its width shrinks rapidly which is thought to be responsible for the extreme numerical effort of the simulations [23]. Figure 6.7 shows the spatial profile of the physical current  $j_{ph,\parallel,e}(\bar{s}) = j_{0,\parallel}(\bar{s}) + \delta j_{ph,\parallel,e}(\bar{s})$  at various time steps for the case  $k_y^A = 1.44$ , referring to the run discussed in Figure 6.5. The physical current  $j_{ph,\parallel,e}(\bar{s})$  was obtained by applying the transformation  $p_{\parallel}/m_s - q_s/m_s A \mapsto v_{\parallel}$  during marker binning. The current was binned via marker summation on discrete  $\bar{s}$ -values repeated for various poloidal positions  $\chi$  and is representative for all  $\chi$ -values. The noise on the current was smoothed for better visualisation: at a specific discrete lattice point  $\bar{s}_i$  of the current profile obtained by EUTERPE the mean value of the current including ten points,  $[\bar{s}_{i-5} \dots \bar{s}_{i+4}]$  has been calculated. Inspecting Figure 6.7, up to the time  $t = 132.1$  the evolving current structure  $\delta j_{ph,\parallel,e}(\bar{s})$  (blue) is similar to the initial profile (green). Within the next short period  $\Delta t_{\text{coll}} \approx 20$  (collapse time), the current profile at the resonant layer  $\bar{s} = 0.5$  peaks very fast while the width of the current channel further decreases. The extend of the current channel is roughly given by the electron skin depth or  $\Delta \bar{s} \approx 0.02$ . Although the largest growth rate  $\gamma(t)$  is not reached (Figure 6.5), the current starts already to collapse. For  $t = 158.8$  a reasonable current profile can be resolved just in time, although the diagnostic quantities depicted in Figure 6.6 do not hint a crash of the simulations for the following period  $t = 160, \dots, 167$ . Previous simulations of fluid models have found similar current spikes as depicted in Figure 6.7 of both the unphysical [23] and physical current density [36]. Although the adaptive Fehlberg integrator reduced the time step  $\Delta t = 0.05, \dots, 1.5 \cdot 10^{-3}$  a saturation after the collapse of the current profile could not be achieved. The

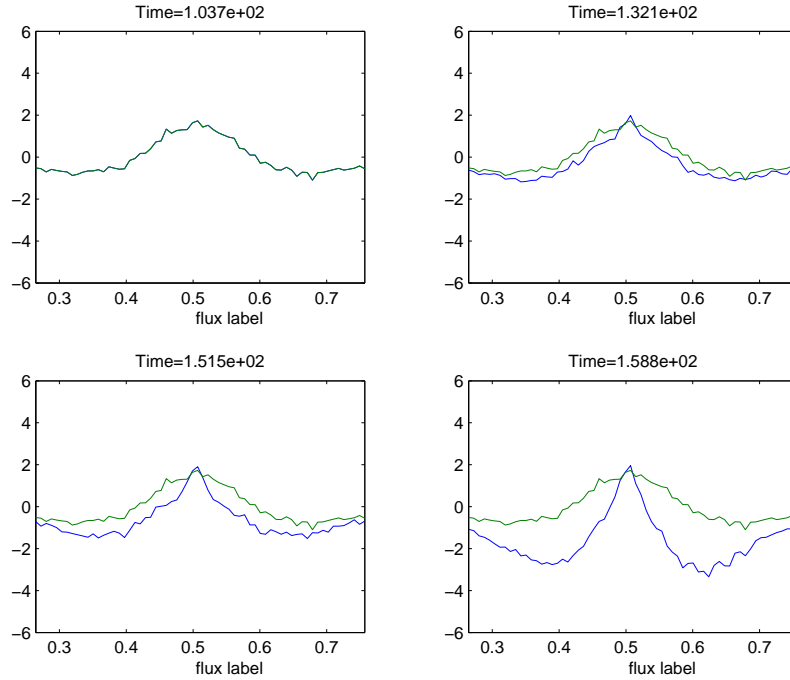


Figure 6.7: Temporal evolution of the physical current profile  $j_{ph,\parallel,e}(\bar{s})$  (blue) for  $k_y^A = 1.44$ . The perturbed current  $\delta j_{ph,\parallel,e}$  is multiplied by a factor of five. The initial current profile is shown for comparison (green).

tremendously short collapse period makes it hard to obtain reasonable simulation results.

For comparison the evolution of the smoothed current profile related to  $k_y^A = 1.46$  is shown in Figure 6.8. In the saturated mode case the evolving current profile (blue) does not show peaked current profiles from  $t = 101.3, \dots, 154.7$  compared with the initial profile (green).

In the analytical work of Refs. [23, 76] a differential equation was derived describing the temporal evolution of the island width normalised to the electron skin depth  $\hat{w} = w/d_e$ . In this reference a minimal fluid model was investigated in the cold electron limit ( $\rho_{S,e}^A = 0$ , corresponding to  $1/a \rightarrow 0$  if  $T_{0,e} = \text{const.}$ ), thereby using a heuristic ansatz for a fixed flow pattern related to  $\phi$ . The authors of Ref. [36] extended the analysis to the case of hot electrons ( $\rho_{S,e}^A > 0$ ) which is more relevant for the cases considered here. Similar to [23], the evolution of  $\hat{w} = w / \left[ (d_e^A)^{1/3} (\rho_{S,e}^A)^{2/3} \right]$  is governed by the differential equation  $d^2\hat{w}/d\hat{t}^2 = \hat{w}/4 + c_J/4 \cdot \hat{w}^4$ . The time is normalised to the growth rate,  $\hat{t} = k_y^A \left[ (d_e^A)^{1/3} (\rho_{S,e}^A)^{2/3} \right] t$ . The constant  $c_J = \mathcal{O}(1)$  must be chosen after the simulations to match the time series  $\hat{w}(t)$ , thus an extended discussion of the solution  $\hat{w}(t)$  in comparison to simulations is fairly hard.

Recently, a generalisation of the MHD energy principle with a nonlinear displacement map was applied to the two-fluid model of Ref. [23] describing the evolution of the mode amplitude in a more rigorous fashion [35]. However, this prediction

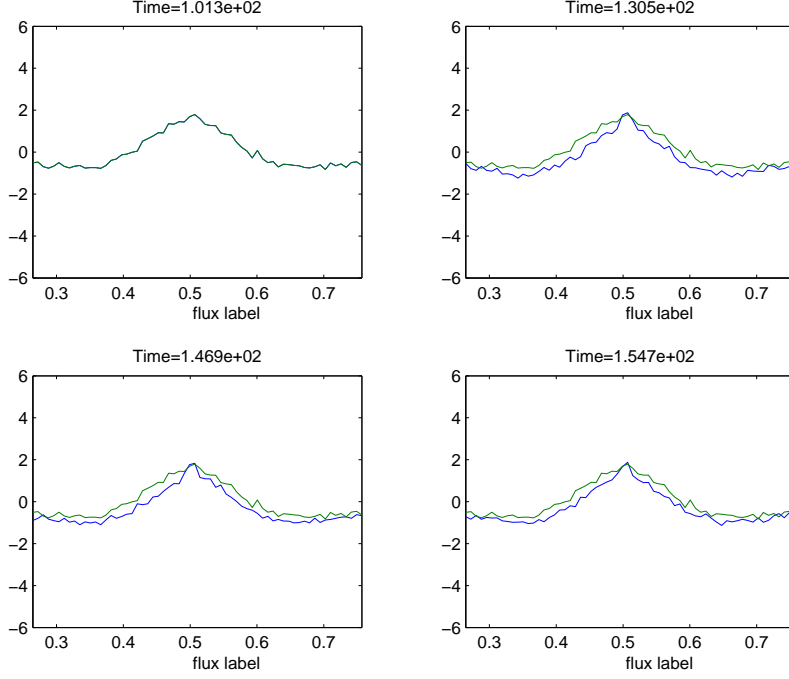


Figure 6.8: Temporal evolution of the current profile  $j_{ph,\parallel,e}(\bar{s})$  (blue) ( $k_y^A = 1.46$ ). The perturbed current  $\delta j_{ph,\parallel,e}$  is multiplied by a factor of five. The initial current profile is shown for comparison (green) The current does not evolve a peaked profile since the mode saturates.

is also only valid in the cold electron limit and in the asymptotic limit  $k_y^A \rightarrow 0$ , thus  $k_y^A \ll 1.44$ . It is important to note that this analytic approach predicts also a substantial different island evolution compared to Ref. [23], namely  $d^2\hat{w}/d^2t \sim \hat{w}^2$ . Presently, in none of the time-series of for instance the electron field energy or amplitude evolution a typical physical time scale  $T \ll \Delta t_{\text{coll}}$  could be identified in the super-exponential phase similar to, for instance, the oscillation period in the saturated phase which would allow a much more compact characterisation of the process. Moreover, with the gyrokinetic simulations performed so far a physical saturation after the explosive growth has never been achieved in contrast to results of recent works which employ gyrofluid models [10, 34], although the same parameters have been adopted. Obviously, there is a substantial difference between the nonlinear gyrokinetic and nonlinear gyrofluid calculations which is an important point when comparing both models.

### 6.2.2 The transition between both nonlinear phases

As indicated in the previous section, a small variation of the wave vector  $k_y^A$  can change the character of the nonlinear phase completely. There certainly is a critical wave number  $k_{y,\text{cr}}^A$  between  $k_y^A = 1.44 < \dots < k_y^A = 1.46$ , where a transition occurs. This transition is very interesting, since a small change of the wave vector changes

the nonlinear character of the system completely. This has never been discussed before in the literature where only the extreme limits of  $\Delta'$  have been examined. For the subsequent investigations both kinds of magnetic equilibria are used. The high computational effort is evident by using up to 2048 cores for each run for roughly  $5 \cdot 10^5$  CPUh. A detailed listing of the setup scenarios is shown in Table 6.2.

magnetic equilibrium	EUTERPE units	Alfvén units
II	$L_x = 20.94$	$L_x^A = 2\pi$
	$a = 3.33$	$a^A = 1$
	$\rho_{S,e} = 1$	$\rho_{S,e}^A = 0.3$
	$d_e = 0.33$	$d_e^A = 0.1$
	wave vector varied	
I	$L_x = 157.08$	$L_x^A = 4\pi$
	$a$ varied	$a^A = 1$
	$\rho_{S,e} = 1$	$\rho_{S,e}^A$ varied
	$d_e = 1$	$d_e^A = 1$
	$k_y = 0.04$	$k_y^A = 0.5$

Table 6.2: Different setups for the simulations in both unit systems. The two different values of  $d_e$  result in two different values for the plasma- $\beta$ :  $4.91 \cdot 10^{-3}$  (II) and  $5.47 \cdot 10^{-4}$  (I).

It turned out that the oscillation frequency  $\omega_B$  of the field energy in the deeply nonlinear phase is supposed to be a good quantity to indicate the transition as long as the physical saturation can be proven clearly. The frequency  $\omega_B$  was obtained by calculating the mean value over several periods  $n_p$  of the field energy,  $\omega_B = 2\pi/[n_p(T_f - T_i)]$ ,  $T_i$ ,  $T_f$  being the initial and final time point of measurement. It is also possible to measure the island width, but one has to solve additionally the nonlinear Eq. (6.1).

First, magnetic equilibrium II is considered to extend the results of the previous chapter. The strategy is to characterise the transition by starting with a value  $k_y^A \approx 2$  in the well-behaved Rutherford-regime and reduce it slowly to  $k_{y,cr}^A$ , until the oscillation frequency changes strongly when crossing both regimes. Figure 6.9 shows the oscillation frequency versus the wave vector  $k_y^A$ . In the vicinity of marginal instability  $k_y^A \approx 2$ , a clear saturated and oscillating phase can be observed. Reducing the wave vector to values  $k_y^A \approx 1.5$ , the oscillation frequency increases ( $\Delta'd_e \approx 1$ ). Close to  $k_y^A \approx 1.45$  the frequency falls with smaller  $k_y^A$  approaching a critical wave vector  $k_{y,cr}^A$ . In Figure 6.9 this threshold is indicated by setting the oscillation frequency manually to zero ( $\omega_B = 0$ ). Due to the high sensitivity of the threshold a closer approach according to  $k_y^A = k_{y,cr}^A + \epsilon_k$  ( $0 < \epsilon_k \ll 1$ ) could not be achieved.

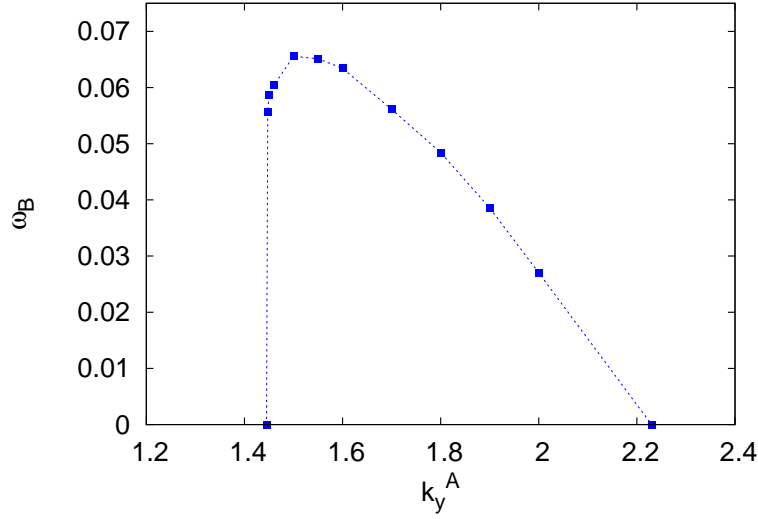


Figure 6.9: Oscillation frequency  $\omega_B$  depending on the wave vector  $k_y^A$ . The transition between saturated and super-exponential reconnection occurs at  $k_{y,\text{cr}}^A \approx 1.45$  (Equilibrium II).

The strongly reduced oscillation frequency indicates that the saturated phase becomes quasi-static compared to the linear growth rate in this range ( $\omega_B \ll \gamma_k = \mathcal{O}(0.1)$ ). A further decrease of  $k_y^A$  leads again to the super-exponential phase and no oscillation frequency can be assigned to the mode.

Simulations with a wave vector very close, but below the threshold  $k_y^A = k_{y,\text{cr}}^A - \epsilon_k$  ( $k_y^A = 1.4425, 1.445, \dots < k_{y,\text{cr}}^A$ ) require a very high resolution of the grid ( $n_{\bar{s}} = 1.85 \cdot 10^4$ ). For the value  $k_y^A = 1.4425$  the Fehlberg integrator allowed to achieve at least an energy conservation of  $\Delta\epsilon \lesssim 5\%$  which was not possible before with the Runge-Kutta scheme and marks a clear numerical improvement. The step size reduced to  $\Delta t = 0.05, \dots, 10^{-3}$  when the mode approaches the largest slope of the field energy. When using the adaptive time step integrator, the evaluation of the marker statistics similar to Figure 6.6 showed that the loss of electron markers could be reduced by three orders of magnitude. Despite that the current profile still undergoes a crash for  $k_y \lesssim k_{y,\text{cr}}$  the numerical enhancements may serve as a starting point for a closer inspection of the super-exponential behaviour at the critical threshold.

Similar simulations of the transition were performed using magnetic equilibrium I. The question arises whether this equilibrium might allow for the super-exponential growth, too. The parameter used here refer to similar simulation conditions of Ref. [21]. Instead of  $k_y^A$  the width of the equilibrium current  $a$  was varied.

Figure 6.10 shows the nonlinear oscillation frequency  $\omega_B(a)$  and the linear growth rate  $\gamma(a)$ . For relatively large  $a \gtrsim 16$  nonlinear saturation is observed. The growth rate  $\gamma$  is of the same order of magnitude as the oscillation frequency,  $\gamma \approx \omega_B$ , moreover, the shape of both curves suggests a linear relation  $\omega_B \sim \gamma$ . When reduc-

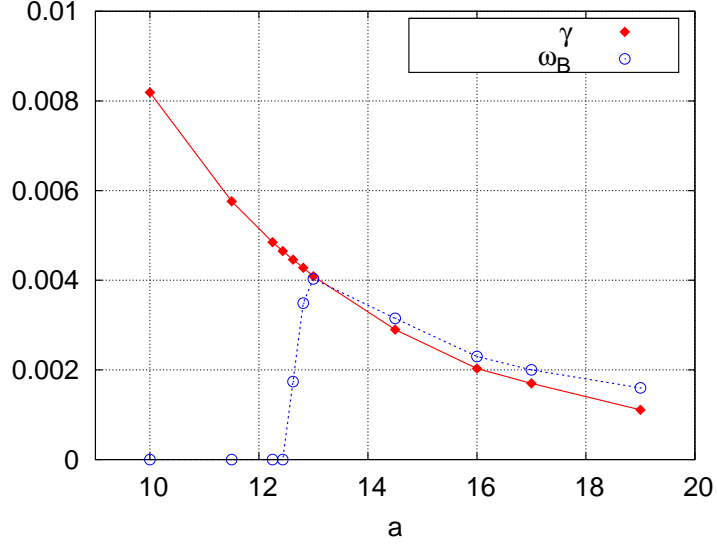


Figure 6.10:  $\omega_B$  and  $\gamma$  depending on  $a$  (configuration I). The transition of the nonlinear phase is proven to occur with configuration I at  $a_{\text{cr}} \approx 12.5$ . Below this value the oscillation frequency is set to zero.

ing  $a \lesssim 16$ , the oscillation frequency achieves a maximum at  $a \approx 13$  ( $\omega_B \approx 4 \cdot 10^{-3}$ ). A further decrease of  $a$  causes the oscillation frequency to fall and subsequently, a sharp transition occurs at  $a_{\text{cr}} \approx 12.5$ . The results show that slightly above the threshold  $a \gtrsim a_{\text{cr}}$  the saturated mode is quasi-static ( $\omega_B \ll \gamma$ ). For smaller values  $a < a_{\text{cr}}$  the oscillation frequency was set to zero manually, since during super-exponential growth an oscillation could not be assigned to the mode. These investigations prove that simulations with configuration I also reveal a critical threshold for nonlinear tearing modes. Recall that  $a = 1/\rho_{S,e}^A$  is changed, thus the threshold occurs at  $\rho_{S,e}^A \approx 0.08 \ll d_e^A = 1$ . It is an open issue how the ratio of these both quantities characterise the threshold.

Further simulations are necessary to quantify the saturated island width at critical  $a_{\text{cr}}$  and  $k_{\text{cr}}$ . Additionally, a detailed quantification of the plasma inflow pattern at the resonant layer might give further insight into the critical threshold. In Ref.[10] the nonlinear acceleration is investigated by means of a gyrofluid model. The accelerated phase is accompanied with larger  $\vec{E} \times \vec{B}$  flow velocities at the  $X$ -point than in the saturated phase. However, the simulation results obtained with the gyrofluid model could not be reproduced with EUTERPE, thus hinting a substantial difference in the models. The transition between both nonlinear phases shown for the oscillation frequencies here is very sharp. It would be helpful if equilibria and selected parameters were investigated allowing a “smoother” transition to improve the numerical control of the mode.

### 6.2.3 Extended parameter studies

An extensive parameter study is presented giving an overview of the critical threshold depending on the parameters  $L_x$ ,  $L_y$  and  $a$ . The simulation results of the previous chapter will be classified within this set of results obtained with configuration I as well.

Furthermore, the results in a broad parameter space are compared with available results in literature. In contrast to results obtained with EUTERPE concerning the super-exponential phase, it has been shown that a saturation mechanism and a well-defined conservation of the energy occur after the super-exponential phase for  $\tau \approx 1$  and  $\tau \ll 1$  [34, 51]. The fast-reconnection is known to be necessary for super-exponential growth, but counterexamples were found [34]. Recently, it was shown that a second acceleration can occur after the first explosive phase for  $\Delta' d_e > 1$  [10]. It is still unclear whether the physical model is significant in order to observe super-exponential growth or if there are universal parameter regions independent from the models.

To relate simulation results of the gyrokinetic model with previous investigations two parameter scans were performed in which either  $(a, L_x)$  is varied (scan (i)), or  $(a, L_y)$  (scan (ii)). Table 6.3 summarises the selected parameter regions. Due to the definition of the Alfvén units in the first scan (i)  $L_x^A$  is varied when  $\rho_{S,e}^A$  changes, and similarly in (ii)  $L_x^A$ , although  $L_x = 15$  remains a constant.

The fields were spatially resolved with up to  $n_{\bar{s}} \times n_{\chi} = 2 \cdot 10^4 \times 20$  points in

parameter scan	parameter values
(i)	$L_x, a$ varied ( $\mapsto d_e^A, \rho_{S,e}^A$ )
	$d_e = 1$
	$L_y = 157.08$ ( $k_y^A = 0.5$ )
(ii)	$L_x = 15, a$ varied ( $\mapsto d_e^A, \rho_{S,e}^A$ )
	$d_e = 1$
	$k_y = 2\pi/L_y$ varied

Table 6.3: Parameter values of the two scans (i), (ii). The plasma- $\beta$  is kept constant at  $5.47 \cdot 10^{-4}$ . Due to the different normalisations the values in brackets change as well.

$x, y$ -direction. This ensures a resolution of  $a, d_e$  with at least ten points. The time consuming computations are performed with up to 1024 cores and at most  $8 \cdot 10^7$  markers for each species needing roughly  $5 \cdot 10^5$  CPUh.

The parameter scans describe a binary decision whether a nonlinear saturation takes place or not. Figure 6.11 shows the results of parameter scan (i). The green area represents the complete domain of simulated pairs  $(a, L_x)$  with a resolution of about  $(\Delta a, \Delta L_x) = (0.1, 5)$ . This area is bounded from above by the linear

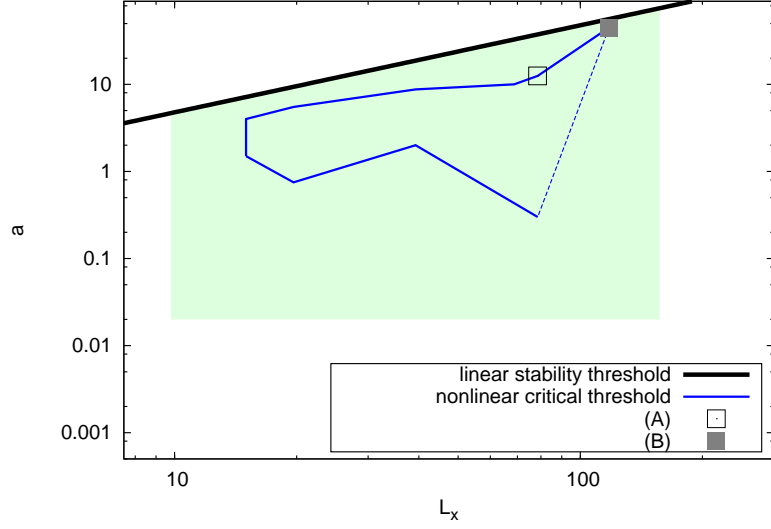


Figure 6.11: Parameter scan (i). The green shaded area covers the range of the parameters  $(a, L_x)$ . The inner of the polygon marks the super-exponential regime. The dotted line does not denote necessarily a transition from left to right, but closes only the polygon from (B) to the point with smallest  $a$ ,  $(0.3, 78.54)$ .

stability threshold above which the mode is linearly stable. The linear stability parameter was computed by solving  $\Delta'(L_x, L_y, a) = 0$  numerically at various points and interpolated (black solid line). Note that the  $m = 1$  mode is always selected. The green shaded area is bounded from below by the minimum value  $a = 2 \cdot 10^{-2}$ . The region can be just resolved using the computational means available (memory consumption of the solver matrix and number of markers).

Within the blue polygon the mode shows super-exponential growth. Point (A) marks the parameter values studied in the previous chapter,  $(a, L_x) = (12.5, 78.54)$  (It also refers to Ref. [21] at which  $\rho_{S,e}^A = d_e^A$ ). Starting at this point, a lowering of  $a$  with constant  $L_x$  maintains the super-exponential character of the mode. However, for small enough values  $a < 0.3$ , the study reveals a second critical threshold below which the mode becomes again nonlinearly stable. These values of  $a$  are equivalent to the relation  $\rho_{S,e}^A \gg d_e^A$ . Thus, in the large- $\Delta'$  range the saturation of the mode sets in again.

When  $L_x = 10, \dots, 80$ , the upper boundary of the polygon refers to the low- to medium- $\Delta'$  regime ( $\Delta' d_e \approx 1$ , if  $a \gtrsim 3$ ). In this range the nonlinear destabilisation of the mode has been verified when  $\Delta'$  is of order unity. If  $L_x$  is small enough in the regime  $L_x = \mathcal{O}(10)$ , both critical thresholds vanish and a Rutherford-like stabilisation was observed: a variation of the magnetic equilibrium scale can not excite the super-exponential growth in the range  $\mathcal{O}(10^{-2}) < \dots a \dots < \mathcal{O}(1)$ .

A special point (B) marks  $(a, L_x) \approx (45, 117)$ . It was shown that as the mode crosses the linear stability threshold its growth immediately experiences a super-

exponential acceleration. This is remarkable since at this point  $\Delta'd_e \approx 0$  is valid which contradicts the general regime of super-exponential acceleration. The point (B) can be compared with results of Ref. [34], where  $a$  was fixed but, enlarging the difficulty of a direct comparison, a deuterium plasma with an unnatural proton to electron ratio was considered. Additionally, the plasma- $\beta$  was varied within the range  $10^{-5}, \dots, 10^{-3}$ , resulting in different ratios  $d_e/\rho_{S,e}$  and maintaining the condition  $d_e = \mathcal{O}(1) \ll a = \mathcal{O}(10)$ . This reference, however, found a physical saturation after an explosive phase which could not be confirmed. In the simulations here, following point (B) to lower values of  $a$  ( $L_x = 117$ ), a second nonlinear stability threshold could not be verified within the green shaded area. Therefore, the polygon in Fig. 6.11 was closed with the dashed line.

A short overview of the parameter regime under investigation compared with significant references is provided by Table 6.4.

The parameter space is extended by varying  $L_y$ , when  $L_x = 15$  is fixed (scan (ii)).

	$\Delta'd_e < 1$	$\Delta'd_e > 1$
$\rho_{S,e}^A > d_e^A$	[34], Figure 6.11	[21], Figure 6.5
$\rho_{S,e}^A \approx d_e^A$	[34], Figure 6.11	[36], Figure 6.11
$\rho_{S,e}^A < d_e^A$	[34], Figure 6.11	[23, 36], Figure 6.9–6.11

Table 6.4: Summary of references investigating super-exponential reconnection and results obtained with EUTERPE.

This variation of parameters is motivated by the fact that in previous nonlinear simulations with the magnetic equilibrium I [26] it has never been observed with EUTERPE that the super-exponential behaviour occurs. The exploration provided by scan (ii) relates both the domain of parameters used in Sec. 5.1 and in scan (i). In Figure 6.12 the green shaded area marks the parameter regime which has been investigated to observe whether the nonlinear acceleration is excited or not. The blue area refers to the set of parameters  $(a, L_y)$  that allow for a nonlinear acceleration phase. Additionally, the threshold  $\Delta'd_e = 1$  (red solid line) is depicted as well as the linear stability threshold provided by solving the equation  $\Delta'(L_x, L_y, a) = 0$  (black solid line).

In Figure 6.12 the threshold defined by the condition  $\Delta'd_e = 1$  is valid in the domain  $L_y = 30, \dots, 100$  and  $a \approx 2$ . If the equilibrium current width  $a$  and  $L_y$  are small enough,  $(a, L_y) = (\mathcal{O}(1), \mathcal{O}(10))$ , the equilibrium values of the linear benchmark in Sec. 5.1 are covered approximately by  $(a, L_y) = (\mathcal{O}(1), 10)$  and  $\beta = 10^{-3}$ . A similar range of parameters is used in Ref. [26]. This parameter range does not support super-exponential behaviour of the nonlinear mode: the blue area contracts for small enough  $(a, L_y)$  showing that the nonlinear acceleration is inhibited. Even smaller values of  $a$  do not change this result, although  $\Delta'd_e \approx 1$ .

The simulations in the range  $L_y = 50, \dots, 200$  (or small enough  $k_y$ ) show that the critical threshold of nonlinear acceleration appears for two different values of  $a$ ,

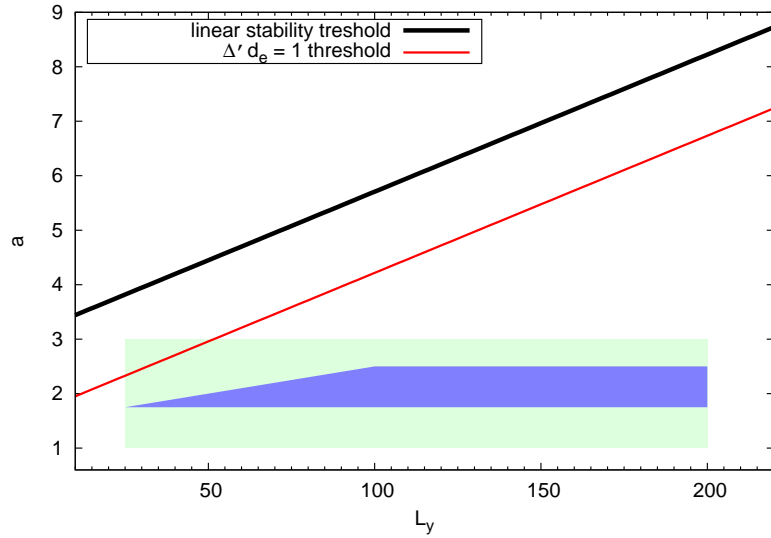


Figure 6.12: An extended parameter study showing the threshold of super-exponential reconnection.  $L_x = 15$  is fixed and  $L_y, a$  varied (Equilibrium I).

marking an upper and a lower critical threshold. The upper threshold remains constant, while the estimated condition  $\Delta' d_e = 1$  is clearly not valid.

The parameter scans (i), (ii) demonstrate clearly that the threshold  $\Delta' d_e \approx 1$ , widely used in nonlinear simulations using fluid models, does not necessarily mark the transition between both nonlinear phases. Due to substantial differences of the nonlinear simulations performed with the gyrokinetic model here and the fluid models of discussed references, the result of the parameter scans (i), (ii) probably do not hold universally independent of the model. An important finding is the second critical threshold of the equilibrium current width  $a$ , below which the super-exponential phase is inhibited and saturation sets in again.

# 7 Comparison of a compressible gyrofluid and gyrokinetic model

## 7.1 Introduction

Although much of the progress in the understanding of magnetic reconnection has been possible thanks to the use of fluid-based models, the results achieved with these models require independent confirmation when kinetic effects are expected to be important. Here, a compressible gyrofluid code that has been employed in Refs. [10, 51] to investigate ion gyro-orbit averaging effects on collisionless magnetic reconnection, is compared with the gyrokinetic equation <sup>1</sup>.

After a linear benchmark of the codes with a numerical eigenmode and eigenvalue analysis, the results of the two models in the linear regime are compared over the whole spectrum of linearly unstable wave numbers, both in the drift kinetic limit and for finite ion temperature. Nonlinearly, focusing on the small- $\Delta'$  regime, relevant observables as the evolution and saturation of the island half width and the oscillation frequency at saturation are compared <sup>2</sup>.

### 7.1.1 The compressible gyrofluid model

The gyrofluid model considered here has been adopted in Refs. [10, 51] to investigate magnetic reconnection in collisionless high-temperature plasmas with a strong guide field.

This model originates from a comprehensive gyrofluid model for both ions and electrons derived from the gyrokinetic equation by Snyder and Hammett [61]. The moments are obtained by applying velocity space integrals to the gyrokinetic equation with an unshifted Maxwellian. This model includes magnetic curvature effects, mirror terms, FLR and diamagnetic effects. The highest moments of the velocity integrals are subject to closure schemes related to three categories. It considers the inclusion of Landau damping, the closure of toroidal terms and mirror terms (trapped particles).

A simplified version of this model has been derived in Ref. [40] neglecting magnetic curvature effects and restricting it to two-dimensional dynamics. Furthermore, the

---

<sup>1</sup>The results of the comparison of both models developed from a collaboration with Luca Comisso and Daniela Grasso, members of “The Burning Plasma Research Group” at the Politecnico di Torino, Dipartimento di Energia. The simulation results of the gyrofluid model are provided by Luca Comisso.

<sup>2</sup>In this section all quantities have been normalised to Alfvén units.

reduced model truncates the moment hierarchy by taking only the first two velocity moments of the gyrokinetic equation for both the electrons and the ions (four-field model). The species temperature are taken to be constant while the electron Larmor radius has been neglected. Electron inertia terms were retained in order to break the frozen-in condition and allow for magnetic reconnection. Ion compressibility is adopted to investigate the influence of ion sound waves on reconnection [10]. Therefore, the evolution equations of the compressible gyrofluid model consist of the continuity equation and the  $z$ -component of the equation of motion for the ion gyrocenters,

$$\frac{\partial n_i}{\partial t} + [\langle \phi \rangle, n_i] = -[u_i, \langle A \rangle], \quad (7.1)$$

$$\frac{\partial D}{\partial t} + [\langle \phi \rangle, D] = \tau \rho_{S,e}^2 [\langle A \rangle, n_i], \quad (7.2)$$

and similar equations for the electrons,

$$\frac{\partial n_e}{\partial t} + [\phi, n_e] = -[u_e, A], \quad (7.3)$$

$$\frac{\partial F}{\partial t} + [\phi, F] = -\rho_{S,e}^2 [A, n_e]. \quad (7.4)$$

Here  $D = \langle A \rangle + d_i^2 u_i$  is proportional to the ion gyrocenter parallel canonical momentum, whereas  $F = A - d_e^2 u_e$  is proportional to the electron parallel canonical momentum. Furthermore,  $\langle \phi \rangle = \Gamma_0^{1/2} \phi$  is the gyro-averaged electrostatic potential and  $\langle A \rangle = \Gamma_0^{1/2} A$  is the gyro-averaged parallel magnetic potential, where the symbol  $\Gamma_0^{1/2}$  refers to the gyro-averaging operator that is adopted in its lowest-order Padé approximant form [37]

$$\Gamma_0^{1/2} = \frac{1}{1 - \frac{\rho_i^2}{2} \nabla_{\perp}^2}. \quad (7.5)$$

The system of equations is completed by the parallel component of Ampère's law,

$$\nabla_{\perp}^2 A = u_e - \Gamma_0^{1/2} u_i, \quad (7.6)$$

and by the quasi-neutrality condition

$$n_e = \Gamma_0^{1/2} n_i + \frac{\Gamma_0 - 1}{\rho_i^2} \phi. \quad (7.7)$$

The resulting model is dissipationless and suitable for the study of reconnection mediated by electron inertia. In particular, it possesses a noncanonical Hamiltonian structure [40] that reveals the presence of four Lagrangian invariants, which have proved to be helpful to understand how the reconnection evolution is affected by the plasma- $\beta$  and by the ratio of species temperatures [51].

This model has been subject to various simplifications in literature. By neglecting ion compressibility in Eq. (7.1) ( $[\langle \phi \rangle, n_i] = 0$ ), the equations cover the three-field

model of Ref. [44].

The electrons are mainly responsible for parallel and perpendicular dynamics so one can simplify the equations by neglecting the ion response. Then, Eq. (7.1) is not needed and the density and current of the ions do not contribute to the condition of quasi-neutrality, Eq. (7.7) and Ampère's law, Eq. (7.6). Employing additionally the constraint  $k_{\perp}\rho_i < 1$  on this reduced two-field model the quasi-neutrality Eq. (7.7) can be simplified to  $(1 - \rho_i^2 \nabla_{\perp}^2)n_e = \nabla_{\perp}^2 \phi$  [42, 77].

As shown in Sec. 5.1, the electrostatic fluctuation  $\phi$  can be interpreted as a small correcting quantity completing the electromagnetic description of the tearing mode. By neglecting  $\phi$  the quasi-neutrality can be discarded and the model includes only the evolution of the parallel current  $u_e$  and the density response  $n_e$  of the electrons. This minimal model has been used in Sec. 1.4 to derive the linear dispersion relation of the tearing mode.

### 7.1.2 Equilibrium configuration and numerical setup

To investigate spontaneous reconnection the model equations are solved numerically by employing magnetic configuration II in a two-dimensional slab geometry ( $\partial/\partial z = 0$ ). The parameter was chosen to be  $C = 0.1$  if not stated otherwise. This results in a maximal relative shear strength of  $B_{0,y}/B_{0,z} \approx 0.08$  in the domain and a shear length  $l_s = B_{0,z}/(dB_{0,y}/dx) = 5$  at the resonant surface  $x = 0$ .

The equilibrium magnetic field  $\vec{B}_0$  results from an equilibrium current  $u_{0,e}$  from electrons only as described in Sec. 4.2. Furthermore, the plasma is considered homogeneous with flat density  $n_s(x) = n_0$  and temperature profiles  $T_s(x) = T_s$  for each species. The simulation domain is characterised by  $\{(x, y) : -\pi \leq x \leq \pi, -\hat{a}\pi \leq y \leq \hat{a}\pi\}$ . The parameter  $\hat{a}$  fixes the domain length  $L_y$  in  $y$ -direction which is linked to the wave number  $k_y = 2\pi m/L_y$  of the longest wave length mode  $m = 1$  of the system. The tearing mode stability quantity  $\Delta'$  is then characterised by the wave vector  $k_y$  according to Eq. (4.6) (Sec. 4.2).

The gyrofluid code decomposes the fields into a time-independent background equilibrium and an evolving perturbation within a pseudospectral method [51, 78]. Periodic boundary conditions are employed in both the  $x$ - and  $y$ -directions, and a grid of  $1024 \times 128$  points has been used. Since periodic boundary conditions are imposed also along the  $x$ -direction, a Fourier series truncated to eleven modes is used to approximate the equilibrium magnetic field. Finally, an Adams-Bashforth algorithm is applied to push the fields in time and an initial disturbance on the out-of-plane current density of width  $\mathcal{O}(d_e)$  around the resonant surface is set to accelerate the onset of the tearing instability.

It is important to note that the boundary conditions for the fields with respect to the  $x$ -direction are different in both codes. Due to the numerical method underlying the gyrofluid code periodic boundary conditions arise naturally. The choice of the domain size in the  $x$ -direction is sufficient to avoid finite domain size effects on the value of the tearing stability parameter. However, in the following the effects on the boundary conditions will be checked by performing a detailed linear benchmark with the eigenvalue approach. If simulations in the drift kinetic limit were performed, this

was achieved by setting the temperature ratio to  $\tau = 1/900$ , giving  $\rho_i = 1/30 \ll d_e$ , which makes the effect of the gyroaveraging operators negligible. Additionally, instead of the Padé approximation the long wavelength approximation was then used for the quasi-neutrality equation in EUTERPE.

## 7.2 Linear comparison of the models

As a first step the accuracy of the codes is checked in the linear regime with a benchmark. For this purpose a numerical eigenmode and eigenvalue analysis is applied to each of the two models in the drift kinetic limit. After the accuracy of the codes has been proven to a high degree, a comparison of the models in both the drift kinetic limit and the case of finite Larmor radii follows.

### 7.2.1 Eigenvalue equations

In this section the procedure of performing a numerical benchmark is described using the shooting method explained in Sec. (5.2) to get the linear dispersion relations in the drift kinetic limit. An analysis of the eigenvalues and the eigenmode structure is given here for both the linearised gyrofluid and the gyrokinetic equations. The gyrofluid equations (7.1–7.4), and the gyrokinetic equation (2.5–2.9), are linearised using the ansatz  $\partial_t \mapsto -i\omega$  and  $\partial_y \mapsto ik_y$  for the perturbed quantities, additionally assuming a long wavelength approximation for the quasi-neutrality equation, Eq. (2.13). The field equations are cast into a general form with the coefficients  $q_j^i$ , with  $(i, j) = (A, \phi)$ ,

$$\frac{d^2\phi}{dx^2} = -q_\phi^\phi(x, \omega)\phi - q_A^\phi(x, \omega)A, \quad (7.8)$$

$$\frac{d^2A}{dx^2} = -q_\phi^A(x, \omega)\phi - q_A^A(x, \omega)A. \quad (7.9)$$

The linearisation of the gyrofluid system gives the following coefficients

$$q_\phi^\phi(x, \omega) = -k_y^2 + \sum_s q_s \frac{F'_{0,s}}{N_s} \frac{k_y}{\omega}, \quad (7.10)$$

$$q_A^\phi(x, \omega) = -\sum_s \frac{q_s}{N_s} \left( q_s + \frac{k_s}{k_\parallel} N_s + \tau_s \rho_{S,e}^2 \frac{k_\parallel k_s}{\omega^2} \right), \quad (7.11)$$

$$q_\phi^A(x, \omega) = -\sum_s \frac{F'_{0,s}}{N_s} \frac{k_y}{\omega}, \quad (7.12)$$

$$q_A^A(x, \omega) = -\sum_s \frac{q_s}{N_s} \left( q_s + \tau_s \rho_{S,e}^2 \frac{k_\parallel k_s}{\omega^2} \right), \quad (7.13)$$

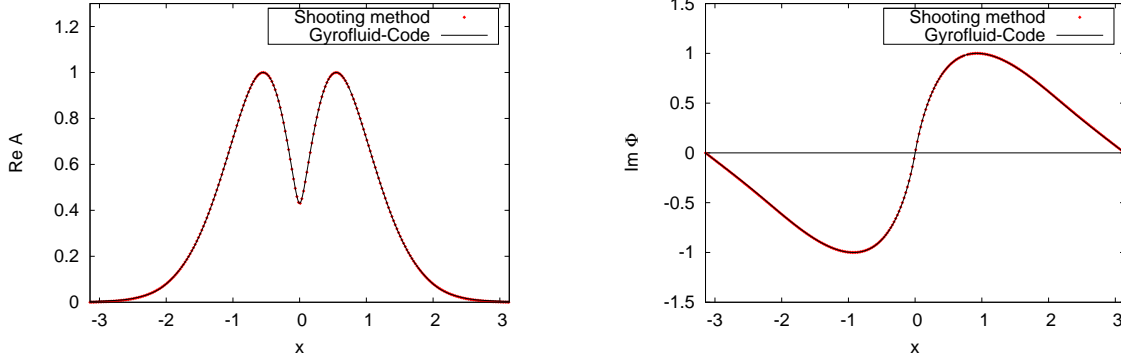


Figure 7.1: Benchmark of the gyrofluid eigenfunctions. Left: The real part of the parallel vector potential  $A$ . Right: The imaginary part of the electrostatic potential  $\phi$ .

where the prime denotes the derivative with respect to  $x$ . Also the quantities

$$\begin{aligned} F'_{0,s} &= -B_{y,0} + q_s d_s^2 u'_{0,s}, & k_{\parallel} &= -A'_0 k_y, \\ k_s &= -u'_{0,s} k_y, & N_s &= d_s^2 \left( 1 - \tau_s \frac{\rho_{S,e}^2 k_{\parallel}^2}{d_s^2 \omega^2} \right), \end{aligned} \quad (7.14)$$

have been introduced to make the notation more compact.

The coefficients resulting from the linearisation of the gyrokinetic model were derived in Sec. (5.1), Eqs. (5.4) and normalised to Alfvén units. Both these sets of eigenvalue equations are solved numerically using the shooting method described Sec. 5.1 with Dirichlet boundary conditions in the  $x$ -direction.

### 7.2.2 Linear benchmark with eigenvalue approach

The first benchmark is carried out for the parameter values  $d_e = 0.1$ ,  $d_i = 4.285$ ,  $\rho_{S,e} = 0.6$  and  $k_y = 0.6$ . This corresponds to  $\beta = 1.96 \cdot 10^{-2}$  and a realistic proton to electron mass ratio  $\mu = 1836$ .

The comparison of the eigenfunction resulting from the shooting method with results from the gyrofluid simulation is shown in Figure 7.1. Due to symmetries of the equations and the pure imaginary eigenvalue,  $\gamma = 0.0248$ , only the real part of  $A$  remains, as well as only an imaginary part of  $\phi$ . The field structures agree very well with results from the shooting code, although the boundary conditions with respect to  $x$  differ. The same procedure has been performed with EUTERPE which gives in this case  $\gamma = 0.0273$ . Both potentials are in good agreement with the shooting method as well, as shown in Figure 7.2. In this case both methods use the same boundary conditions regarding the  $x$ -direction. The comparison with the solution of the gyrofluid problem shows that the instability is mainly influenced by the dynamics at the resonant layer. The solutions drop very fast to zero approaching the boundaries and therefore the influence of the boundary conditions is suppressed.

## 7 Comparison of a compressible gyrofluid and gyrokinetic model

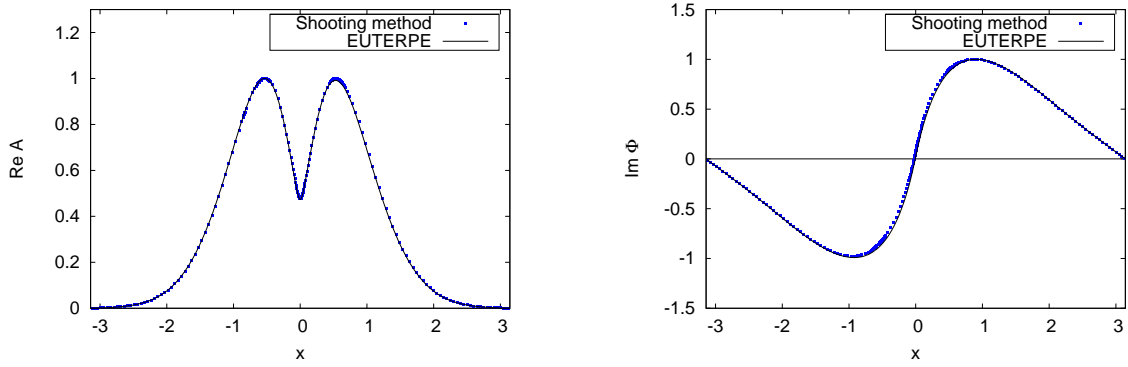


Figure 7.2: Benchmark of the gyrokinetic eigenfunctions. Left: The real part of the parallel vector potential  $A$ . Right: The imaginary part of the electrostatic potential  $\phi$ .

This will be important for further nonlinear comparisons.

To check the eigenvalues over an extended  $k_y$ -spectrum of unstable modes, simulations have been performed with the previous setup varying the simulation domain size  $L_y$ . The comparison of both fluid and kinetic results and the relevant results of the shooting method are shown in Figure 7.3<sup>1</sup>. These benchmarks show that the two codes give exact results in the linear regime over a wide range of  $k_y$ .

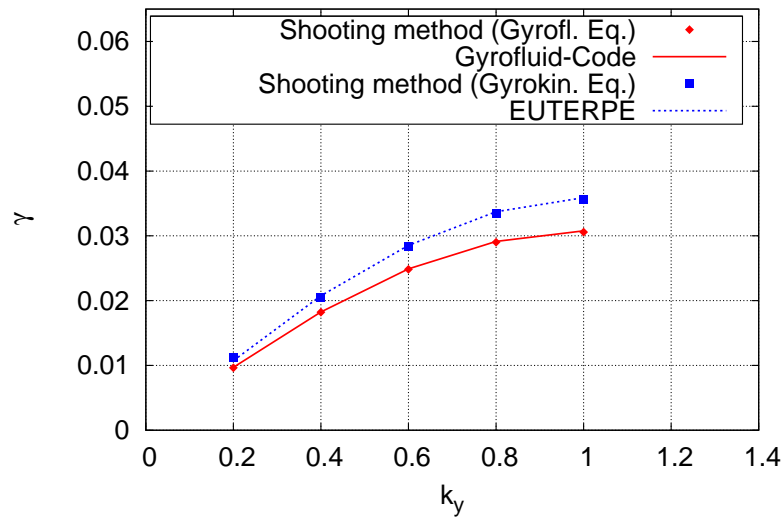


Figure 7.3: A benchmark of the linear growth rates of both models for various wave vectors  $k_y$ . Both the gyrofluid and the gyrokinetic code work linearly exact.

<sup>1</sup> The solid lines in this Figure connect simulation results as well as for all following Figures.

### 7.2.3 Model comparison in the drift kinetic limit

In the following two sets of parameters are used which are relevant for reconnection physics. The parameter associated with Setup I and II are listed in Table (7.1). Case I refers to a realistic mass ratio  $\mu$  and “kinetic” regime,  $\beta \gg m_e/m_i$ , or equivalently  $\rho_{s,e} \gg d_e$ , whereas case II defines a “medium” range between kinetic and inertial regime,  $\beta \approx m_e/m_i$ .

Simulations for cases I and II have been performed for various  $k_y$ . Over the full range of wave numbers, from the large- $\Delta'$  to the small- $\Delta'$  cases, close to the stability threshold at  $k_y \approx 2.23$ , both models describe the reconnection process very well, as shown in Figure 7.4. A relative maximum deviation of about 20% is found around  $k_y \approx 1$  for both setups. However, in the small- $\Delta'$  limit the differences of the growth rates become smaller.

The kinetic description allows one to estimate the width of the region of particle acceleration,  $\delta_e$ , due to the resonance condition  $k_{\parallel} \rho_{s,e}/d_e = k_y \delta_e/l_s \cdot \rho_{s,e}/d_e \sim \gamma$  in the small- $\Delta'$  limit and  $\delta_e \ll L$  [18]. Together with the kinetic dispersion relation in this limit,  $\gamma = k_y d_e \rho_{s,e} \Delta'/l_s$ , one gets the estimate  $\delta_e \sim \Delta' d_e^2$ . Two-Fluid-description yields the same scaling of the growth rate and current layer in the limit of marginal instability [46, 49].

Another point which might be important concerns the assumptions of the adopted gyrofluid model: The derivation uses the restriction that the bulk velocity of the species  $u_{0,s}$  is much smaller than the thermal velocity  $v_s$ . Moreover, this model uses an unshifted Maxwellian when performing the integration over the velocity space to get the equations of moments. Therefore, the gyrofluid equations hold exactly only for  $C \ll 1$ . For the linear simulations done here the amplitude of the sheared perpendicular field was chosen as  $C = 0.1$ , which approximates this limit very well and allows relatively short simulation times. However, this point has been checked simulating a mode with  $k_y = 1.0$ ,  $d_e = 0.1$ ,  $d_i = 4.285$ ,  $\rho_{s,e} = 0.3$  and decreasing  $C$  from  $10^{-1}$  to  $10^{-4}$ . These runs required very long simulation times for small  $C$ , due to the dependence of  $\gamma$  from  $l_s$ . The relative deviation of the growth rates of the models fell from approximately 20% to 12%.

Setup	I	II
$\mu$	1836	100
$\beta$	$4.91 \cdot 10^{-3}$	$4 \cdot 10^{-2}$
$\rho_{s,e}$	0.3	0.2
$d_e$	0.1	0.1
$d_i$	4.285	1.0

Table 7.1: Set of parameters defining setup I and II used for the simulations.

## 7 Comparison of a compressible gyrofluid and gyrokinetic model

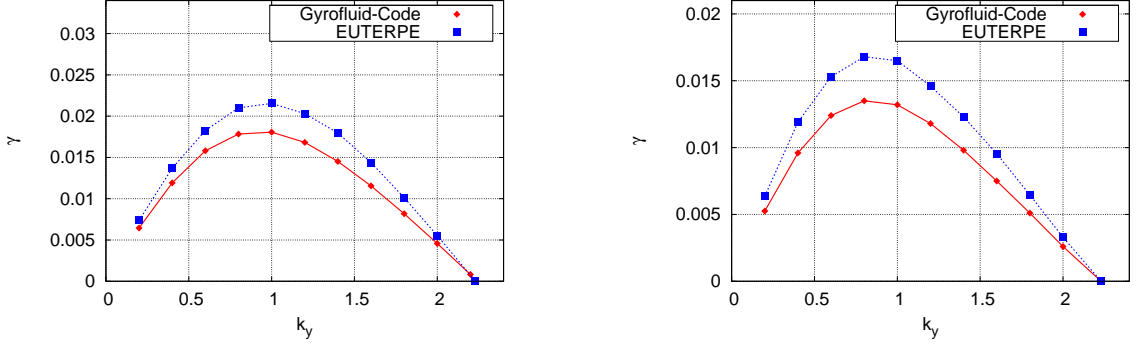


Figure 7.4: The comparison of the linear dispersion relations shows a good agreement between the two approaches over the full  $k_y$  range (Left: setup I, right: setup II).

### 7.2.4 Influence of gyro-effects

It is desirable to go beyond the drift kinetic limit and simulate the tearing mode for finite ion temperatures when the gyroradius can become much larger than the thickness of the electron diffusion region which is  $\mathcal{O}(d_e)$  [54]. Here only the linear

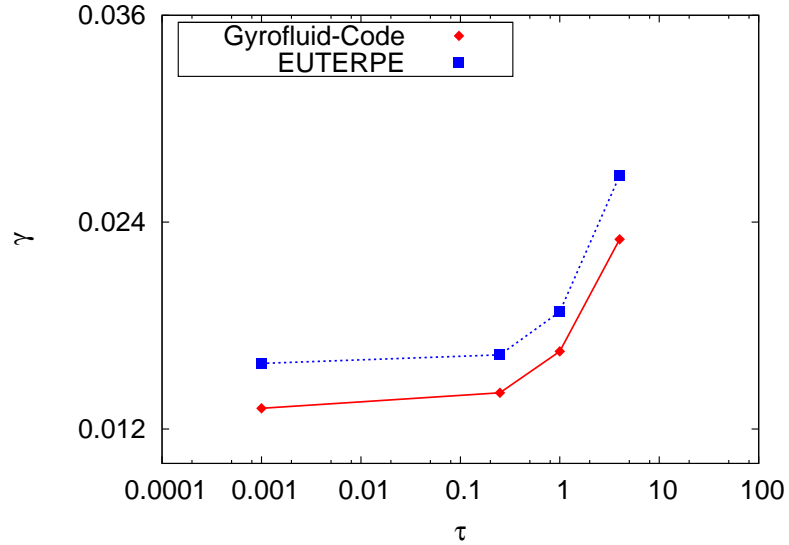


Figure 7.5: In the medium- $\Delta'$  range ( $\Delta'd_e \approx 1$ ) the codes show a good agreement of  $\gamma$  over whole range of  $\tau$ .

simulations of the codes are compared using the setup scenario II for  $k_y = 1$  and  $k_y = 2$ , while varying  $\tau$ . The gyrokinetic effects now enter according to Eq. (2.12, 7.7) using the Padé approximation.

Figures 7.5 and 7.6 show that the growth rates obtained with the two different codes behave qualitatively very similar when  $\tau$  is varied. While for small  $\tau$  the growth rate remains nearly constant, for larger ion-gyroradii,  $\rho_i \gg \rho_{s,e}$  ( $\tau \gtrsim 1$ ), the growth rate

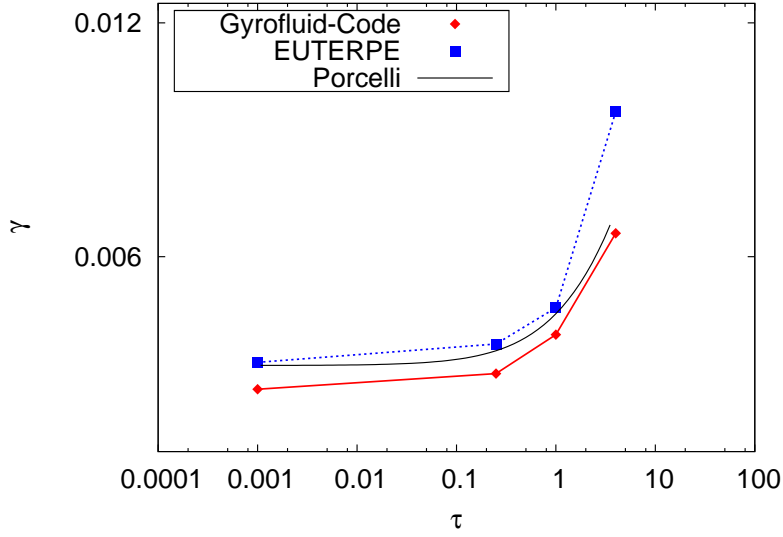


Figure 7.6: Small- $\Delta'$  range: Both codes show a good agreement of the growth rates for relatively small  $\tau$ . The analytical prediction, Eq. (7.15), fits well for both the gyrokinetic and gyrofluid model.

begins to increase strongly. For the medium range  $k_y \approx 1$  both models cover the physics very well, see Figure 7.5. This result is important since it shows clearly that the gyro-effects are being covered correctly by both gyro-approaches, which provides a good starting point for the following comparisons in the nonlinear regime.

Figure 7.6 displays the simulation results of the kinetic and fluid simulations in the small- $\Delta'$  limit. In this range of parameters an analytical prediction for a gyrokinetic ion response together with an electron fluid derived by Porcelli gives [49]

$$\gamma = k_y \Delta' \sqrt{1 + \tau \frac{d_e \rho_{S,e}}{l_s \pi}}, \quad (7.15)$$

which reproduces the simulation results to high accuracy.

## 7.3 Comparison of the nonlinear models

Continuing with the parameters of both cases I and II the nonlinear phase is discussed, concentrating on the small- $\Delta'$  regime. The saturated island half width  $w$  and oscillation frequency  $\omega_B$  in the deeply nonlinear phase are the two most relevant observables. Up to now, in the literature there are only a few extended simulation results of these quantities in homogeneous plasmas [25, 26].

It is important to note that the equilibrium considered in this section is unstable with respect to modes with  $m = 1$ , which can in general interact in the nonlinear phase with the  $m = 0$  mode. Pseudospectral codes simulate a complete rectangular domain  $[-m_{\max}, \dots, m_{\max}] \times [-n_{\max}, \dots, n_{\max}]$  in Fourier space [78],  $n$  being the

mode number in  $z$ -direction ( $n_{max} = 0$  here), so the  $m = 0$  mode is being simulated as well. In the gyrofluid simulations all relevant scales were well resolved by choosing the extent of the Fourier spectrum to  $1/k_{max} \ll d_e$ . In EUTERPE it is not necessary to choose a corresponding domain setup. Nevertheless, to match the initial computational conditions of the two methods, EUTERPE was adjusted to adopt the filter  $[-1 \dots 1] \times [0]$ . Because higher modes numbers  $m = 2, 3, \dots$  are expected to play no role in the dynamics the chosen filter does not restrict the essential physics. The gyrokinetic simulations were performed with up to  $N_p = 3 \cdot 10^7$  markers with a minimum time step  $\Delta t = 0.125$ . The skin depth  $d_e = 0.1$  is resolved with at least 16 points, whereas the width of the perturbed current produced by the parallel electric field,  $\delta_e$ , was resolved with about ten points. The numerical resolution of the vector potential in the  $x$ -direction amounts to  $n_{\bar{s}} = 1024$  points, which separates scales up to  $\Delta x = 5 \cdot 10^{-3}$ . This introduces an upper error range, which can be removed with finer grid resolutions but demands a much higher computational effort.

Two different methods are applied to obtain the island half widths  $w$  of the collisionless tearing mode. Assuming the constant- $A$  approximation, Eq. (1.25) (Sec. 1.4.3) is used. Otherwise, without any approximation, one can obtain the exact island half width using the geometric definition of the island separatrix by solving numerically Eq. (6.1) (Sec. 6.1) on the discrete spatial grid used in the codes.

### 7.3.1 Drift kinetic limit

The evolution of the island half width into the deeply nonlinear regime is shown in Figure 7.7 for the parameter case I and  $k_y = 1.8$  obtained with both codes. The Figure depicts the solution of Eq. (6.1) (geometric island half width) at each time step. Both gyrofluid and gyrokinetic models behave well in the nonlinear phase and show a clear saturated phase beginning at  $t \approx 1500$ . The energy conservation proved to be more accurate than 2.5%. Moreover, it turned out for all simulations presented here that the coupling between the modes  $m = 0$  and  $m = 1$  is very weak and can be neglected. Figure 7.8 shows a comparison of the evolution of the exact island half width and the island half width obtained according to Eq. (1.25) for the gyrofluid simulation shown in Figure 7.7 for  $k_y = 1.8$ . For wave vectors  $k_y \geq 1.8$ , which corresponds to the small- $\Delta'$  limit, the island half width calculated with the constant- $A$  approximation is valid within the precision of the measurement. Nevertheless, in the following Eq. (6.1) (geometric definition of  $w$ ) is used.

When the island width becomes comparable to the linear current sheet thickness  $\delta_e$ , the mode saturates [19]. After the transition into the saturation phase the width of the island begins to oscillate with the characteristic frequency  $\omega_B$ , which is clearly visible in Figure 7.7 and 7.8. From the time series  $w(t)$  the saturated island width  $w$  is measured by taking the mean value  $w = \langle w(t) \rangle_T$  after saturation starts.

In the following both quantities  $w$  and  $\omega_B$  are measured for an extended parameter range to compare the gyrokinetic and gyrofluid models, and to check the validity of analytical predictions in this regime of parameters.

Figure 7.9 shows  $w$  as a function of the longest wavelength in the system for both parameter cases. For low values of  $k_y \approx 1.6$  the relative difference of the island

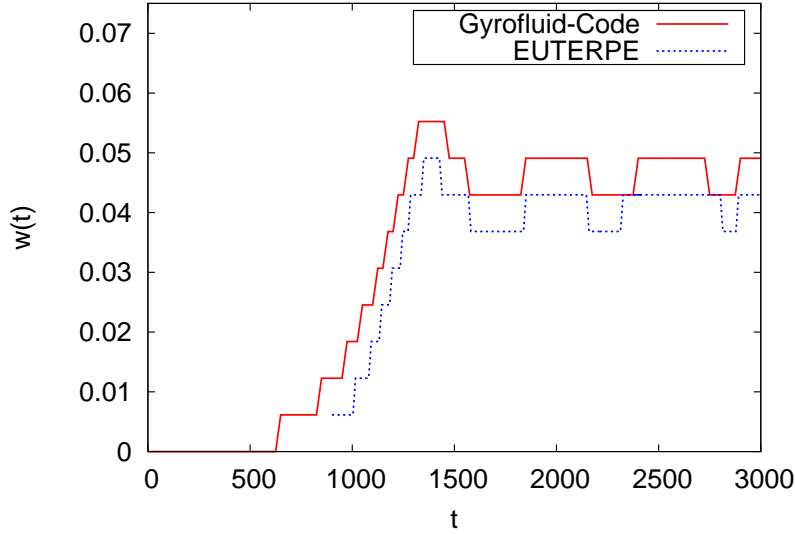


Figure 7.7: Island half width as a function of time for  $k_y = 1.8$  (case I, small- $\Delta'$ ). Both gyrofluid and gyrokinetic models show clear saturated behaviour of the mode. The steps are due to the spatial discrete grid points.

half widths obtained with the two adopted models is found to about 30% for both parameter cases I and II. Increasing  $k_y$  to the range  $k_y = 1.9, \dots, 2.23$  (close to the stability threshold) the agreement between the results of the two codes is much better. The relative deviation of the island half widths is approximately 10% for  $k_y = 1.9$  in both setups and vanishes practically for higher wave numbers. This shows that for  $\Delta' \lesssim 1$  both models agree very well. Therefore, there are no significant differences between the gyrofluid and the gyrokinetic model for small island widths, i. e. when  $w \lesssim d_e$ . So, for the cases investigated here in which the island half width and the extend of the electron current layer thickness  $\delta_e$  are much smaller than the equilibrium scales, the fluid description produces practically the same island half widths as the more complete kinetic model. The comparison between the models also shows that the island width is slightly higher in the fluid description than in the kinetic model. These are the first extended comparisons of the saturated island width in slab geometry over a broad range of parameters.

Since for both parameter cases the ion skin depth is much larger than the electron skin depth,  $d_e \ll d_i$ , electron inertia dominates completely. It was shown by Drake and Lee that the tearing mode saturates approximately when  $w \approx \delta_e$ , which in this regime means  $w \sim \Delta' d_e^2$  [19]. The detailed estimation yields  $w = \Delta' d_e^2 / (2G)$  (Sec. 6.1). Therefore, in the small island limit,  $d_e \ll L \approx l_s$ , the saturated island half width is described only by the skin depth  $d_e$  and the tearing mode stability parameter  $\Delta'$ , which for the equilibrium here is known analytically from Eq. (4.6) (Sec. 4.2).

The analytical prediction in comparison with our simulation results depending on  $k_y$  is shown in Figure 7.10. Drake and Lee's estimate of  $w$  reflects well the qualitative

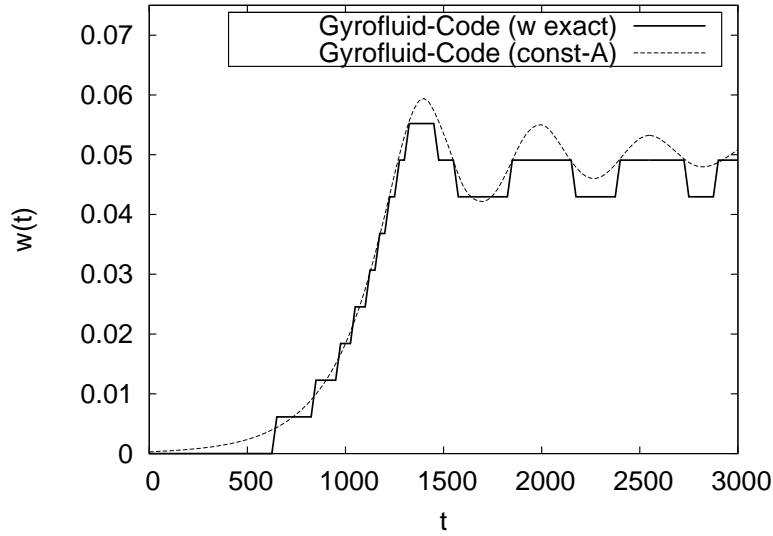


Figure 7.8: Comparison between the exact island width obtained by solving Eq. (6.1) on a discrete spatial grid and the island half width calculated according to Eq. (1.25) (Setup I and  $k_y = 1.8$ ). In the small- $\Delta'$  limit the constant- $A$  approximation is numerically confirmed.

behaviour of the saturated island half widths over the shown  $k_y$ -range and agrees more closely with the gyrokinetic than the gyrofluid results. The deviations of the prediction of  $w$  can be caused by assumptions which are not completely valid in the simulations. For instance, in the analytical estimations the shifted background Maxwellian was not used rigorously, and in addition the density response was neglected.

For both parameter cases investigated here, the island width does not seem to depend on the values of  $\rho_{S,e} = 0.2, 0.3$ , as can be seen by comparing the left and right panel of 7.9. This suggests that there is no influence of finite electron temperature effects on the island width. This is consistent with the fact that the analytical prediction of Drake and Lee does not contain finite electron temperature effects related to  $\rho_{S,e}$ , which are linked to finite pressure effects and the width of the ion inflow region [46]. Since  $\rho_{S,e}$  is comparable to the electron skin depth and the analytical model does not contain this quantity, it is unclear whether it plays an important role in nonlinear simulations with both kinetic species. To investigate this dependence the parameters  $k_y = 1.8$ ,  $\Delta' d_e \approx 0.25$ ,  $\mu = 1836$  are fixed and  $\rho_{S,e} = 0.3, 0.1, 0.05, 0.025$  is varied. The simulations have shown that the island half width remains the same ( $w \approx 0.04$ ) to high accuracy in both gyrokinetic and gyrofluid simulations. It follows that in the small- $\Delta'$  regime the pressure scale has no influence on the saturation level of the tearing mode.

A further important nonlinear quantity which has been compared within the adopted gyrokinetic and gyrofluid models is the oscillation frequency  $\omega_B$  that characterises the saturation phase, as shown in Figure 7.7 and 7.8. The parameter cases I and

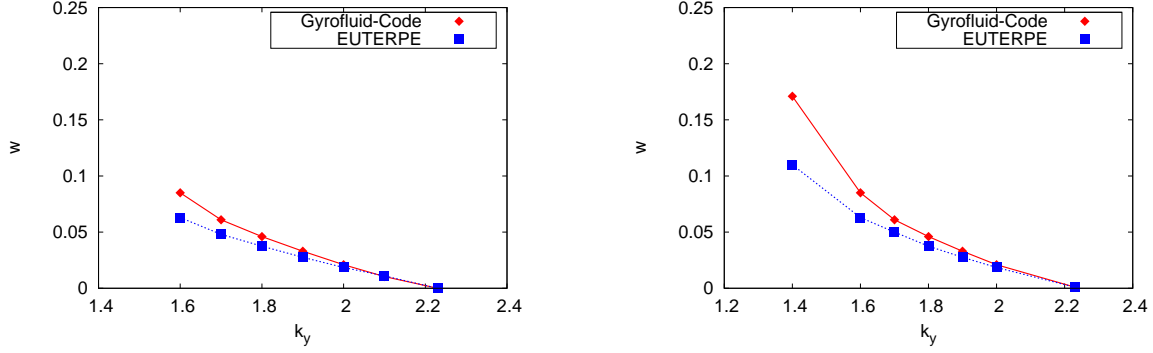


Figure 7.9: Saturated island half width  $w$  as a function of  $k_y$  (Left: setup I, right: setup II). The gyrokinetic and gyrofluid models show a very good agreement in determining the saturated island half width in the small- $\Delta'$  limit.

II are considered again measuring the oscillation frequency in the deeply nonlinear saturation phase as described in Sec. 6.1. In the gyrofluid simulations the oscillation frequency can always be clearly observed. While for parameters of case I the frequency can be measured clearly for the gyrokinetic model, it is more difficult in case II. Therefore, the number of markers was doubled to  $N_p = 3 \cdot 10^7$  and the previous time step was halved to  $\Delta t = 0.125$ .

The results are displayed in Figure 7.11, where the left panel refers to setup I and the right panel to setup II. Both models agree very well for all wave numbers  $k_y$  shown here, also for moderate values of  $\Delta' d_e \approx 1$ . These results clearly show that also in this regime the oscillatory behaviour of the saturated reconnection process can be described completely by a fluid description.

From a rough kinetic estimation one gets  $\omega_B \sim k_y v_e w / (2l_s)$  [19, 26], so the frequency is roughly proportional to the island width and the stability parameter  $\Delta'$ . The results in Figure 7.11 confirm this linear scaling in the limit of low- $\Delta'$  values. As stated in Sec. (6.1), the explanation by Drake referring to a resonant interaction of trapped electron with the mode causing saturation and oscillation is not completely convincing. Both models show practically the same nonlinear behaviour when  $\Delta' d_e$  is small enough.

### 7.3.2 Finite ion temperature effects

This section deals with the extension of previous nonlinear results by including finite ion temperature effects using the full finite Larmor radius response. Here the focus lies on the parameter case I and the behaviour of the saturated island half width with increasing ion temperature.

In Figure 7.12 the saturated island half width is shown when the ion temperature is varied using the values  $\tau = 1/900, 0.25, 1, 4$  and fixing  $k_y = 1.8$ . The island width only changes by about 5% over approximately three orders of magnitude of  $\tau$ . This shows that finite Larmor radius effects on  $w$  are weakly relevant for  $\Delta' d_e \lesssim 1$ .

## 7 Comparison of a compressible gyrofluid and gyrokinetic model

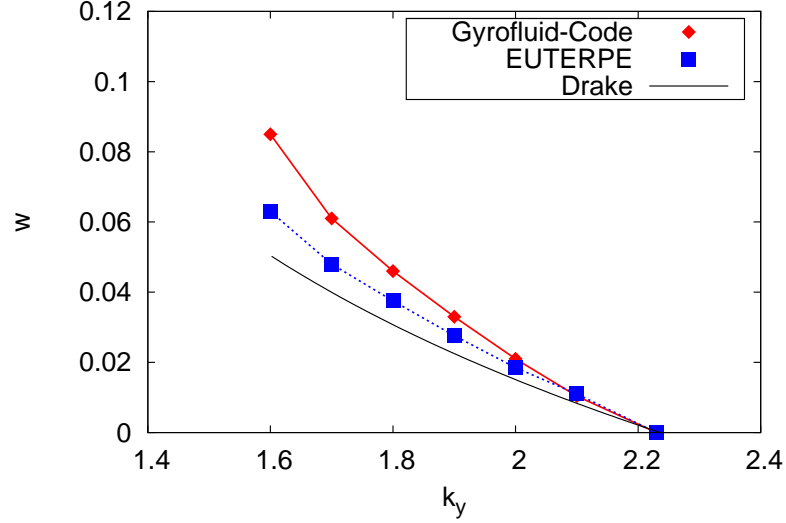


Figure 7.10: The saturated island half width  $w$  depending on  $k_y$  is compared with the prediction by Drake and Lee (case I). The analytical model shows a good qualitative agreement with simulation results for  $\Delta'd_e < 1$ .

As stated earlier, Ref. [19] predicts the general saturation condition  $w \approx \delta_e$ . Here, due to the influence of finite ion temperature, the electron current channel width changes according to [38]

$$\delta_e \sim \frac{\gamma l_s}{k_y v_e \sqrt{1 + \tau}}. \quad (7.16)$$

On the other hand the growth rate increases according to  $\gamma \sim \sqrt{1 + \tau}$ , as has been shown in Sec. 7.2. Using Eq. (7.15) for the growth rate and Eq. (7.16) for the modified current width, the generalised scaling of the saturated island half width

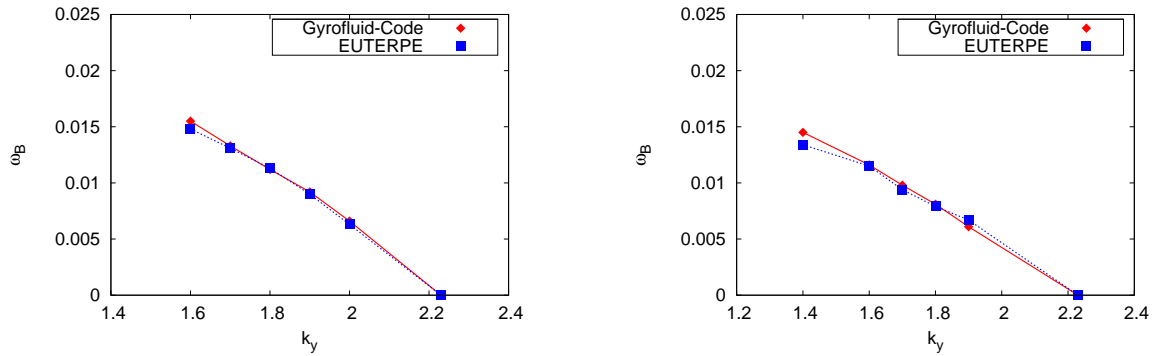


Figure 7.11: Oscillation frequency as a function of the wave number  $k_y$  for the two models (Left: case I, right: case II). Both models agree very well in the low- and medium- $\Delta'$  range.

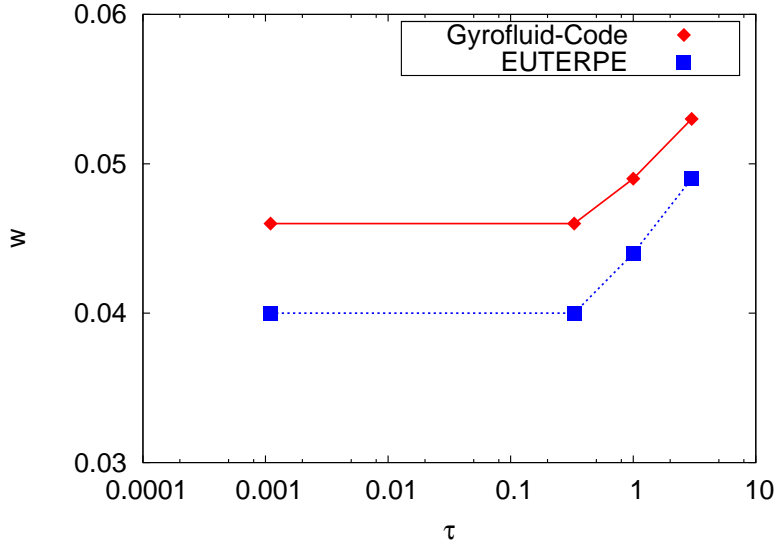


Figure 7.12: Comparison of the island half widths  $w$  as a function of the temperature ratio  $\tau$  (setup I and  $k_y = 1.8$ ).

for finite  $\tau$  becomes

$$w \sim \Delta' d_e^2,$$

as stated for the drift kinetic case. This estimation makes evident that the saturated island width does not change significantly with ion temperature.

The gyrofluid model has been benchmarked for the first time. The comparison of both models shows a good agreement for linear and nonlinear simulations. For the drift kinetic limit the saturated island widths differ only slightly from each other while the bounce frequencies are practically the same. Effects of FLR affect both models with the same amount in the linear as well as in the nonlinear regime for the parameters chosen here.

## 7 *Comparison of a compressible gyrofluid and gyrokinetic model*

## 8 Conclusions and outlook

Electromagnetic simulations of the linear tearing mode without equilibrium gradients have been performed with EUTERPE. The dispersion relation has been compared with a shooting method showing an excellent agreement between both methods. Linear simulations in the presence of finite temperature gradients were benchmarked as well to high precision. Employing finite density and temperature gradients a critical threshold of the linear growth rate over the temperature to density ratio has been observed. Comparing the simulations with an analytic hybrid approach it's predictions could be confirmed to good agreement as well as the occurrence of the critical threshold in this parameter regime. The kinetic theory of Drake and Lee is not able to predict the linear critical threshold what hints that their estimates are too rough. A detailed kinetic linear stability analysis in the presence of diamagnetic effects is presently not available.

Nonlinear single-mode simulations of the saturated tearing mode have been carried out. The simulation results are compared to the predicted saturated island half width predicted by Drake and Lee. For small enough growth rates the analytic result can be recovered but deviates from the simulation results in the medium- $\Delta'$  range. Therefore, the analytic prediction is confirmed. An comprehensive theory of nonlinear collisionless magnetic reconnection which includes more realistic scenarios, e. g. including the coupling of higher harmonics modes and parameter ranges which allow finite- $\Delta'$  values of order unity is currently not available. Also, it is important to note that a capacious theory of nonlinear tearing including diamagnetic effects could be highly desirable.

The super-exponential behaviour of the tearing mode has been demonstrated for two magnetic equilibria and numerical difficulties has been discussed.

For the first time the threshold between sub- and super-exponential behaviour has been verified measuring the oscillation frequency of the field energy depending on the wave number and equilibrium current width. This threshold is an important quantity and could be the starting point for numerical investigations getting deeper insight into the question of possible non-saturation of tearing modes.

A detailed parameter study of the threshold for different equilibrium parameters was presented. The scan of the equilibrium width  $a$  and box size  $L_x$  shows clearly that the assumption of the high- $\Delta'$  regime does not necessarily leads to super-exponential behaviour. Moreover, there exists a region in the parameter space allowing a super-exponential phase of mode right at linear stability threshold.

A comparison of the gyrokinetic model and a compressible gyrofluid model has been performed. The results of both approaches have been compared to each other linearly and nonlinearly for an extended set of parameters. As a first step, the shooting method has been used to benchmark the linear simulations of both codes in the drift

## *Bibliography*

kinetic limit. The linear eigenmodes of the two models have been benchmarked for a single wave number and a fixed set of plasma parameters, whereas the linear growth rates of both codes have been compared for a range of wave numbers. It has been shown that in the linear regime both codes give results with high degree of accuracy. Then the results of the two models have been compared over the whole spectrum of linearly unstable wave numbers for two sets of plasma parameters showing a good agreement between the growth rates obtained with the gyrokinetic model and the gyrofluid one.

The linear simulations have been extended to the case of finite ion temperature, where it has been shown that ion gyro-orbit averaging effects can be properly described by both approaches. Furthermore, numerical simulations in the small- $\Delta'$  range compare favourably with the asymptotic theory of Porcelli.

Nonlinear simulations of both models have been carried out in the small- $\Delta'$  regime. A detailed comparison of observables such as the evolution and saturation of the island width, as well as its oscillation frequency in the saturated phase has been carried out. The gyrokinetic and gyrofluid simulations have shown that close to marginal stability the evolution and saturation of the island width for both models is practically the same. Moreover, an important and new observation is that the oscillation frequency of the island width shows no difference between the two models. Therefore, the main result is that the nonlinear evolution of the collisionless tearing mode in the drift kinetic limit can essentially be well described by fluid theory. Also finite ion temperature effects in the saturated island phase have been considered. Here again both models differ only slightly when measuring the island width. Therefore, in the regimes investigated here, the nonlinear reconnection physics can be completely described with a gyrofluid approach.

Slightly stronger deviations between the simulation results occur for  $\Delta'd_e$  of order unity, suggesting that further investigations will be of interest in this regime, as well as in cases where  $\Delta'd_e$  is much larger than unity for which a detailed nonlinear comparison between the gyrokinetic and gyrofluid models is still missing.

Numerical simulations of magnetic reconnection using fluid models including resistivity can be performed in a straight manner. However, it is still an open issue how to perform numerically exact benchmarks of the collisional tearing mode using the PIC framework. Closely related to this topic are simulations of micro-tearing modes with PIC methods which are left for further work.

# Bibliography

- [1] E. R. Priest and T. G. Forbes, *Magnetic Reconnection: MHD Theory and Applications* (Cambridge University Press, 2000).
- [2] J. Birn and E. R. Priest, *Reconnection of Magnetic Fields* (Cambridge University Press, 2007).
- [3] M. Hoshino, T. Mukai, T. Terasawa, and I. Shinohara, *J. Geophys. Res.* **106**, 25979 (2001).
- [4] M. Hoshino, T. Mukai, A. Nishida, S. Kokubun and T. Yamamoto, *Adv. Space Res.* **26**, 425 (2000).
- [5] M. Yamada, R. Kulsrud and J. Hantao, *Rev. Mod. Phys.* **82**, 603 (2010).
- [6] D. Biskamp, *Magnetic Reconnection in Plasmas* (Cambridge University Press, 2000).
- [7] A. Y. Aydemir, *Phys. Fluids B Letter* **4**, 3469 (1992).
- [8] V. M. Vasyliunas, *Rev. Geophys.* **13**, 303 (1975).
- [9] P. Ricci, J. U. Brackbill and W. Daughton, G. Lapenta, *Phys. Plasmas* **11**, 4102 (2004).
- [10] L. Comisso, D. Grasso, F. L. Waelbroeck and D. Borgogno, *Phys. Plasmas* **20**, 092118 (2013).
- [11] R. G. Kleva, J. F. Drake and F. L. Waelbroeck, *Phys. Plasmas* **2**, 23 (1994).
- [12] E. G. Harris, *Nuovo Cim.* **23**, 115 (1961).
- [13] R. J. Goldston and P. H. Rutherford, *Introduction to Plasma Physics* (Institute of Physics Publishing, London, 1995).
- [14] H. P. Furth, J. Killeen, and M. N. Rosenbluth, *Phys. Fluids* **6**, 459 (1963).
- [15] J. Wesson, *Tokamaks* (Oxford University Press, 1986).
- [16] N. T. Gladd, J. F. Drake, C. L. Chang, and C. S. Liu, *Phys. Fluids* **23**, 1182 (1980).
- [17] P. H. Rutherford, *Phys. Fluids* **16**, 1903 (1973).
- [18] J. F. Drake and Y. C. Lee, *Phys. Fluids* **20**, 1341 (1977).

## Bibliography

- [19] J. F. Drake and Y. C. Lee, *Phys. Rev. Lett.* **39**, 453 (1977).
- [20] I. Katanuma and T. Kamimura, *Phys. Fluids* **23**, 2500 (1980).
- [21] D. Grasso, F. Pegoraro, F. Porcelli and F. Califano, *Plasma Phys. Control. Fusion* **41**, 1497 (1999).
- [22] L. Comisso, F. L. Waelbroeck, and D. Grasso, *J. Phys.: Conf. Ser.* **401**, 012005 (2012).
- [23] M. Ottaviani and F. Porcelli, *Phys. Rev. Lett.* **71**, 3802 (1993).
- [24] M. A. Shay and J. F. Drake, *Geophys. Res. Lett.* **25**, 3759 (1998).
- [25] X. Y. Wang, Y. Lin, L. Chen, X. Lu and W. Kong, *Phys. Plasmas* **18**, 122102 (2011).
- [26] W. Wan, Y. Chen and S. E. Parker, *Phys. Plasmas* **12**, 012311 (2005).
- [27] T. S. Hahm, W. W. Lee and A. J. Brizard, *Phys. Fluids* **31**, 1940 (1988).
- [28] R. Kleiber, C. Beidler, M. Borchardt, T. Fehér, R. Hatzky, K. Kauffmann, A. Könies, A. Mishchenko and J. M. Garcia-Regaña, TH/P3-06.
- [29] M. J. Pueschel, F. Jenko, D. Told, and J. Büchner, *Phys. Plasmas* **18**, 112102 (2011).
- [30] W. Daughton and H. Karimabadi, *J. Geophys. Res.*, **110**, A03217 (2005).
- [31] R. Numata, G. G. Howes, T. Tatsuno, M. Barnes and W. Dorland, *J. Comp. Phys.* **229**, 9347 (2010).
- [32] R. Numata, W. Dorland, G. G. Howes, N. F. Loureiro, B. N. Rogers and T. Tatsuno, *Phys. Plasmas* **18**, 112106 (2011).
- [33] J. M. TenBarge, W. Daughton, H. Karimabadi, G. G. Howes and W. Dorland, *Phys. Plasmas* **21**, 020708 (2014).
- [34] A. Biancalani and B. D. Scott, *Europhys. Lett.* **97**, 15005 (2012).
- [35] M. Hirota, P. J. Morrison, Y. Ishii, M. Yagi and N. Aiba, Submitted to *Nuclear Fusion* (2013).
- [36] A. Bhattacharjee, K. Germaschewski and C. S. Ng, *Phys. Plasmas*. **12**, 042305 (2005).
- [37] W. Dorland and G. W. Hammett, *Phys. Fluids B* **5**, 812 (1993).
- [38] B. N. Rogers, S. Kobayashi, P. Ricci, W. Dorland, J. Drake, and T. Tatsuno, *Phys. Plasmas* **14**, 092110 (2007).

- [39] B. N. Rogers, S. Kobayashi, P. Ricci, W. Dorland, J. Drake, and T. Tatsuno, Phys. Plasmas **18**, 049902 (2011).
- [40] F. L. Waelbroeck and E. Tassi, Commun. Nonlinear Sci. Numer. Simulat. **17**, 2171 (2012).
- [41] R. Fitzpatrick and F. Porcelli, Phys. Plasmas. **11**, 4713 (2007).
- [42] D. Del Sarto, C. Marchetto, F. Pegoraro and F. Califano, Plasma Phys. Control. Fusion **53**, 035008 (2011).
- [43] D. Grasso, F. Califano, F. Pegoraro and F. Porcelli, Plasma Phys. Rep., **26**, 6 (1999).
- [44] E. Tassi, F. L. Waelbroeck and D. Grasso, J. Phys. Conf. Series, **260**, 012010 (2010).
- [45] N. F. Loureiro, D. A. Uzdensky, A. A. Schekochihin, S. C. Cowley and T. A. Yousef, Mon. Not. R. Astro. Soc. **000**, 1 (2009).
- [46] A. Zocco and A. A. Schekochihin, Phys. Plasmas **18**, 102309 (2011).
- [47] N. F. Loureiro, A. A. Schekochihin and A. Zocco, Phys. Rev. Lett. **111**, 025002 (2013).
- [48] G. Hornig, *Zur kovarianten Formulierung der magnetischen Rekonnexion* (PhD thesis, 1997).
- [49] F. Porcelli, Phys. Rev. Lett. **66**, 425 (1991).
- [50] V. V. Mirnov, C. C. Hegna and S. C. Prager, Plasma Phys. Reports, **11**, 9 (2004).
- [51] L. Comisso, D. Grasso, E. Tassi and F. L. Waelbroeck, Phys. Plasmas **19**, 042103 (2012).
- [52] R. Fitzpatrick, Phys. Plasmas **17**, 042101 (2010).
- [53] D. Grasso, M. Ottaviani and F. Porcelli, Phys. Plasmas, **8**, 10 (2001).
- [54] S. C. Cowley, R. M. Kulsrud and T. S. Hahm, Phys. Fluids, **29**, 10 (1985).
- [55] B. Coppi, Phys. Lett. **11**, 961 (1964).
- [56] B. Basu and B. Coppi, Phys. Fluids **24**, 465 (1981).
- [57] A. Y. Aydemir, Phys. Fluids B **3**, 11 (1991).
- [58] K. H. Spatschek, *Theoretische Plasmaphysik: Eine Einführung* (Teubner Studienbücher, 1989).
- [59] T. S. Hahm, Lu Wang and J. Madsen, Phys. Plasmas, **16**, 022305 (2009).

## Bibliography

- [60] A. J. Brizard and T. S. Hahm, *Rev. Mod. Phys.* **79**, 421 (2007).
- [61] P. B. Snyder and G.W. Hammett, *Phys. Plasmas* **8**, 3199 (2001).
- [62] O. Mishchenko, *New methods in gyrokinetic particle-in-cell simulations* (PhD thesis, 2005).
- [63] V. Kornilov, *Global Ion-Temperature-Gradient Driven Instabilities in Stellarators within Two-Fluid and Gyrokinetic Descriptions* (PhD thesis, 2004).
- [64] R. W. Hockney and J. W. Eastwood, *Computer Simulation Using Particles* (Institute of Physics Publishing, 1988).
- [65] Satish Balay, Jed Brown, Kris Buschelman, William D. Gropp, Dinesh Kaushik, Matthew G. Knepley, Lois Curfman McInnes, Barry F. Smith and Hong Zhang, "<http://www.mcs.anl.gov/petsc>", (2013);  
Satish Balay, Jed Brown, Kris Buschelman, Victor Eijkhout, William D. Gropp, Dinesh Kaushik, Matthew G. Knepley, Lois Curfman McInnes, Barry F. Smith and Hong Zhang, ANL-95/11 - Revision 3.4, Argonne National Laboratory (2013);  
Satish Balay, William D. Gropp, Lois Curfman McInnes and Barry F. Smith, *Modern Software Tools in Scientific Computing* (Birkhäuser Press, 1997).
- [66] K. Kauffmann, *Including Collisions in Gyrokinetic Tokamak and Stellarator Simulations* (PhD thesis, 2013).
- [67] J. C. Cummings, *Gyrokinetic simulation of finite-beta and self-generated sheared-flow effects on pressure-gradient-driven instabilities*, (PhD thesis, 1995).
- [68] R. Hatzky, T. M. Tran, A. Könies, R. Kleiber and S. J. Allfrey, *Phys. Plasmas* **9**, 898 (2002).
- [69] R. Hatzky, A. Könies and A. Mishchenko, *J. Comp. Phys.* **225**, 568 (2007).
- [70] Stoer and Bulirsch, *Einführung in die Numerische Mathematik II* (Springer Verlag, 1978).
- [71] F. Porcelli, D. Borgogno, F. Califano, D. Grasso, M. Ottaviani and F. Pegoraro, *Plasma Phys. Control. Fusion* **44**, B389 (2002).
- [72] B. N. Rogers, J. F. Drake and M. A. Shay, *Geophys. Res. Lett.* **27**, 3157 (2000).
- [73] M. R. Scott, *J. Comp. Phys.* **12**, 334 (1973).
- [74] M. Takata and W. Löffler, *Publ. Astron. Soc. Japan* **56**, 645 (2004).
- [75] R. D. Sydora, *Phys. Plasmas* **8**, 1929 (2001).
- [76] M. Ottaviani and F. Porcelli, *Phys. Plasmas* **2**, 4104 (1995).

- [77] D. Grasso, F. Califano, F. Pegoraro and F. Porcelli, *Plasma Phys. Rep.* **26**, 512 (2000).
- [78] S. K. Lele, *J. Comp. Phys.* **103**, 16 (1992).

## *Bibliography*

# Declaration of originality

Hiermit erkläre ich, daß diese Arbeit bisher von mir weder an der Mathematisch-Naturwissenschaftlichen Fakultät der Ernst-Moritz-Arndt-Universität Greifswald noch einer anderen wissenschaftlichen Einrichtung zum Zwecke der Promotion eingereicht wurde.

Ferner erkläre ich, daß ich diese Arbeit selbständig verfasst habe und keine anderen als die darin angegebenen Hilfsmittel und Hilfen benutzt und Textabschnitte eines Dritten ohne Kennzeichnung übernommen habe.

---

Oliver Zacharias

*Declaration of originality*

# Acknowledgements

First of all I would like to thank Per Helander very much to give me the great possibility to study plasma physics.

Further thanks go to my advisor Ralf Kleiber. Beside many others I would like to acknowledge Luca Comisso, Henry Leyh and Matthias Borchardt, Roman Hatzky, Alexey Mishchenko, Daniela Grasso and Alessandro Zocco.

Part of this work was carried out using the HELIOS supercomputer system at the Computational Simulation Centre of International Fusion Energy Research Centre (IFERC-CSC), Aomori, Japan, under the Broader Approach collaboration between Euratom and Japan, implemented by Fusion for Energy and JAEA.

## *Acknowledgements*

# Index

Alfvén unit system, 31  
Alfvén wave, 36, 42

collisionless tearing mode, 3, 10  
complementary plasma dispersion function, 41  
constant- $\Psi$  approximation, 14, 18  
constant- $A$  approximation, *see* constant- $\Psi$  approximation

$\delta f$ -ansatz, 22, 26  
drift tearing mode, 16

electron tearing mode model, 42  
EUTERPE unit system, 31

full tearing mode model, 42

gyrokinetic equation, 22  
gyrokinetic model, 21

high- $\Delta'$  regime, 16, 33

low- $\Delta'$  regime, *see* high- $\Delta'$  regime  
long wavelength approximation, 23

magnetic island, 18  
micro-tearing mode, 4

nonlinear tearing mode, 17

Ohm's law, 2, 11

Padé approximation, 24  
plasma dispersion function, 37, 41

resistive tearing mode, 3, 4, 17  
Riccati method, 43

stability parameter, 13, 32

Vlasov-Maxwell system, 22